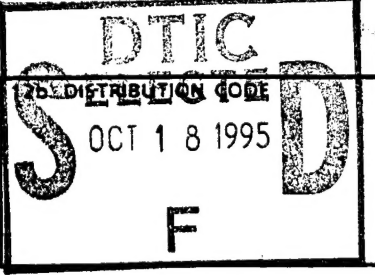


6639

## REPORT DOCUMENTATION PAGE

Public reporting burden for this collection of information is estimated to average 1 hour per response, including the gathering and maintaining the data needed, and completing and reviewing the collection of information. Send comments and suggestions for reducing this burden to Washington Headquarters Services, Directorate for Information Operations and Processing, Paperwork Reduction Project, 1204, Arlington, VA 22202-4302, and to the Office of Management and Budget, Paperwork Reduction Project, 1204, Washington, DC 20503.

1. AGENCY USE ONLY (Leave blank)			2. REPORT DATE	3. REPORT TYPE AND DATES COVERED
			August 1995	Final Technical 1 Jan 94 — 30 Jun 95
4. TITLE AND SUBTITLE			5. FUNDING NUMBERS	
Thrust Vector Control of Rectangular Jets using Counterflow			Grant # F49620-94-1-0046	
6. AUTHOR(S)			8. PERFORMING ORGANIZATION REPORT NUMBER	
Michael R. Van der Veer and Paul J. Strykowski				
7. PERFORMING ORGANIZATION NAME(S) AND ADDRESS(ES)			10. SPONSORING / MONITORING AGENCY REPORT NUMBER	
University of Minnesota, ORTTA Office of Research and Technology Transfer 1100 Washington Ave. S, Suite 201 Minneapolis, Minnesota 55415-1226			N/A F49620 - 94-1-0046	
9. SPONSORING / MONITORING AGENCY NAME(S) AND ADDRESS(ES)			11. SUPPLEMENTARY NOTES	
AFOSR 110 Duncan Avenue Suite B115 Bolling AFB, DC 20332-0001				
12a. DISTRIBUTION / AVAILABILITY STATEMENT			13. ABSTRACT (Maximum 200 words)	
Approved for public release. Distribution unlimited			 <p>DTIC DISTRIBUTION CODE S OCT 18 1995 D F</p>	
14. SUBJECT TERMS			15. NUMBER OF PAGES	
Thrust vector control; counterflow; subsonic turbulent jets; jet attachment; Coanda effect			140	
17. SECURITY CLASSIFICATION OF REPORT			18. SECURITY CLASSIFICATION OF THIS PAGE	
Unclassified			Unclassified	
19. SECURITY CLASSIFICATION OF ABSTRACT			20. LIMITATION OF ABSTRACT	
Unclassified				

19951017092

THRUST VECTOR CONTROL OF RECTANGULAR JETS  
USING COUNTERFLOW

A Final Technical Report  
Submitted to

THE AIR FORCE OFFICE OF SCIENTIFIC RESEARCH  
WASHINGTON, DC

Accession For	
NTIS	CRA&I
DTIC	TAB
U. unclassified	
Justification	
By	
Distribution /	
Availability Codes	
Dist	Avail and / or Special
A-1	

BY

Michael R. Van der Veer & Paul J. Strykowski  
Department of Mechanical Engineering  
University of Minnesota  
Minneapolis, Minnesota 55455

31 AUGUST, 1995

## TABLE OF CONTENTS

	Page
<b>LIST OF FIGURES</b> .....	v
<b>NOMENCLATURE</b> .....	xi
<b>1. INTRODUCTION</b> .....	1
<b>2. THEORETICAL BACKGROUND</b> .....	8
<b>3. EXPERIMENTAL SETUP</b> .....	17
3.1 NOZZLE AND SUCTION COLLAR DESIGN.....	17
3.2 FORWARD AND REVERSE FLOW FACILITIES .....	19
3.3 INSTRUMENTATION AND DATA ACQUISITION .....	21
3.4 FLOW VISUALIZATION .....	22
<b>4. FLOW CONDITIONS</b> .....	24
4.1 "STANDARD" JET .....	24
4.2 "COUNTERFLOWING" JET .....	27
4.2.1 Introductory Comments .....	27
4.2.2 Reverse Flow Calibration .....	29
4.2.3 Vector Angle Determination.....	32
4.2.4 Measurement Techniques.....	36
<b>5. RESULTS AND DISCUSSION</b> .....	40
5.1 PRELIMINARY OBSERVATIONS .....	40
5.2 RESPONSE TO GEOMETRICAL CHANGES IN COLLAR .....	45
5.2.1 Effect of Gap .....	46
5.2.2 Effect of Divergence Half Angle .....	48
5.2.3 Effect of Length.....	49
5.2.4 Geometry Impact on Critical Vector Angle .....	51
5.3 EFFECT OF PRIMARY EXIT MACH NUMBER.....	53

	Page
5.4 DIMENSIONAL ANALYSIS.....	58
5.5 COLLAPSE OF DATA .....	69
<b>6. CONCLUSIONS .....</b>	<b>75</b>
<b>A. DERIVATION OF CONTROL VOLUME EQUATIONS.....</b>	<b>79</b>
<b>REFERENCES .....</b>	<b>86</b>
<b>FIGURES .....</b>	<b>92</b>

## LIST OF FIGURES

Figure 1. Schematic of the fluidic thrust vector nozzle showing vectoring when counterflow is activated in the upper shear layer of the jet.

Figure 2. Two-dimensional jet of height  $H$ . (a) A free jet entraining the surrounding fluid. (b) A jet in the presence of a curved surface of radius  $R$  illustrating the Coanda effect. Pressure near the surface is low causing jet deflection.

Figure 3. Jet attaches to the curved surface in (a). In (b), the jet continues attachment until it can no longer entrain enough fluid to maintain a low enough pressure to prevent separation. The curved wall jet along the  $\theta$  axis is stable due to the positive pressure gradient in the positive  $r$  direction.

Figure 4. Nozzle-collar configuration used to generate an axisymmetric countercurrent mixing layer (from Strykowski & Wilcoxon, 1993; with permission).

Figure 5. Schlieren photographs of an axisymmetric jet at  $Re_D = 7.8 \times 10^4$  using the facility from Fig. 4. The photograph in (a) was taken without suction and (b) was obtained at a velocity ratio of  $-U_2/U_1 \approx 0.35$  (from Strykowski & Wilcoxon, 1993; with permission).

Figure 6. Scaled drawing of the nozzle-collar assembly used for counterflow vectoring. The forward stream  $U_1$  and secondary stream  $U_2$  are defined in a coordinate system having an origin in the nozzle exit plane.

Figure 7. Scaled drawing of the internal dimensions of the side and end views of the nozzle-collar configuration. The  $L = 1$  cm,  $\alpha = 30^\circ$  collar is shown.

Figure 8. Schematic showing the approximate distribution of one row of the static pressure collar wall taps. The location of tap used to measure gage exit pressure,  $\Delta P_{exit}$ , is also indicated. The collar having  $L/H = 3.5$  is shown. Tap size is not to scale.

Figure 9. Schematic of the test facility used to generate the forward velocity stream. The air exhausts into the laboratory from a rectangular nozzle shown in cross section A-A. The main drawing is not to scale.

Figure 10. Schematic of the reverse flow assembly. The drawing is not to scale.

Figure 11. Diagram illustrating integration of the Scanivalve with the static pressure taps placed along the collar wall. Static collar wall pressure distributions were sampled by the voltmeter and then passed to the computer for processing.

Figure 12. Coordinate system for standard jet measurements.

Figure 13. Mean Mach profiles along the (a) y-axis and (b) z-axis of the standard jet without any collar attached. Profiles were obtained at  $Re_H = 1.16 \times 10^5$  ( $M_e = 0.5$ ) and  $x/H = 0.05$ .

Figure 14. Mean Mach profile along y-axis for the standard jet with representative collar attached. The profile was obtained at  $Re_H = 1.16 \times 10^5$  ( $M_e = 0.5$ ) and  $x/H = 0.05$ .

Figure 15. Mean downstream Mach profiles comparing standard jet with and without a collar. Profiles are at (a)  $x/H = 10$  and  $20$ , and (b)  $x/H = 30$  and  $40$ . Exit flow conditions were  $Re_H = 1.16 \times 10^5$ .

Figure 16. Calibration curve of the pressure drop across the reverse flow meter versus the rotameter reading. Best fit is plotted as solid line.

Figure 17. Thrust vector angle determined by flow visualization. The jet is illuminated by using injected smoke particles to scatter light from a laser sheet. Angles of (a)  $0^\circ$ , (b)  $6^\circ$ , (c)  $13^\circ$  and (d)  $27^\circ$  are shown. This  $L/H = 0$  collar was used for flow visualization only.

Figure 18. Downstream pitot surveys showing increasing offset in Mach profile as measurements are made at increasing  $x/H$  positions as measured from the collar exit. The amount of offset can be used to determine the thrust vector angle,  $\delta_v$ .  $M_e = 0.5$ .

Figure 19. Schematic showing the boundaries of the control volume used to calculate vector angle. Forces are resolved from the static pressure measurements along collar walls and estimated pressure profiles across the exit plane. The outside boundary of the control volume is assumed to be at ambient pressure.

Figure 20. Collar static pressure profiles taken on the  $L/H = 2$ ,  $\alpha = 60^\circ$  collar for a gap height of  $G/H = 0.40$  at  $M_e = 0.5$ .

Figure 21. Thrust vector response curve as a function of gage exit pressure,  $-\Delta P_{exit}$ . Data are for the  $L/H = 2$ ,  $\alpha = 60^\circ$  collar at  $G/H = 0.4$  and  $M_e = 0.5$ . Open symbols compare vector angle determined by downstream Mach profiles to control volume calculations represented by the solid symbols.

Figure 22. Thrust vector response curve as a function of reverse flow to primary mass flow ratio. Data are for the  $L/H = 2$ ,  $\alpha = 60^\circ$  collar at  $G/H = 0.4$  and  $M_e = 0.5$ . The hysteretic effect of collar attachment on vector angle is shown. The critical vector angle,

$\delta_{v, cr}$ , marked by the arrow, is defined as the maximum angle achieved before the jet becomes bistable.

Figure 23. Collar static pressure distributions with attached jet for: (a) the  $L/H = 2, \alpha = 60^\circ$  collar at  $G/H = 0.4$ , and (b) the  $L/H = 3.5, \alpha = 30^\circ$  collar at  $G/H = 0.75$ .  $M_e = 0.5$  for both cases.

Figure 24. Thrust vector response curve as a function of mass flow ratio for the  $L/H = 2, \alpha = 60^\circ$  collar at  $M_e = 0.5$ . Effect of varying gap height is illustrated. Continuous data shown. Solid symbols represent critical vector angle values where jet returns from attachment to collar.

Figure 25.  $-\Delta P_{exit}$  thrust vector response curve for the  $L/H = 2, \alpha = 60^\circ$  collar at  $M_e = 0.5$  comparing operation for variable gap heights. Continuous data shown. Solid symbols represent critical vector angle values.

Figure 26.  $-\Delta P_{exit}$  thrust vector response curve for the  $\alpha = 30^\circ$  and  $60^\circ$  collars. Both collars are  $2.0H$  in length and have gap heights of  $G/H = 0.4$ . Continuous and attached data shown. Solid symbols represent critical vector angle values.  $M_e = 0.5$ .

Figure 27.  $-\Delta P_{exit}$  thrust vector response curve for all  $\alpha = 30^\circ$  collars comparing operation for differing collar lengths. Each symbol represents a separate gap height. Solid symbols represent critical vector angle values for each length.  $M_e = 0.5$ .

Figure 28. Figure 28. Maximum critical vector angle obtainable for each collar length as a function of collar length and divergence angle.  $G/H = 0.2, 0.4$ , and  $0.5$  for  $L/H = 1.0, 2.0$ , and  $3.5$  at  $\alpha = 30^\circ$ .  $G/H = 0.4$  for  $L/H = 2.0$  at  $\alpha = 60^\circ$ .  $M_e = 0.5$  for all cases.

Figure 29.  $-\Delta P_{exit}$  vector response curve for  $L/H = 1$ ,  $\alpha = 30^\circ$  collar comparing operation for variable jet exit Mach numbers. Gap height was fixed at  $G/H = 0.2$ . Both continuous and attached data are included for the  $M_e = 0.387$  and  $0.316$  cases (the  $M_e = 0.5$  and  $0.447$  cases were non-hysteretic). Solid symbols represent critical vector angle.

Figure 30. Mass flow ratio vector response curve for the same data plotted in the previous figure.  $L/H = 1.0$ ,  $\alpha = 30^\circ$  collar at  $G/H = 0.2$ .

Figure 31. Detail showing the hysteresis curves in the mass flow ratio vector response curves for the  $M_e = 0.316$  and  $0.387$  cases.  $L/H = 1.0$ ,  $\alpha = 30^\circ$  collar at  $G/H = 0.2$ .

Figure 32. Critical vector angle as a function of  $M_e^2$  for the  $L/H = 1$ ,  $\alpha = 30^\circ$  collar at  $G/H = 0.2$ .

Figure 33. Velocity ratio thrust vector response curve for the  $L/H = 1$ ,  $\alpha = 30^\circ$  collar at  $G/H = 0.2$  for variable exit Mach numbers.

Figure 34. Thrust vector response curve as a function of reverse over primary velocity ratio for the  $L/H = 2$ ,  $\alpha = 60^\circ$  collar for variable gap heights.

Figure 35. Mean Mach profiles showing the effect of suction on jet spreading for the  $L/H = 1$ ,  $\alpha = 30^\circ$  collar at  $G/H = 0.2$ . Data was taken at  $16H$  downstream of the collar exit with the y-axis aligned normal to the vector angle for each level of suction.  $M_e = 0.5$ .

Figure 36. Diagram showing the centrifugal instability of the countercurrent mixing layer when the jet is vectored close to the collar surface.

Figure 37. Thrust vector response curves as a function of gage exit pressure normalized by primary momentum flux. Data are shown for all gap heights,  $0.2 < G/H < 1.0$ , and exit Mach numbers,  $0.316 < M_e < 0.500$ , for the  $\alpha = 30^\circ$  collars. The effect of collar length is shown.

Figure 38. Collapsed universal thrust vector response curve shown when all data,  $0.2 < G/H < 1.0$  and  $0.316 < M_e < 0.500$ , from the  $30^\circ$  collars is plotted as a function of gage exit over primary jet momentum flux multiplied by  $L/H$ .

## NOMENCLATURE

A	= area
a	= speed of sound
C	= empirical constant in thrust vector angle relation
$C_T$	= thrust coefficient
$F_{Cx}$	= axial pressure force on collar
$F_{Cy}$	= side pressure force on collar
G	= counterflow gap height
H	= short exit dimension of jet
L	= collar length as measured from jet exit
M	= local mean Mach number
$M_c$	= $(u_1 - u_2)/(a_1 + a_2)$ ; local convective Mach number
$\dot{m}$	= mean mass flow rate
P	= local mean static pressure
$P_0$	= tunnel stagnation pressure
$P_t$	= local mean total pressure
$P_{wall}$	= mean static pressure at a wall
R	= local radius of curvature of a surface (such as the collar surface)
r	= cylindrical radial coordinate of curved jet
$Re_H$	= $U_1*H/v$ ; Reynolds number based on jet exit short dimension
S	= total control volume surface area
$T_0$	= tunnel stagnation temperature
U	= mean streamwise velocity at jet exit plane
u	= local mean streamwise velocity

W	= long exit dimension of jet
x	= Cartesian streamwise coordinate
y	= Cartesian coordinate along short dimension of jet exit
z	= Cartesian coordinate along long dimension of jet exit
$\alpha$	= collar divergence half angle
$\gamma$	= ratio of specific heats
$\Delta A_c$	= incremental area between collar taps (constant for each collar in this study)
$\Delta P_c$	= local static gage pressure at collar surface
$\Delta P_{exit}$	= static gage pressure in counterflow gap, "gage exit pressure"
$\Delta P_{meter}$	= pressure difference across secondary mass flow meter
$\delta_v$	= effective thrust vector angle
$\delta_{v,cr}$	= critical thrust vector angle
$\theta$	= cylindrical streamwise coordinate of curved jet
$\nu$	= dynamic viscosity
$\Sigma(\dot{m}U)_x$	= net axial momentum at jet exit plane
$\Sigma F_x$	= net axial pressure force
$\Sigma F_y$	= net side pressure force
$\phi$	= angular distance along collar wall

### Subscripts

1	= primary freestream conditions
2	= secondary freestream conditions
atm	= atmospheric or ambient conditions
e	= conditions at primary jet exit plane

$G$  = conditions at counterflow gap  
 $i$  = station or tap number  
 $j$  = "added" station number for estimated pressure distribution at end of collar  
 $m$  = number of taps downstream of exit plane pressure tap  
 $n$  = number of "added" taps for estimated pressure distribution at end of collar

## 1. INTRODUCTION

This study involves the examination of a new and innovative method for thrust vectoring. The redirection of the engine exhaust will play a large role in the performance of the next generation of military aircraft. Thrust vector control has several advantages over maneuverability strategies based on the aerodynamic control surfaces. These advantages include post-stall maneuvering, reduced takeoff distance and weight, and improvements in overall combat agility. However, many of the promising concepts currently under investigation require complicated hardware to redirect or vector the engine exhaust. This hardware typically consists of movable flaps and nozzles which add considerable weight to the aircraft and can often be expensive in terms of added drag penalty, active cooling and time response. This report will describe the operation of a fluidic thrust vectoring concept which relies on counterflow to redirect the jet exhaust. Fluidic thrust vectoring relies on fluid dynamic phenomena for control and has the advantage over existing technologies in that the control surfaces are stationary and are not exposed directly to high temperature gases. This report will also examine the role of counterflow nozzle design on bistable operation which is known to limit the utility of many fluidic nozzles. Additionally, a simple design law for determining vector angle based on geometry and operating conditions will be sought.

Technology demonstrator aircraft employing first generation vectoring nozzles have already proven the advantages of thrust vectoring under flight conditions (Mishler & Wilkinson 1992, and Capone et al. 1992). These early vectoring nozzles have developed along two different lines; rectangular or

two-dimensional, convergent-divergent (2D/CD) nozzles with pitch vectoring and axisymmetric nozzles with multi-axis vectoring. Two dimensional pitch vectoring nozzles were first employed on the USAF Short Takeoff and Landing and Maneuvering Technologies Demonstrator (S/MTD) program. The modified F-15 aircraft fitted with twin pitch vectoring nozzles demonstrated significant increased pitch rate and decreased takeoff roll using thrust vectoring. Because of these proven performance enhancements and the inherent low observable characteristics of rectangular nozzles, vectoring 2D/CD nozzles are being incorporated into the USAF's newest fighter, the F-22. Multi-axis thrust vectoring was first explored on the X-31 aircraft and on the NASA F/A-18 High Angle of Attack Research Vehicle (HARV). The multi-axis vectoring capability of these first generation systems was achieved by employing a simple system of three vanes arrayed around each nozzle exit. Even with these simple vane systems, both the X-31 and the HARV programs demonstrated the increased directional and lateral maneuverability possible with multi-axis vectoring. While these early flight demonstration nozzles proved the effectiveness of vectoring, aircraft integration issues such as weight, cooling and, particularly in the case of the vane systems, external drag were of secondary concern. Estimates of these associated nozzle penalties such as the studies done by Henderson (1990) and Doonan & Kuchar (1992) will need to continue to fully assess the viability of new thrust vector concepts.

More recently, emphasis has been given to the development of high performance multi-axis vectoring nozzles which attempt to retain the light weight design of current axisymmetric nozzles but allow deflection of the

divergent section flaps in any direction through added actuation and control hardware. Most notable of these efforts are General Electric's Axisymmetric Vectoring Exhaust Nozzle (AVEN) (Snow, 1990 and Mishler & Wilkinson, 1992) and Pratt and Whitney's Pitch/Yaw Balanced Beam Nozzle (P/Y BBN) (Bursey, Berger, & DeFreese, 1993). These axisymmetric exhaust systems are capable of vectoring up to 20 degrees in pitch and yaw at a maximum rate of up to 40 degrees per second. Also of note is Pratt and Whitney's Spherical Convergent Flap Nozzle (SCFN) (Boggs, 1993). This nozzle has a rectangular exit hinged to a spherical convergent section accommodating vectoring in both pitch and yaw axes with a 40% reduction in weight over the first generation 2D/CD pitch vectoring nozzles. Scale testing by Capone et al. (1992) has shown that the P/Y BBN and SCFN vectoring nozzle concepts have external drag levels comparable to current non-vectoring nozzles. At the time of writing (December, 1994) the General Electric AVEN had completed a limited flight demonstration on a F-16. The Pratt and Whitney P/Y BBN is similarly scheduled for flight demonstration on a F-15. Results of the AVEN testing indicate that multi-axis thrust vectoring can be successfully integrated into a production aircraft with its benefits in enhanced maneuverability realized. However, even with the relatively minor hardware differences between the AVEN and conventional axisymmetric nozzles, the flight worthy AVEN weighed 400 lbs more and was subject to increased thermal stresses. Additionally, while ideal for retrofitting current military aircraft employing axisymmetric nozzles, the AVEN and P/Y BBN nozzles would unlikely be integrated with future aircraft due to the high radar signatures of round nozzles.

While vectoring jets using variable nozzle geometry is rapidly maturing, the use of fluidic nozzle design to achieve thrust vector control remains attractive owing to the elimination of heavy control and actuation hardware. Much of the early work on fluidic jet control was carried out in the context of fluid-jet amplifiers. Studies by Olson (1962), Comparin et al. (1962), Warren (1962) and others showed that small jets could be easily directed through the use of secondary air injection and auxiliary side walls at the jet exit. Since the primary purpose of these studies was to show the feasibility of such configurations for logic control devices, these fluidic control schemes were bistable in nature. Recently, efforts by Gilbert (1991) showed that this technique could be applied on larger scales with high pressure secondary air injected either perpendicularly or tangentially into the side walls. However, this technique also suffered from bistable operation being attached to either one wall or the other with no continuous control of the vector angle. The bistable characteristic of these fluid-jet amplifier type vectoring systems limits their usefulness for aircraft control applications. However, these studies proved that jets could be effectively controlled without moving surfaces.

Fluidic control vectoring methods have also been tested on a larger scale for the application of missile or aircraft control. One such scheme was called Boundary-Layer Thrust Vector Control, examined in part by Fitzgerald & Kampe (1983) and Carroll & Cox (1983). This concept consisted of an overexpanded nozzle with control ports placed around the perimeter of the divergent section. In order to vector the jet, one of the ports was vented to ambient air, the jet separated from this side of the nozzle resulting in vectored thrust. This technique depended on the ambient pressure being

greater than the pressure in the diverging region of the nozzle. Under some flight conditions, pressurized secondary injection was required. A related fluidic vectoring concept called Confined Jet Thrust Vector Control, described by Porzio & Franke (1989), Franke (1991), and Friddell & Franke (1992) employed a chamber downstream of the convergent-divergent primary nozzle. The chamber reconverged downstream to an orifice at the exit. Small amounts of pressurized secondary air were injected into the confined chamber which forced separation but the primary jet followed the inner contour of the chamber before exhausting, resulting in vectored thrust as the jet exits through the chamber orifice. Although large vector angles could be achieved using controlled injection, continuous thrust vector control was possible over only a limited range. Furthermore, unstable operation at zero or low levels of secondary injection of these fluidic devices seriously limited their utility in aircraft applications.

Besides variable geometry and fluidic control, various other schemes for thrust vectoring have been explored. One notable study was that of Green & Glezer (1993). This study placed low power piezoelectric actuators at the exit of a rectangular nozzle. A thin sheet of steel, sandwiched between piezoelectric material, was vibrated parallel to the jet exit to excite the shear layer on one side of the jet, leading to deflection in that direction. The effect was achieved with little increase in cross stream spreading. Still another method was the use of translating side walls of underexpanded nozzles as researched by Cornelius & Lucius (1993). This method employed a simple extension of a side wall on an underexpanded nozzle. Results indicated that a 20° vector angle in one direction was achievable for both 2-D and 3-D nozzle

models with little penalty in thrust performance. Further work needs to be done to demonstrate the applicability of these concepts to full scale aircraft.

Counterflow thrust vectoring attempts to combine the continuous vector control of mechanical vectoring systems with the potential simplicity of fluidic control systems. Figure 1 shows a schematic of a counterflow vectoring system illustrating the short dimension of a rectangular jet. The primary jet exhausts from the nozzle flowing left to right between curved collars placed on either side (top and bottom in the figure) of the primary stream. To achieve upward thrust vectoring at an angle  $\delta_v$ , as shown in Fig. 1, a secondary flow must be established in the upper shear layer of the jet. This is accomplished by applying suction to the cavity between the primary nozzle and upper collar setting up the countercurrent mixing layer on the upper side of the primary stream. The interaction between the two opposing streams in the presence of the collar surface causes the primary jet to change direction.

Based on previous studies of countercurrent mixing layers as reviewed by Strykowski & Krothapalli (1993), it is anticipated that the entrainment characteristics of the two opposing shear layers give rise to markedly different pressure distributions on the upper and lower collars during vectoring, thus providing the cross stream force necessary to vector the jet. The long term goal of this research is to thoroughly investigate the mechanisms facilitated by the countercurrent shear layer for vectoring. The immediate topic of interest, however, and the main focus of this report, is the examination of the change in direction of the primary jet and how this directional change (vector angle) is affected by the counterflow and collar geometry. Countercurrent mixing layers have been examined in detail by Strykowski and others,

however, the application of counterflow for vectoring jets, to our knowledge, has only been qualitatively examined by Strykowski & Krothapalli (1993). In the present study, counterflow vectoring was modeled with a system comprised of a rectangular jet with curved, sectored arc, collars. The complete facility will be described in detail in a following section.

## 2. THEORETICAL BACKGROUND

In order to understand how fluidic vectoring is achieved, this section examines how entrainment influences jet behavior. Figure 2a depicts a two-dimensional free jet issuing from a nozzle of height  $H$ . As the jet leaves the nozzle exit, structures (not shown) in the jet shear layers entrain fluid from the surroundings, which is at essentially a constant atmospheric pressure,  $P_{atm}$ . Because the jet is gathering fluid through the entrainment process, its boundaries spread outward. Gradually, the structures traveling downstream in the jet shear layer weaken due to diffusion and their ability to entrain the surrounding fluid decreases.

Figure 2b depicts the two-dimensional jet with a curved surface of radius  $R$  aligned tangentially to the edge of the nozzle exit. The jet is seen to bend towards the curved surface. The mechanism responsible for this behavior has been described by several researchers including Squire (1950) and Wilson (1970). The fluid entrained on the lower side of the jet in Fig. 2b is constrained by the presence of the curved surface. This surface requires that the entrained fluid be replaced by ambient fluid which must flow along the surface from downstream. In order for flow to enter this constricted region, the pressure there must be less than the pressure of the surroundings. This pressure differential draws the jet toward the curved surface. It is this change in the pressure field within the vicinity of the jet that is known as the "Coanda" effect. (First described by Young (1800), the Coanda effect is named for the French engineer who patented the "effect" in 1932.) If the entrainment rate is sufficiently high, the pressure continues to drop until the jet becomes attached to the surface as seen in Fig. 3a. It is this attachment

process that is most often associated with the Coanda effect. However, attachment is not a necessary condition for the Coanda effect, but rather a result of it.

As mentioned above, Fig. 3a shows the jet attaching itself to the curved surface. The jet continues to entrain fluid between itself and the curved surface leading to further wrapping of the jet around the surface as shown in Fig. 3b. This process continues until the shear layer structures have weakened sufficiently and can no longer entrain the fluid necessary to force the jet against the surface. The point of separation of the jet from the surface is therefore dependent on the nature of the shear layer structures and their ability to entrain ambient fluid. This observation is supported by the work of McGlaughlin & Greber (1967) which showed that the angle of attached flow separation depended highly on the jet turbulence. The turbulent jets, with their higher rates of entrainment, separated farther along the curved surface than did the laminar jets of the study. McGlaughlin & Greber also showed that separation or attachment is influenced by nozzle geometry, with the higher aspect ratio jets (aspect ratio =  $W/H$  where  $W$  is the width of the nozzle exit), more closely approximating two-dimensional flow, remaining attached farther downstream.

Once the jet has established itself in the configuration shown in Fig. 3b under steady conditions, it remains stable, i.e. perturbations to this flow result in the jet reestablishing itself to the condition prior to the perturbations. While the attached portion of the jet is obviously no longer entraining fluid against the curved wall, the pressure there is kept low as demanded by the equations of motion. Referring to Fig. 3b, the curved jet can be described by

two-dimensional cylindrical coordinates  $r$  and  $\theta$  which, respectively, are the local radius of the curved jet and its angular position. Note that center of curvature of the jet may not always correspond with the center of curvature of the surface as depicted in Fig. 3b. The difference in the centers of curvature between the jet and surface are most readily apparent when the jet is not attached to the surface. In any case, the corresponding local velocities in the  $r$  and  $\theta$  directions are then  $u_r$  and  $u_\theta$ , respectively. The equations of motion for a steady, laminar, inviscid, and incompressible fluid in the absence of body forces are then:

$$\rho \left( u_r \frac{\partial u_r}{\partial r} + \frac{u_\theta}{r} \frac{\partial u_r}{\partial \theta} - \frac{u_\theta^2}{r} \right) = - \frac{\partial P}{\partial r} \quad (1)$$

$$\rho \left( u_r \frac{\partial u_\theta}{\partial r} + \frac{u_\theta}{r} \frac{\partial u_\theta}{\partial \theta} - \frac{u_r u_\theta}{r} \right) = - \frac{1}{r} \frac{\partial P}{\partial \theta} \quad (2)$$

Assuming nominally parallel flow, namely that  $u_\theta = u_\theta(r)$  and  $u_r = 0$ , then the above equations reduce to:

$$\rho \frac{u_\theta^2}{r} = \frac{\partial P}{\partial r} \quad (3)$$

Consequently, the pressure gradient in the positive  $r$ -direction is seen to increase with the square of the velocity. Therefore, the pressure will increase from some minimum value at the curved surface to the maximum level of  $P_{atm}$  attained near the outer boundary of the attached jet, ensuring that the centrifugal forces are balanced by the pressure field.

An important result of this balance between centrifugal and pressure forces was described by Rayleigh (1916). He determined that for flows in which the angular momentum increased with distance from the center of curvature would be stable while flows in which the angular momentum decreased with distance from the center of curvature would be unstable. In other words, the radial equilibrium of a fluid element is stable if the radial gradient of the circulation squared is positive ( $\frac{\partial(ru_\theta)^2}{\partial r} > 0$ ) and unstable if it is negative ( $\frac{\partial(ru_\theta)^2}{\partial r} < 0$ ). This condition is known as Rayleigh's criterion for centrifugal instability. Hence, the inner part of a jet attached to a convex curved surface will be stable since  $u_\theta$  increases radially outward from its value of zero on the curved wall surface.

The above discussion on the stability of attached jets is important for the following reasons. Many previous attempts to use fluidics in order to achieve thrust vectoring utilize the Coanda effect to deflect the jet. Fluidic vectoring concepts such as those by Gilbert (1991) and Franke and others (1989, 1991, 1992) deflected the jet by attaching it to various configurations of surfaces with the use of secondary injected air (see Chapter 1). Unfortunately, for the above reasons, once the jet attached to the surface, it stayed there, giving a limited range vectoring for a given surface configuration. Large amounts of secondary injection would then be required to detach the jet from the surface whereupon it would immediately attach itself to another surface (usually on the opposite side of the nozzle) where the jet would once again be stable. This bistability, while useful for fluid logic devices, renders the above concepts inappropriate for aircraft thrust vectoring where continuous control of the thrust vector angle is required.

Nevertheless, the use of jet entrainment to influence the direction of the jet remains attractive owing to the potential advantages of fluidic thrust vectoring systems as discussed in Chapter 1. However, the Coanda effect is passive. For a given nozzle-surface geometry and jet condition, a fixed cross stream pressure gradient distribution ( $\frac{\partial P}{\partial r}(\theta)$ ) is established along the surface. If the pressure gradient is sufficiently strong, the jet will stably attach itself to the surface as depicted in Figs. 3a and 3b. Figure 2b, on the other hand, suggests that a certain level of pressure differential gives a fixed amount of jet deflection without attachment to the surface. Since the  $\partial P/\partial r$  distribution in Fig. 2b is dependent on the level of jet entrainment, the proposition could be made that control of the jet thrust vector angle, within the vicinity of a surface, might be accomplished with active control of the level of jet entrainment. Furthermore, by limiting the level of entrainment, the jet could be made to vector up to a given angle as shown in Fig. 2b without exceeding the level of entrainment and thus the pressure differential necessary to attach the jet to the surface as shown in Fig. 3a. As a result, continuous control of the jet vector angle could be maintained without the bistability associated with attached jets.

The following question remains: how can the entrainment of the jet be manipulated to control jet vectoring? Furthermore, it is essential that any such strategy be viable in the harsh environments of most applications, with turbulent shear layers and high-temperature jets. Efforts by Lepicovsky et al. (1988) examined the influence of acoustic excitation on the mixing of high-speed subsonic jets. Results of the study found that such jets were only mildly susceptible to acoustic excitation. Attempts by Reisenthal (1988) and

others were made to control jet mixing by employing sensor/actuator based feedback systems, however, these control schemes appeared to be limited to moderate and low Reynolds numbers. Hence, utilizing external forcing techniques for influencing jet entrainment would appear to require excessive energy input, particularly in practical applications such as high-temperature supersonic flows (Raman, Zaman, & Rice, 1989). One possible exception to the above statement is the recent work of Green & Glezer (1993). This study, as mentioned in Chapter 1, showed that the shear layer of a rectangular jet could be excited utilizing low power piezoelectric actuators. The excitation led to enhanced entrainment and jet deflection. Further preliminary work by Kibens, Parekh, Joshi & Glezer (1994) has shown that this technique may be applicable at Mach numbers exceeding 1.2.

One of the more promising approaches to control mixing in jets with turbulent shear layers is through the use of counterflow. This technique does not rely on the typically poor coupling between acoustic fluctuations and vortical disturbances in the flow. Accordingly, the passive feedback of information through a countercurrent mixing layer has been shown by Strykowski & Wilcoxon (1993) to produce self-excited oscillations in the jet leading to enhanced mixing. Indeed, work by Strykowski, Krothapalli, & Wishart (1992) demonstrated that counterflow was also effective in enhancing the entrainment in supersonic heated jets.

These studies on turbulent shear layers were motivated by the earlier results by Niccum (1990) and Strykowski & Niccum (1991) on laminar shear layers showing that global instabilities within the layer were established when the velocity ratio,  $-U_2/U_1$ , exceeded 0.14. Where  $U_1$  was the mean streamwise

velocity of the primary flow and  $U_2$  was the mean streamwise velocity of the reverse flow. This value was defined as the critical velocity ratio or  $(-U_2/U_1)_{cr}$ . The presence of these global oscillations led to significant changes in the mixing dynamics of the jet.

Utilizing the circular nozzle configuration depicted in Fig. 4, the counterflow study of Strykowski & Wilcoxon (1993) established an annular countercurrent mixing layer about the axisymmetric low-speed jet ( $U_1 = 20$  to  $60$  m/sec). They observed a significant advancement in mixing using counterflow compared to the previous studies of Niccum & Strykowski due to the addition of a collar of length  $L$  placed concentrically around the nozzle of diameter  $D$ . They showed that global oscillations led to enhanced entrainment at a critical velocity ratio of  $(-U_2/U_1)_{cr} \approx 0.20$  at a collar length of  $L/D = 1$ . The enhanced mixing due to counterflow is clearly evidenced by the Schlieren photographs in Figs. 5a and 5b. Figure 5a shows the streamwise development of the jet in the absence of counterflow, which can be compared to the significant spreading of the jet in Fig. 5b at a velocity ratio of  $-U_2/U_1 \approx 0.35$ . Furthermore, Strykowski & Wilcoxon reported that the amount of counterflow necessary to achieve a given level of enhanced entrainment was reduced significantly with increased collar length and decreased counterflow slot width  $w$  (see Fig. 4).

The counterflow study of Strykowski, Krothapalli, & Wishart (1992) in circular high-speed jets used a similar nozzle-collar assembly to that used by Strykowski & Wilcoxon. These authors examined both the effect of primary Mach number, ranging from  $M_1 = 0.4$  to  $1.2$ , and stagnation temperature, ranging from  $T_0 = 20^\circ\text{C}$  to  $400^\circ\text{C}$ . The principle finding of the study was that

annular counterflow could also be used in compressible shear layers to effectively enhance jet entrainment. While the effectiveness of counterflow on jet mixing decreased with increasing primary Mach number, the critical velocity ratio was seen to drop with increasing Mach number. Thus, the study concluded that less counterflow was required to induce global oscillations within the shear layer for increasing Mach numbers, with  $(-U_2/U_1)_{cr}$  as low as 0.03 at  $M_1 = 1.2$ . Additionally, increasing the jet stagnation temperature at a fixed Mach number increased the effectiveness of counterflow mixing once the critical velocity ratio was exceeded. The results of this study together with the results of low-speed studies reveal that counterflow is both an effective and robust means of controlling and enhancing the entrainment of jets over a wide range of jet conditions.

A comprehensive overview of the application of countercurrent mixing layers for shear layer control can be found in Strykowski & Krothapalli (1993). The paper reviewed the findings of the above counterflow studies and provided further elaboration of the effect of counterflow in compressible shear layers. Most importantly, it presented the first results of the use of counterflow for jet thrust vectoring. The study utilized a rectangular supersonic Mach 2 jet in conjunction with a set of curved collars placed downstream of the nozzle exit about the long dimension of the nozzle. The collars had a fixed length of  $L/H = 7.0$ , where  $H$  was the short dimension of the 4:1 aspect ratio nozzle exit. The collars were offset a variable distance  $G$  from the nozzle exit. By controlling the amount of entrainment between the jet and collar surfaces, the authors set out to show that the jet could be vectored.

The results of the study were successful. In the absence of counterflow the jet was not affected by the presence of the collars, however, when counterflow was applied to one side of the jet, the amount of entrainment increased between the jet and the collar to which the counterflow was applied. As a result, the pressure between the collar surface and the jet was decreased relative to the ambient pressure in the manner described earlier in this chapter. Thus the jet was increasingly deflected towards the side of applied counterflow achieving thrust vector angles up to  $20^\circ$ . Not only were Strykowski & Krothapalli able to control the vector angle  $\delta_v$  using counterflow, but the jet showed little tendency to attach to the collar surface. Their study proved that counterflow could provide a means for smooth and continuous fluidic jet thrust vectoring without bistability although the physical mechanism for vectoring was not explored in detail. The aim of the present study was to begin filling the gap in our physical understanding of fluidic thrust vectoring using counterflow.

### 3. EXPERIMENTAL SETUP

#### 3.1 NOZZLE AND SUCTION COLLAR DESIGN

In order to examine fluidic vectoring in the laboratory, a free jet facility was built. The approach involved applying suction on one side of a rectangular jet through a rectangular gap as shown in Fig. 6. The suction could be applied on either side of the nozzle exit with the jet vectoring towards that side. The forward stream ( $U_1$ ) was passed through a fifth-order polynomial rigid PVC nozzle with an area contraction ratio of 19.5 to 1. The polynomial was chosen such that the slope and curvature went to zero at the entrance and exit of the nozzle. The edge of the nozzle exit formed a reference frame where the coordinate  $x$  was measured from the nozzle lip and increased in the direction of the forward stream  $U_1$ . The nozzle exit formed a 4:1 aspect ratio rectangle with the long,  $W$ , and short,  $H$ , dimensions being nominally 4 and 1 cm respectively. The counterflowing or reverse stream,  $U_2$ , was defined as the mean velocity of the flow through the suction gap in the plane of the nozzle exit (i.e. at  $x = 0$ ). The reverse velocity  $U_2$  was created by connecting a vacuum pump and manifold to the suction collar assembly.

The detail of the collar assembly, shown in Fig. 7, consisted of two collar walls positioned symmetrically about the jet centerplane, creating a cavity on either side of the primary nozzle so that counterflow could be applied independently to either side of the jet. Each collar wall consisted of two parts: a flexible Teflon portion, which formed the cavity wall and a rigid acrylic sectored arc, which extended downstream a distance  $L$  from the jet exit,

terminating with a divergence half angle  $\alpha$ . The rigid portion of the collar wall (referred hereafter as the collar) could be interchanged with other sectored arc portions in order to effect changes in collar geometry. Nine to eighteen pressure taps of 0.56 mm or 0.84 mm i.d. (depending on the collar length) were placed at equal intervals on the collar surface to capture static pressure distributions. In order to increase the density of measurements on the small collar surface, the pressure taps were staggered in two rows (three rows for the 1 cm collar) about the jet centerline. Figure 8 illustrates the distribution for one of the rows of pressure taps along the  $L/H = 3.5$  collar. A tap located in the jet exit plane to reference the conditions in the counterflowing stream is also shown. The pressure measured at this location was expressed as  $\Delta P_{exit}$ .

Collar lengths with  $L/H$  of 3.5, 2.0 and 1.0 and divergence half angles with  $\alpha$  of  $30^\circ$  and  $60^\circ$  were investigated. The height of the counterflow gap  $G$  was varied between  $0.2H$  and  $H$  through the use of adjustment screws mounted to the collar and flexible wall. Since the collars were composed of circular arcs, the collar radius of curvature,  $R$ , could be determined from the independently specified parameters of length and divergence half angle. From the collar geometry, the relationship for  $R$  is then:

$$L = R \cdot \sin \alpha \quad (4)$$

In all, four different collar configurations of different lengths and divergence half angles were examined. Several gap widths were studied for each configuration. The geometries are summarized below in Table 1.

Finally, parallel side plates spaced  $W$  apart, enclosed the collar assembly and extended downstream of the nozzle exit the same distance as the collar length. These plates were intended to minimize three-dimensional effects and further isolate the action of counterflow applied to only one side of the jet shear layers during thrust vectoring.

**Table 1. Collar configurations examined in this study**

Collar	L/H	$\alpha$	R/H	G/H Range	No. of Taps
1	3.5	$30^\circ$	7.0	0.50, 0.75, 1.0	18
2	2.0	$30^\circ$	4.0	0.25, 0.4, 0.5, 0.75, 1.0	14
3	2.0	$60^\circ$	2.3	0.25, 0.4, 0.5, 0.6	14
4	1.0	$30^\circ$	2.0	0.2, 0.25, 0.4	9

### 3.2 FORWARD AND REVERSE FLOW FACILITIES

The forward stream,  $U_1$ , was supplied by the fan-powered wind tunnel shown in Fig. 9. The fan was a 10 HP constant speed Fuji model 804A-7W ring compressor. The flow was controlled with a dual valve assembly with one valve upstream of the compressor intake, and a bypass valve branched off immediately downstream of the compressor exit. This setup allowed for fine variation in primary jet speed while allowing for proper air flow through the compressor to prevent burnout. Blower vibrations were isolated from the floor by neoprene vibration isolator mounts placed on the base of the blower. The entrance to the tunnel consisted of a 5.9 cm i.d. CPVC tube having a length of 38 cm. This section contained a TEE branch to accommodate the

bypass valve mentioned above. The bypass portion contained screens to minimize flow resonance within the TEE cavity and was ducted approximately 8 m away in order to prevent the hot bypass air causing a temperature rise in the immediate area of the blower.

The entrance section was followed by a 54 cm long rectangular stainless steel diffuser section which diverged from a  $6.0 \times 6.0$  cm section to a  $19 \times 15$  cm section. Total included angles for the diffuser were  $14^\circ$  for the long dimension and  $9.7^\circ$  for the short dimension. A perforated metal plate with 63.4% blockage was placed at the entrance to the diffuser in order to smooth the flow entering from the connecting tube. Exiting the diffuser, the flow entered an air-to-water heat exchanger. The  $19 \times 15 \times 5$  cm fin type galvanized steel heat exchanger was an ordinary automobile heater core and was contained within a flanged sleeve which could be removed if necessary. Its purpose was to reduce the  $+75^\circ$  C temperature rise at maximum flow rates resulting from the ring compressor. Water flow rates through the heat exchanger were maintained between 23 and 30 liters per minute in order to minimize air temperature variation across the heat exchanger exit. From the heat exchanger, the flow entered a rectangular-to-round transition section. The exit of the transition contained a high blockage perforated plate in order to condition the flow leaving the heat exchanger. The flow then entered a large aspect ratio honeycomb flow straightener followed immediately by a mesh screen in the manner recommended by Loehrke & Nagib (1976) for freestream turbulence control.

Following this initial flow setup portion of the tunnel, the flow entered a plenum chamber of 12.7 cm diameter. The plenum contained

several screen sets and provisions for thermocouple insertion. The circular plenum then changed to a  $7.6 \times 10.2$  cm rectangular flow path over a 15.2 cm transition section. This transition section then terminated at the nozzle assembly previously described. The total system length was approximately 3.5 meters. Tunnel performance and verification is described in the following section.

The reverse flow portion of the system (Fig. 10) was powered by another Fuji ring compressor (2.5 HP, model 503A-7W), operating in vacuum mode. The reverse flow was drawn from four 1.27 cm (1/2") o.d. brass tubes in the collar assembly through 1.25 cm i.d. flexible vinyl tubing of equal lengths. The vinyl tubing was clamped securely about brass tubes to minimize leakage and led to a 7.6 cm i.d., 3 m long manifold chamber. In this way, the reverse flow stream  $U_2$  was effectively isolated from any pump pulsations. A laminar flow meter consisting of honeycomb flow straightener was contained within the suction manifold to obtain the mass flow rate of the reverse stream,  $m_2$ . Reverse flow rate was controlled using a dual valve assembly similar to that used for control of the primary jet.

### 3.3 INSTRUMENTATION AND DATA ACQUISITION

The majority of the data consisted of pressure measurements acquired with MKS Baratron Type 223B transducers. Two-way differential heads of 100 and 1000 torr were used for static wall pressures and primary jet pitot surveys, respectively. The small pressure drops across the laminar reverse flow meter were determined using a MKS Baratron Type 398 HD transducer with a 1 torr differential head along with the MKS 270B signal conditioner. Signals from

the transducers were processed through a Keithley 194a dual-channel digitizer. The digitizer could sample at rates up to 100 kHz while retaining 16-bit resolution. Final data processing was performed on an Everex 386 workstation. The complete data acquisition system is shown in Fig. 11.

Ease and speed of the data acquisition were greatly enhanced through the use of automation. The multiple pressure measurements required to determine the collar static pressure distribution was facilitated by a Scanivalve 48J9-1 pressure sampling scanner. This device was connected to the collar wall taps via 1.5 mm i.d. vinyl tubing and its single output to the Baratron transducer. The Scanivalve scanner is illustrated linked to the data acquisition system also in Fig. 11. The solenoid driven scanner was controlled by the Scanivalve CTLR2/S2-S6 allowing both manual and remote operation of the scanner. The remote circuits of the controller were switched using logic driven relays connected to a IEEE data bus originating from the Everex workstation. Data acquisition programs could then step the scanner through the pressure ports and take data in any manner input into the program. IEEE control was provided by a Superior Electric Modulynx - Slo-Syn motion control system which contained a IOD012 I/O card for driving the logic relays. The motion control system was also capable of driving a two axis automated traverse system.

### 3.4 FLOW VISUALIZATION

Flow visualization was helpful in determining the extent of thrust vectoring during preliminary studies. The jet was illuminated by creating laser sheet images of the vectored plane along the jet axis using an American

Laser Co. Model 909 5W Argon ion laser. Roscoe stage smoke, injected into the facility upstream of the nozzle, was used for light scattering. Photographs were taken with a Nikon F3 35 mm camera equipped with a Nikon 50 mm focal length F1.8 lens. In order to facilitate camera and laser placement when the flow visualization photographs were taken, the rectangular nozzle was placed on its side so that the long axis was perpendicular to the laboratory floor. Thus the laser and the beam spreading optics could be placed horizontally on an adjacent bench. The camera was then placed on a stand above the nozzle so that it could shoot downward along the long dimension of the exit at the laser sheet. Jet exit velocity was also slowed down during the flow visualization studies so that the smoke would not be dispersed too quickly. Therefore, while most numerical data were obtained at exit Mach numbers between 0.3 and 0.5 (up to approximately 170 m/sec), the flow visualization runs were made at exit velocities of approximately 30 m/sec. Images of the vectoring jet made with this setup were useful for determining thrust vector angle under certain counterflow conditions as well as qualitatively understanding the jet behavior.

## 4. FLOW CONDITIONS

### 4.1 "STANDARD" JET

In this portion of the paper the characteristics of the jet without reverse flow (hereafter referred to as a "standard" jet) will be described. Two configurations of the standard jet were examined: 1) without the collar assembly attached to document the baseline jet initial conditions, and 2) with a representative collar attached to illustrate its effect, if any, on the standard jet. Total head pitot measurements were utilized to obtain the local mean total pressure ( $P_t$ ) and therefore the mean streamwise Mach number in the flow field. A Cartesian coordinate system ( $x, y, z$ ), as shown in Fig. 12, was chosen for these initial condition studies. Its origin was located at the center of the nozzle exit with the  $x$ -axis oriented along the jet centerline. The  $y$  and  $z$ -axes were oriented along the short and long dimensions of the jet exit, respectively. Care was taken in positioning the probes so that all traverse mechanisms and support structure were placed outside of the shear layer. An automated two-axis motor driven Velmex UniSlide traverse system was aligned with the  $x$  and  $y$ -axes. Small manual linear traverses, Newport model 430, were mounted on the UniSlide system. The manual traverses provided a spatial resolution of 0.001 mm and were used for fine probe positioning along the  $y$  and  $z$ -axes. The constant speed ring compressor provided steady operation of the facility over the course of an experimental run (typical run times were 1-2 hours). The tunnel mean stagnation pressure,  $P_0$ , was found to vary by less than 0.5% over this time period. Additionally, the heat exchanger minimized temperature fluctuations keeping the

variation of mean stagnation temperature,  $T_0$ , within  $0.3^\circ C$  over the run time. The facility provided constant and repeatable operating conditions during the course of the study.

It was desired to operate the the jet-wind tunnel at its maximum velocity in order to minimize the bistability of the jet in the presence of the collar (this is explained in detail in following sections). The Fuji 408A ring compressor was capable of driving the facility at velocities up to 180 m/sec. Because of the compressibility effects at this velocity and since the temperature was typically different ( $\pm 10^\circ C$ ) from the ambient temperature ( $T_0$  was a strong function of primary flow rate and heat exchanger water temperature), the study was conducted using primary stream exit Mach number ( $M_e$ ) rather than velocity as the relevant parameter. The exit Mach number was therefore fixed at 0.50 (167 m/sec at  $T_0 = 20^\circ C$ ) for the majority of the study giving an exit Reynolds number based on the jet short dimension as  $Re_H = 1.16 \times 10^5$ .

Typical mean Mach profiles (local Mach number normalized by  $M_e$ ) taken along the two central planes (y and z-axes) of the nozzle exit for the standard jet without the collar assembly are shown, respectively, in Figs. 13a and b. The profiles were taken immediately downstream of the nozzle exit and are characterized by their top hat shape with no discernible overshoot at the shoulders. Although Fig. 13 is for a flow condition of  $Re_H = 116,000$  ( $M_e = 0.5$ ), the profile is typical of all flow speeds investigated. The mean Mach profile along the y-axis at the nozzle exit for the standard jet with the collar assembly attached is shown in Fig. 14 at the same flow conditions. The collar used in the initial condition studies had a length of 1 cm ( $L/H = 1.0$ ), a

divergence half angle  $\alpha$  of  $30^\circ$  and was offset a distance of 2 mm ( $G/H = 0.2$ ). This particular collar geometry was chosen primarily for its narrow gap width (much data for the study was taken at this geometry as well) which would most likely have the greatest effect on initial jet conditions. As with Fig. 13a, the profile with the collar exhibits a clean top hat shape that is nearly identical to the profile taken with the no collar jet. The influence of the collar on the "standard" jet is therefore negligible near the exit plane. The exit profile along the z-axis for the collar case was not taken due to the presence of the side plates.

Comparisons of the downstream Mach profiles with and without the collar were made in the y-plane at  $x/H$  values ranging from 10 to 40. The downstream profiles, shown in Fig. 15a for  $x/H$  of 10 and 20 and Fig. 15b for  $x/H$  of 30 and 40, show the symmetrical spreading of the standard jet as it moves downstream. The downstream Mach profiles with the collar have lower velocities near the center line of the jet and exhibit a slightly larger spreading rate than the profiles measured without the collar. This is particularly noticeable for  $x/H$  greater than 10. This behavior is most likely due to the influence of the side plates placed at the edges of the jet exit. The shear layers are probably forced slightly in the immediate neighborhood of the collar giving rise to more shear layer structures and mixing which is then seen as increased spreading in these y-plane profiles. These mean pitot profiles compared the standard jet with and without a representative collar attached and typify the base flow conditions in the forward jet stream.

## 4.2 "COUNTERFLOWING" JET

As stated previously, the goal of this study was to examine the effectiveness of vectoring a rectangular free jet using a countercurrent mixing layer. This study measured the change in direction of the jet (using a method to be described) under the influence of asymmetric counterflow under differing geometric and flow conditions. The goal of this section is to present and discuss the methods, and difficulties encountered, in obtaining these measurements in an experimental study.

### 4.2.1 Introductory Comments

Before proceeding, a note on the variables used in this study needs to be made. As mentioned above, the jet vectoring angle,  $\delta_v$ , was used as the measure of merit. The different nozzle-collar geometric parameters used in the study, such as  $L$ ,  $G$  and  $\alpha$  have been mentioned previously. The short dimension,  $H$ , of the nozzle exit, was used as the primary length scale for normalization. The use of  $H$  in this manner was appropriate for these near field studies and was consistent with other studies of rectangular jet mixing (see Grandmaison, Pollard, & Ng, 1991 and Shih, Krothapalli, & Gogineni, 1992). The impact of nozzle-collar geometry on fluidic controlled jets is significant as demonstrated by many fluid-amplifier studies and Coanda control papers (a representative sample of these studies would include Olson, 1962; Warren, 1962; and McRee & Moses, 1967). Because of the strong effect that collar geometry has, one of this study's primary goals was to examine counterflow vectoring under geometrical changes.

However, measuring the changes in flow conditions were not as straightforward. In order to achieve active control of the vectoring jet for a given configuration, the amount of counterflow or suction must be varied and then measured and compared to the vector angle achieved. Several parameters could be used in order to measure the amount of counterflow. Typically, counterflow studies such as those by Niccum (1990), Strykowski & Niccum (1991) and Strykowski & Wilcoxon (1993) have used velocity ratio across the mixing layer to express the parameter space. Where velocity ratio has been expressed as  $-U_2/U_1$ .

The above studies involved axisymmetric counterflow, which was modeled on an infinite-planar shear layer and correlated with linear stability theory. However, with asymmetric counterflow applied to a vectoring jet, the relevant velocity ratio is not so easily defined. Due to the deflection of the jet toward the curved collar wall, the gap between the jet and the wall will be narrower midway down the length of the collar than it is at the jet exit plane. The velocity ratio will then vary along the collar, making the applicable velocity ratio difficult to ascertain. Additionally, without a means of non-intrusive measurement, such as laser Doppler velocimetry, there was no way to directly determine the reverse flow velocity as a function of collar length. Consequently, the reverse velocity was defined in the present study as the average value measured in the jet exit plane at  $x = 0$ . This value for reverse velocity was obtained by measuring the mass flow of the secondary stream and assuming that the secondary stream was uniformly distributed across the gap  $G$  at  $x = 0$ .

Because of the difficulties with determining the "true" velocity ratio, guidance was taken again from Coanda and fluid amplifier studies in

determining the relevant primary parameter space for this problem. Many Coanda effect studies examine the influence of wall or bubble pressure (pressure measured on the Coanda surface within the point of jet attachment) on the behavior of the attached jet. The fluid amplifier studies of Comparin et al. (1962) and Warren (1962) and the fluidic vectoring papers of Franke (1991) and Gilbert (1991) utilized secondary or control pressure (pressure supplied by the control ports of the fluidic system) as a means of determining the effectiveness of their system in deflecting the primary jet. When multiplied by the area of application, the bubble or secondary pressure gave these researchers the amount of force acting on the primary jet. Since this study dealt with the deflection of a primary jet under fluidic forces, reverse flow suction pressure was considered to be a primary variable for counterflow vectoring. This suction pressure or gage exit pressure,  $-\Delta P_{exit}$  (the negative sign in the expression emphasizes the fact that these pressures were below the ambient pressure), was measured in the nozzle exit plane by a collar wall tap as shown earlier in Fig. 8. The gage exit pressure could be repeated from day to day by adjusting the valves of the reverse flow assembly (see Fig. 10). Because of these reasons, gage exit pressure proved to be an easy and accurate metric for the study of jet deflection by countercurrent mixing layers.

#### 4.2.2 Reverse Flow Calibration

While gage exit pressure,  $-\Delta P_{exit}$ , was extremely useful as a benchmark in measuring vectoring performance, it did not provide physical insight into the flow dynamics within the nozzle-collar assembly. Therefore, the decision was made to monitor the reverse mass flow rate as measured at the jet exit

plane and use reverse to primary mass flow ratio,  $\dot{m}_2/\dot{m}_1$ , in addition to  $-\Delta P_{exit}$  as a primary study parameter. The mass flow ratio would indicate what the flow requirements were for vectoring the primary jet to a given angle and collar geometry.

In order to measure the amount of reverse flow, a 45 cm long section of aluminum honeycomb flow straightener was placed within the reverse flow manifold chamber as shown in Fig. 10. Static pressure wall taps were placed at each end of the honeycomb section in order to measure the pressure drop,  $\Delta P_{meter}$ , across it. While not long enough to be considered a true "laminar" flow meter, the meter could be calibrated to give accurate and repeatable mass flow rates correlating to measured differential pressures across the honeycomb section. In order to obtain the calibration, a large, 0.0026 to 0.026 kg/sec (4.6 to 46 SCFM), rotameter, Omega model FL1660, was placed in line between the honeycombed section and the vacuum compressor. Visual readings of the rotameter were taken while the 1 torr head pressure transducer monitored  $\Delta P_{meter}$ . The transducer was sampled for 10 seconds at 500 Hz by the voltmeter during each reading. The calibration curve is shown in Fig. 16. The data in the plot were taken over the course of a day with many points repeated and, as can be seen, were highly consistent. The data are seen to be nearly linear as expected by these types of flow meters. However, the data were fitted with the second order polynomial curve:

$$\dot{m}_2 = 5.243 \times 10^{-4} + 5.694 \times 10^{-5}(\Delta P_{meter}) - 1.998 \times 10^{-8}(\Delta P_{meter})^2 \quad (5)$$

with units of kg/sec for  $\dot{m}_2$  and mtorr for  $\Delta P_{\text{meter}}$ . With great care taken in making sure the collar cavity and tubing connections were well sealed to prevent leakage, the above expression could be subsequently utilized to define the reverse flow rate through the collar gap with repeatable and consistent results.

Once the reverse mass flow rate was known, the average reverse velocity  $U_2$  could be calculated in the jet exit plane for a given gap height, i.e.  $U_2 = \dot{m}_2 / (\rho_2 * G * W)$ . However, the local reverse flow velocity, which is designated here as  $u_2$ , is actually a function of the distance downstream of the nozzle, or  $u_2 = u_2(x)$ , as explained in Section 4.2.1. Nonetheless, the reverse stream velocity defined as  $U_2 = u_2(x = 0)$  gave a velocity ratio,  $-U_2/U_1$ , that was used with some success in this study.

One final note on terminology. Both gage exit pressure,  $-\Delta P_{\text{exit}}$ , and reverse mass flow rate,  $\dot{m}_2$ , have been described as being useful parameters for this study. Both indicate conditions in the counterflowing stream. Often times the relation between these two parameters is monotonic and they can be used interchangeably, i.e. a larger  $-\Delta P_{\text{exit}}$  value results in increasing  $\dot{m}_2$ . However, there are many instances, such as jet attachment to the collar (attachment is explained in detail in the following chapter, Figs. 22 and 23) where large increases in  $-\Delta P_{\text{exit}}$  result in decreased levels of reverse mass flow rate. Because of this discrepancy, the term "suction" is used when describing relative levels of gage exit pressure  $-\Delta P_{\text{exit}}$ . The expression "counterflow" is used when describing relative levels of reverse mass flow rate  $\dot{m}_2$ .

#### 4.2.3 Vector Angle Determination

Since the thrust vector angle,  $\delta_v$ , achieved by the jet with counterflow applied was the main figure of merit for this research, a way of quantifying  $\delta_v$  had to be devised. Without a thrust balance stand, probably the most straight forward way of finding  $\delta_v$  was to use flow visualization. At the beginning of this research, the nozzle-collar assembly was fitted with non-instrumented collars made of aluminum sheet that were easily reshaped. This setup allowed a number of configurations to be examined within a short time in order to obtain a preliminary understanding of the behavior of counterflow vectoring. Jet thrust vector angles generated from this preliminary configuration were determined using the flow visualization techniques described in Section 3.4. Vector angle was easily estimated by measuring the angle between a line drawn through the visual center of the jet plume and the x-axis of the nozzle. Examples are illustrated by the photographs shown in Figs. 17b-d using a pre-test collar of zero length and gap height of  $G/H = 0.7$ . The images were 1 msec exposures of the jet side view extending downstream of the primary jet exit from approximately  $2.5H$  to  $28H$ . The vector angles, estimated from the photographs, were  $6^\circ$ ,  $13^\circ$ , and  $27^\circ$  respectively. In order to prevent excessive particle dispersion, the flow conditions for Fig. 17 were at a relatively low forward velocity of  $29$  m/sec ( $Re_H = 1.85 \times 10^4$ ). While flow visualization was a direct and accurate means of determining vector angle, the setup and particle seeding required for the laser and the restrictions on flow velocity made it impractical for use under the desired test conditions.

Another method used for vector angle determination was the use of downstream total pressure profiles in the y-plane. Using the automated traverse system described in Section 3.3, y-plane pitot surveys of the flow field at several  $x/H$  locations would indicate the position of the jet during vectoring. For large vector angles, the technique required that the probe be nominally aligned with the vectored flow. Alignment was accomplished by mounting a small manually operated turntable, Newport model RSP-2, with 1 degree resolution onto the UniSlide traverse. The probe could then be rotated into the approximate direction of the vectored jet. By programming the automated traverse with the approximate vector angle as an input, both axes of the UniSlide traverse system could be driven so that y-plane profiles could be taken about an x-axis that aligned itself nominally with the jet. In other words, the coordinate system of Fig. 12 was transformed so that the x-axis was rotated to the angle set on the turntable. Additionally, the origin of the transformed coordinate system was moved to the collar exit plane rather than the nozzle exit. In this way, the origin of the transformed coordinate system was situated closer to the origin of the jet vector rotation.

Figure 18 shows an example of downstream Mach profiles taken in this way. The figure depicts profiles in the y-plane taken from 2 to 16H downstream of the collar exit plane for the  $L/H = 1$ ,  $\alpha = 30^\circ$  collar at a gap height of  $G/H = 0.2$ . Suction (in terms of gage exit pressure,  $\Delta P_{exit}$ ) was set at approximately -50 torr. The increasing offset of the profiles indicates that the probe was aligned about a rotation angle that was less than the true jet thrust vector angle (suction is applied to the positive side of the y-axis). In this case the turntable was set to an angle of  $10^\circ$  but the drift in the peak velocities of

the profiles indicated the true jet vector angle was 13°. Downstream pitot surveys provided a very accurate means for quantifying the jet thrust vector angle at the test conditions. Because of its accuracy, this method was used periodically throughout the study. However, because the profiles required a significant amount of time to acquire (the five profiles in Fig. 18 took over 4 hours of run time), the pitot survey method was not practical for measuring vector angles for a large number of collar configurations at different levels of suction.

The method used extensively throughout this study for determining jet thrust vector angle was based on a control volume analysis. The control volume method provided a quick and accurate means of estimating vector angle under any flow conditions. A detailed description of the control volume analysis is found in Appendix A. However, a quick overview follows here.

A relevant control volume (see Fig. 19) was drawn from the nozzle exit plane to just downstream of the collar exit so that this boundary could be considered to be at ambient conditions. A balance of the surface pressure forces and momentum fluxes through the control volume provided an estimate of the effective angle of the vectored thrust,  $\delta_v$ . The pressure distributions on the active collar from the static wall taps located there were integrated to obtain the resultant forces acting on the collar surface,  $F_{cx}$  and  $F_{cy}$ . Sample measurements of the pressure distribution along the inactive collar (the collar wall opposite to the side of vectoring, i.e. the side with no applied suction) showed that the gage pressures there were on the order of 0.5% that of the active collar and hence could be reasonably neglected. The

static gage exit pressure  $\Delta P_{exit}$  was estimated to be uniform across the counterflow gap height  $G$ , while the flow in the primary stream was assumed to exhaust ideally to atmospheric pressure in the nozzle exit plane. The primary momentum flux at the nozzle exit plane could be estimated with a high degree of certainty from the centerline total pressure measurement due to its top hat velocity profile there (refer to Figs. 13 and 14). Secondary velocity  $U_2$  was approximated by assuming the measured mass flow rate  $\dot{m}_2$  was distributed uniformly across the gap height  $G$ . In the absence of a direct force balance on the nozzle-collar assembly, viscous drag was not included in the calculations.

Employing these measurements and assumptions, the effective thrust vector angle of the jet was calculated using the expression (refer to Appendix A for a detailed derivation):

$$\delta_v = \tan^{-1} \left[ \frac{\Sigma F_y}{\Sigma(\dot{m}U)_x + \Sigma F_x} \right] \quad (6)$$

where  $\Sigma F_x$  and  $\Sigma F_y$  represent all the pressure forces in the x-direction (such as  $F_{cx}$  and pressure force exerted normal to the gap height) and y-direction (such as  $F_{cy}$ ), respectively. Likewise,  $\Sigma(\dot{m}U)_x$  represents all the momentum fluxes acting along the x-axis (i.e.  $\dot{m}_1 U_1$  and  $\dot{m}_2 U_2$  at  $x = 0$ ). The control volume analysis also provides the thrust coefficient defined here as:

$$C_T = \frac{\sqrt{[\Sigma(\dot{m}U)_x + \Sigma F_x]^2 + (\Sigma F_y)^2}}{(\dot{m}U)_1} \quad (7)$$

which indicates the magnitude of the pressure and momentum losses associated with the turning of the jet due to counterflow, i.e. the resultant momentum flux leaving the control volume in the direction of  $\delta_v$  is considered to be  $(\dot{m}U)_1$  multiplied by  $C_T$  (see Fig. 19 and Appendix A). The accuracy of the control volume method as compared to the other techniques for quantifying vector angle is examined in detail in the following chapter.

#### 4.2.4 Measurement Techniques

This section reviews the data acquisition process and assumptions made to determine vector angle using the control volume method in a typical run. With the facility fitted with the desired test collar and the gap height set with the adjustment screws, the facility was allowed to come into equilibrium, taking approximately one hour run time. The jet exit Mach number  $M_e$  was then measured with a pitot probe at the jet exit plane. The valve assembly controlling the primary flow rate from the tunnel compressor (see Section 3.2 and Fig. 9) was then adjusted to achieve the desired exit Mach number. Tunnel stagnation temperature  $T_0$  was then measured and recorded using the thermocouple located in the tunnel plenum. With the initial conditions established, suction was applied by opening the valve in the reverse flow assembly (see Fig. 10). Since the pressure transducer was hooked to the  $\Delta P_{exit}$  tap (collar station 0) through the home port of the Scanivalve, the amount of suction was monitored by reading the transducer voltage output on the display panel of the voltmeter. The reverse flow could then be throttled with the valve assembly until the desired  $\Delta P_{exit}$  value was achieved. At this point, the data acquisition program was started, stepping

the Scanivalve through each of the collar pressure taps. Each pressure reading was sampled for 45 seconds at 500 Hz with the average pressure written to a file for later processing. For each collar static pressure measurement, the second channel of the Keithley 194a voltmeter sampled the output of the 1 torr head transducer measuring the pressure drop over the reverse flow meter. These readings were also recorded so that an average reverse flow rate could be determined for the whole run. After the Scanivalve had stepped through all the ports and a complete collar pressure distribution had been recorded, the data acquisition program terminated with the Scanivalve returning to the  $\Delta P_{exit}$  port so that another suction level could be set and the process repeated.

Gage collar static pressures,  $\Delta P_c$ , obtained from the  $L/H = 2$ ,  $\alpha = 60^\circ$  collar for a gap of  $G/H = 0.4$  are shown in Fig. 20. The profiles in the plot are referenced by the gage exit pressure  $\Delta P_{exit}$  developed in the gap for each level of suction (i.e. at collar pressure tap 0). The pressure distributions vary somewhat smoothly from the jet exit at station 0 to station 13 near the end of the collar (station 13 was located at an angular location of  $52^\circ$  or 3 mm arc distance from the end of the  $60^\circ$  collar). Some slight jaggedness is seen in the profiles near the jet exit especially at the higher levels of suction. This variation in the pressure is most likely due to some spanwise pressure variation as seen by the taps which were staggered in two rows about the centerline of the collar (see Section 3.1). The profiles in Fig. 20 are seen to approach atmospheric pressure near the end of the collar as expected. The gage collar pressures do not reach zero gage pressure since the last tap (station 13 for the  $60^\circ$  collar) is not located at the collar end as explained above (see

detailed sketch in Fig. 8). The negative pressure measured there is most likely a result of the local acceleration of the reverse flow over the sharply rounded collar lip.

With the collar pressures recorded, the profiles were integrated over the area of the collar in order to obtain  $F_{cx}$  and  $F_{cy}$  (see Appendix A for a description of the numerical integration process). These values were then used along with the primary and reverse mass flow value to calculate  $\delta_v$  for each level of suction using Eq. (6).

Because the pressures over the collar area from the last tap to the collar end could not be accurately measured, the collar pressure distribution had to be estimated in this region. This addition to the profile was constructed by inserting points during the integration with values distributed linearly between the final recorded value at the last (farthest downstream) tap and zero at the end of the collar (see Appendix A for a detailed description). Any errors in  $\delta_v$  introduced by this estimated addition to the collar pressure profile were minimal since the pressure acted nearly parallel to the y-axis. Therefore, the impact on  $F_{cy}$ , and therefore  $\delta_v$ , was minimal. Additionally, the assumption that the gage collar pressure went to zero at the collar end was felt to be reasonable since the pressure would have to be atmospheric at the end where conditions were quiescent.

The basic flow has now been described in terms of mean values, scaling parameters, and reverse flow conditions. Measurement techniques as well as vector angle calculation have also been examined. The remaining sections of the paper evolve around how the jet is vectored due to the presence of

reverse flow under different geometric constraints. Lastly, this paper attempts to explain the mechanisms responsible for these flow alterations.

## 5. RESULTS AND DISCUSSION

In previous sections of this report, arguments were put forth that free rectangular jets could be effectively vectored through the application of asymmetric counterflow. Furthermore, such vectoring could have distinct weight and complexity advantages over the current mechanical vectoring schemes and avoid the bistability problems associated with other fluidic vectoring approaches. Here, these arguments are supported with the presentation of experimental results on the study of a counterflowing vectoring jet. The general behavior of the vectoring jet is described in Section 5.1. The thrust vector angle is examined as a function of both gage exit pressure and mass flow ratio in order to provide insight into the vectoring process. In Section 5.2, a parametric study of collar geometry effects on vectoring performance is presented with the effects of  $G/H$ ,  $\alpha$ , and  $L/H$  considered. Section 5.3 shows the effect of primary flow conditions while 5.4 pulls the study together with a dimensional analysis of the counterflow vectoring process as well as provides some insight into the responsible mechanisms. Finally, Section 5.5 concludes the presentation with a scaling curve in which the vector angle can be predicted from a given set of flow conditions and collar geometry through the use of a simple design law.

### 5.1 PRELIMINARY OBSERVATIONS

The response of the jet with applied counterflow is shown in Fig. 21 where vector angle  $\delta_v$  is plotted as a function of negative gage exit pressure  $-\Delta P_{exit}$  (data are from the  $L/H = 2$ ,  $\alpha = 60^\circ$  collar at a gap height of  $G/H = 0.4$ ). Vector angle values for the solid symbols were obtained using the control

volume method with each point requiring a full collar pressure distribution for calculation. Several of the data points in Fig. 21 used the pressure profiles displayed in Fig. 20. The control volume predictions were compared to the angles determined from mean downstream Mach profiles represented by the open symbols. The agreement between the predictions of  $\delta_v$  suggests that the assumptions employed in the momentum balance of the nozzle-collar system were reasonable.

The thrust vector response curve in Fig. 21 predicts a nearly linear relationship between effective thrust vector angle and gage exit pressure over the range of conditions studied. The data falls into two groups. On the lower portion of the curve, points could be vectored from  $0^\circ$  to approximately  $20^\circ$  in a repeatable manner. The upper portion of the curve shows a cluster of points at a vector angle of nearly  $50^\circ$ . This upper value was limited by the collar geometry and is discussed in the following section. Stable thrust vectoring was not possible between  $20^\circ$  ( $-\Delta P_{exit} \approx 50$  torr) and  $50^\circ$  ( $-\Delta P_{exit} > 100$  torr). This gap in the data was a result of bistable jet behavior and is best explained by examining Fig. 22.

Figure 22 represents the same data as in Fig. 21, however, this time  $\delta_v$  is shown as a function of mass flow ratio  $\dot{m}_2/\dot{m}_1$ . The most striking characteristic of this plot is the hysteresis loop formed by the data. At low levels of reverse flow (region (a) on Fig. 22), the thrust vector angle increases monotonically with  $\dot{m}_2$  much as it did with gage exit pressure. As the vector angle increases, the jet moves closer to the collar wall thereby reducing the area available for the reverse flow. Hence, a decrease in secondary mass flow occurs, which for this collar geometry and flow conditions occurs when  $\delta_v$

exceeds approximately  $10^\circ$  (see region (b) on Fig. 22). Eventually, the pressure between the primary jet and the collar wall becomes sufficiently low that the jet can no longer stably remain in region (b). At this point, the jet rapidly attaches itself to the collar as depicted in the upper insert diagram in Fig. 22. This attachment results in an increase in  $\delta_v$  from  $19^\circ$  to  $49^\circ$  (region (c) in the figure) as highlighted by the upwards pointing arrow in the main plot. At this point, the jet is attached near the collar end (see discussion below associated with Fig. 23a). With the jet attached, we anticipate that no reverse flow can be drawn from outside the collar but rather originates from the primary jet. Because the suction gap is blocked in this manner, both mass flow ratio and gage exit pressure drop dramatically as seen in Figs. 22 and 21 respectively.

Once the jet is attached to the collar, closing the control valve to its position prior to jet attachment has no noticeable effect on jet position. The control valve must be closed considerably, reducing the suction (decreasing  $-\Delta P_{exit}$ ) to the point where the momentum of the jet overcomes the vacuum built up between the jet and the collar surface. The jet then releases from the collar, establishing an equilibrium position at the intersection of the downward arrow and the lower curve. This point will be called the critical vector angle  $\delta_{v,cr}$  indicating the maximum angle achievable without hysteresis effects. Since the reverse flow control valve was closed considerably to allow jet detachment, the jet returns to a smaller angle of about  $5.5^\circ$ , thereby defining  $\delta_{v,cr}$  which apparently depends on the condition of the attached jet. Therefore, a hysteresis loop is formed, similar to that described by Gilbert (1991) during his research on fluidic vectoring jets.

The loop defines a bistable regime where the jet is either controlled smoothly and continuously with counterflow or attached to the collar. Indeed, for this collar geometry, once the vector angle exceeds  $5.5^\circ$ , large disturbances to the jet column (such as a hand or other object inserted into the flow) results in the attachment of the jet. Below a  $\delta_v$  of  $5.5^\circ$ , the jet was completely stable with no disturbance able to make the jet attach to the collar wall. Clearly, for the collar geometry represented in Fig. 22, the  $5.5^\circ$  critical vector angle marks a boundary beyond which the jet becomes bistable.

The critical vector angle  $\delta_{v,cr}$  should, for practical applications, be increased above the value of  $5.5^\circ$  illustrated for the conditions of Fig. 22. However, the qualitative behavior presented in Figs. 21 and 22 were typical of most cases studied and serve as a good illustration of the general behavior of a counterflow vectoring jet. As will be shown in the section to follow, performance of the system is highly dependent on the nozzle-collar geometric configuration which can be optimized for specific applications.

Further insight into the attached jet behavior can be obtained by examining collar pressure distributions. Figure 23a shows attached jet pressure profiles for the same geometry ( $L/H = 2$ ,  $\alpha = 60^\circ$ ,  $G/H = 0.4$ ) as shown in Fig. 20 for the unattached jet. Both the unattached profiles (Fig. 20) and the attached profiles (Fig. 23a) vary smoothly from  $\Delta P_{exit}$  at the nozzle exit plane (station 0) to near atmospheric pressures at the collar end (station 13). However, a partial vacuum is created by the attached jet, resulting in pressures near the exit plane which are much lower than in the unattached cases shown in Fig. 20. This vacuum pressure (negative gage pressure) extends from station 0 increasing slightly to station 6, marking the portion of

the collar wall within the separation bubble formed behind the attached jet (see inset diagram in Fig 23a). The bubble, described in the fluid amplifier study of Warren (1962), consists of relatively low kinetic energy flow diverted from the primary jet. The negative gage collar pressure  $-\Delta P_c$  drops quickly after station 6 indicating the region of the collar exposed to impingement by the attached jet. Since the jet was attached only to the extreme tip of the  $\alpha = 60^\circ$  collar end for the suction levels studied,  $-\Delta P_c$  does not quite return to zero at station 13.

Figure 23b shows attached jet pressure profiles for the  $L/H = 3.5$ ,  $\alpha = 30^\circ$  collar at  $G/H = 0.75$ . These data are shown to illustrate the effect of varying suction (increasing or decreasing  $-\Delta P_{exit}$  by respectively opening or closing the suction control valve) when the jet is attached. As with the  $\alpha = 60^\circ$  collar, the vacuum bubble is well defined with a rapid increase in collar pressure. What these curves show clearly, though, is the shrinkage of the vacuum bubble with increasing  $-\Delta P_{exit}$ . At a  $-\Delta P_{exit}$  of 47 torr, the jet seems to be attached near the end of the collar past station 17 since the gage pressures there are still negative. As suction is increased, the pressure distribution becomes more compact indicating that the point of jet attachment is moving up the collar. At  $-\Delta P_{exit} = 55$  torr, the gage collar pressures actually become positive from stations 13 to 16. Such positive gage pressures indicating jet attachment (sometimes referred as reattachment) to the collar were first described by Bourque & Newman (1960) in their study of jet reattachment to adjacent plates. The gage collar pressure returns to near zero at station 17 as the jet presumably flows along the collar in its attached state. This process of attachment, or reattachment, is discussed in detail by Olson (1962).

Referring back to Fig. 23a, the data there do not show a region where the jet directly impacted the collar during attachment. A reasonable explanation is that the suction levels in Fig. 23a were not high enough to move the jet attachment point upstream. Yet, the  $-\Delta P_{exit}$  values are twice that in Fig. 23b. This apparent discrepancy stems from the fact that the data represent collars of different geometric configurations. So while the general behavior of the vectoring jet was similar in most of the cases studied, the different geometries had a large impact on the vectoring jet's quantitative performance. The effect of geometry is examined in the next section.

## 5.2 RESPONSE TO GEOMETRICAL CHANGES IN COLLAR

As mentioned previously, the geometrical configuration of the nozzle-collar assembly has a large impact on the fluidic performance of a counterflowing vectoring jet. However, the collar geometry is a major concern for practical applications of the counterflow vectoring concept. Minimizing external drag on the nozzle housing demands that any practical thrust vector concept be aerodynamically streamlined. The potential effects of collar aerodynamic cross section were considered by examining the thrust vector performance as a function of gap height  $G$ , divergence half angle  $\alpha$ , and length  $L$  (see Fig. 7). Lastly, overall geometry impact on critical vector angle  $\delta_{v,cr}$  was assessed. Since bistable operation is clearly undesirable for any flight worthy vectoring concept, the configurations were then evaluated on their ability to maximize critical vector angle.

### 5.2.1        Effect of Gap

The counterflow collars were designed to accommodate variations in gap height over a range from 2 mm (0.2H) to over 10 mm (1H). This was done by translating both the active (suction side) and inactive collars in the vertical plane without variation in the collar contour or length. The flexible Teflon suction cavity wall (refer to Section 3.1 for complete description on collar construction) would deform and translate with the vertical movement of the rigid collar, ensuring a smooth collar wall surface for all gaps heights. Care was taken during these experiments to position the collars symmetrically about the jet axis and seal them to the side plates to eliminate leakage.

Figure 24 shows the thrust vector angle  $\delta_v$  as a function of mass flow ratio for the collar having  $L/H = 2.0$  and  $\alpha = 60^\circ$ ; four different gap heights ranging from  $G/H = 0.25$  to  $0.60$  were studied. The curves show only the unattached smooth and continuous vectoring data. The attached flow portions of the hysteresis loops were omitted here for clarity of presentation. If shown, the hysteresis loops would have extended in the direction of the arrows to a vector angle of about  $50^\circ$  and returned to the critical vector angle value marked with the solid symbol. No arrows are shown of the two largest gap curves ( $G/H = 0.5$  and  $0.6$ ) since the suction pump was not powerful enough to make the jet attach by itself in these cases. However, jet attachment was induced by physically deflecting it to the collar wall at these larger gap heights and then allowed to detach on its own. In this way, the critical vector angles for these gaps could be determined.

The obvious feature of these curves is that for increasing gap height, more reverse mass flow is required to achieve a given vector angle. In fact, the increase in the amount of reverse mass flow required varies somewhat proportionally to gap height. This scaling suggests that the thrust vector angle may be more dependent on velocity ratio,  $-U_2/U_1$  and that, as a parameter, the mass flow ratio enters into this problem only through the gap height  $G/H$ . The importance of velocity ratio for counterflow vectoring could be significant because of the role it has played in previous counterflow studies (such as Strykowski & Wilcox, 1993). As mentioned in Chapter 2, these studies have shown that velocity ratio is an important parameter in countercurrent mixing layer dynamics. However, while interesting, this topic is best left to later in this report (see Section 5.4, Figs. 33 and 34) for more complete discussion.

Returning to Fig. 24, the critical vector angle values (marked by the solid symbols) are seen to be relatively insensitive to gap heights over the range studied here. This observation may seem counter intuitive since more effort should be required to make the jet attach to the collar if the jet were offset farther from the collar. Indeed, the jet at  $G/H = 0.40$  was able to vector to a greater angle ( $\approx 18^\circ$ ) before self attachment than the jet at  $G/H = 0.25$  ( $\approx 9^\circ$ ). (Note that for the  $G/H = 0.5$  and  $0.6$  cases that the jet was unable to attach by itself due to suction pump power limitations.) However, the jets in both cases returned to approximately the same angle after detaching from the collar. The reason for this behavior may be linked to the fact that once the jet detached from the collar, the reverse mass flows were relatively low for each gap. The relatively low mass flow ratio places the operation point of the

counterflowing jet on the flat portion of the mass flow ratio thrust vector response curve (Fig. 24). Since, vector angle was not very sensitive to mass flow ratio here, the resulting critical vector angle did not change much over the gap heights examined.

The effect of gap height is examined again for the same data in Fig. 25. Here the thrust vector response curve is plotted as a function of  $-\Delta P_{exit}$ . The data essentially collapse on a single linear curve without any discernible dependence on gap height. Additionally, since the previous plot showed that  $\delta_{v,cr}$  was invariant with the range of gaps studied, the critical vector angle values in Fig. 25 cluster within a small area.

### 5.2.2 Effect of Divergence Half Angle

While the gap height could be varied continuously, only discrete values of collar length and divergence half angle could be studied through the manufacture of individual collars. Only one collar ( $L/H = 2, \alpha = 60^\circ$ ) had a different divergence half angle than the others ( $\alpha = 30^\circ$ ). Therefore, the effect of  $\alpha$  on counterflow vectoring performance could not be examined in great detail. However, comparison of the thrust vector response curves for the two  $L/H = 2$  collars at  $\alpha = 60^\circ$  and  $30^\circ$  did illustrate the role divergence angle plays in the vectored jet behavior.

Figure 26 plots thrust vector angle as a function of gage exit pressure for the two divergence half angles at  $L/H = 2$  and  $G/H = 0.4$ . Both the unattached and attached data are shown for both cases. As with the other plots of this type, both collars show a nearly linear relationship between  $\delta_v$  and  $-\Delta P_{exit}$ . However, a few differences are apparent between the two data sets. The

attached data for the  $\alpha = 60^\circ$  collar show vector angles much greater ( $\delta_v$  nearly  $50^\circ$ ) than that of the  $30^\circ$  half angle collar ( $\delta_v \approx 30^\circ$ ). Additionally, the unattached data for the  $\alpha = 60^\circ$  collar reach a vector angle of nearly  $20^\circ$  before jet attachment to the collar. In comparison, the  $\alpha = 30^\circ$  collar data achieve only  $14^\circ$  of vectoring before attachment.

The attached vector angles are greater for the larger divergence angle presumably because the jet is simply following the contour of the collar wall to a greater vector angle. As for the second difference, the unattached data reach greater vector angles for the  $\alpha = 60^\circ$  collar likely for the same reason as for the greater gap heights. Since the surface of the  $60^\circ$  half angle collar has a smaller radius,  $R/H = 2.3$ , than the  $30^\circ$  collar,  $R/H = 4.0$  (see Eq. (4)), it curves farther away from the jet providing greater separation from the jet at a given distance downstream. Thus, the jet can be vectored to higher angles before attachment to the collar. The smaller radius of curvature for the  $60^\circ$  collar may also be responsible for its slightly greater critical vector angle. However, the difference in  $\delta_{v,cr}$  between the collars is not large enough to make generalizations on its dependence on divergence half angle.

### 5.2.3 Effect of Length

The collars were manufactured in three different lengths,  $L/H = 1.0, 2.0$ , and  $3.5$ . Each had a divergence half angle of  $30^\circ$ . As explained here and in the following section, collar length had an extremely important influence in counterflow vectoring performance.

Figure 27 displays the thrust vector angle as a function of gage exit pressure for the different collar lengths at  $\alpha = 30^\circ$ . Only smooth and

continuous data are shown. The data for each length represent results obtained for all gap heights studied for each length ranging from  $G/H = 0.2$  to  $1.0$  (please refer to Table 1 in Section 3.1 for a complete listing of gap heights). The data collapse to a family of nearly linear curves representative of each collar length. As with Fig. 25 for the  $\alpha = 60^\circ$  collar, gap height has no measurable effect on the vector angle to gage exit pressure relation for a given collar length. (Note that although the gap parameter  $G/H$  does not affect the  $\delta_v$  vs.  $-\Delta P_{exit}$  performance, it plays a significant role in determining the secondary to primary mass flow ratio as shown earlier in Fig. 24.) The most significant feature of this plot is that, for a given level of suction (level of  $-\Delta P_{exit}$ ), larger vector angles are achievable with the longer collars. The reason for this relation is clear. Increasing collar length increases the area on which the gage collar pressure distribution  $-\Delta P_c$  can act. Since the level of  $-\Delta P_{exit}$  is indicative of the overall gage collar pressure distribution (see Fig. 20), the resultant normal collar force  $F_{cy}$  is proportionally greater for a longer collar at a fixed  $-\Delta P_{exit}$ . The increase in normal collar force results in larger vector angles (from Eq. (6), note that  $\Sigma F_y = F_{cy}$ , see Appendix A). Conversely, a longer collar requires less suction to vector the jet to a given angle.

Another feature of significance in Fig. 27 is the value of critical vector angle, again highlighted by the solid symbols, for each collar length and gap height. The clumping of critical vector angle values in the  $3.5H$  and  $2H$  collars indicates that, like the  $60^\circ$  collar,  $\delta_{v,cr}$  is not very sensitive to gap height for these collars. Critical vector angle points for the  $1H$  collar are not shown on Fig. 28 for the following reason. *The jet could not be made to attach to this collar at any gap height even if physically deflected.* As a result,

no hysteresis loops were observed, making its critical vector angle difficult to define. The maximum angles shown in Fig. 28 at the larger gaps ( $G/H = 0.4$  and  $0.25$ ) were limited by the power of the vacuum pump. The maximum vector angle for the narrowest gap ( $G/H = 0.2$ ) seemed to be pump limited as well. However, the maximum vector angle achieved for this gap height seemed to put the jet against the collar surface ( $\delta_v = 22^\circ$  for the  $\alpha = 30^\circ$  collar). Because of the physical limits imposed by the collar surface, further increases in  $\delta_v$  would not be likely even if higher levels of  $-\Delta P_{exit}$  were possible. While not defined by a hysteresis loop, the maximum vector angle at  $G/H = 0.2$  could therefore be considered the "critical" vector angle for this collar.

Returning to the other lengths, a slight increase in maximum  $\delta_{v,cr}$  from  $3^\circ$  to  $4^\circ$  is indicated as collar length decreases from  $3.5H$  to  $2H$ . However, the inability to obtain the attached jet condition for the collar having  $L/H = 1$ , suggests that  $\delta_{v,cr}$  is a strong function of  $L/H$  in the range of  $L/H < 2$ . Large values for  $\delta_{v,cr}$  are extremely desirable for an aircraft vectoring concept in that it would maximize the range of useful stable vectoring. While the  $1H$  collar may require more suction and, consequently, more power to vector to a given angle, its high value of critical vector angle gives it a distinct advantage over the other two collar lengths.

#### 5.2.4      Geometry Impact on Critical Vector Angle

Collar length was demonstrated as having a direct impact on determining vector angle since  $F_{cy}$  was seen to be proportional to collar surface area. Critical vector angle also varied with collar length, with an

extreme change occurring for  $L/H < 2$ . Maximum achievable critical vector for each collar length angle is plotted as a function of collar length in Fig. 28 with this large difference in critical vector angles well illustrated. To obtain this plot, the critical vector angle for the  $L/H = 1$  case was taken as the highest  $\delta_v$  achieved for this length as mentioned in the previous section. Data for the  $\alpha = 60^\circ$  collar are shown as well, for completeness. Increasing the divergence half angle by  $30^\circ$  seems to increase  $\delta_{v,cr}$  slightly. (As mentioned in Section 5.2.2, this increase may be a result of the decreased collar radius, but the actual mechanism is not entirely clear.)

The most important aspect presented here, however, is again the large critical vector angle at  $L/H = 1.0$  at  $G/H = 0.2$ . The large value results from the fact that the  $L/H = 1$  collar gave no evidence of bistable jet attachment. Even though the jet was observed to be vectored against the collar surface at the highest suction levels ( $\delta_v = 22^\circ$  for the  $\alpha = 30^\circ$  collar), the jet never stably attached. Suction could be reduced, and the vector angle would drop accordingly. The fact that large continuous vector angles are achievable for a relatively small collar length and gap height has important practical implications. Namely, airframe designs incorporating counterflow vectoring will need to minimize both  $L/H$  and  $G/H$  in order to minimize external drag. Furthermore, this lack of hysteresis suggests that there may be a critical vector length, between  $L/H = 1$  and  $2$ , below which counterflow vectoring can operate without any bistability. However, the presence or absence of bistability, as shown in the next section, is also dependent on exit Mach number.

### 5.3 EFFECT OF PRIMARY EXIT MACH NUMBER

With the effects of collar geometry examined, the role that primary flow conditions play in counterflow thrust vectoring becomes the current topic of discussion. Variation in  $M_e$  was of particular interest because under realistic flight conditions the engine exhaust would be throttled over a wide range of flow conditions. Collar geometry was fixed using the  $L/H = 1$ ,  $\alpha = 30^\circ$  collar at  $G/H = 0.2$  since this configuration provided stable vectoring to large vector angles. The exit Mach number was then varied by throttling the primary flow rate using the bypass valve located at the entrance of the free jet facility (see Section 3.2). Exit Mach numbers of 0.316, 0.387, 0.447 and 0.500 were chosen for study since they defined equal increments of  $M_e^2$  and thus exit momentum (see Eq. 8 below).

Figure 29 plots the vector angle response curve for the different exit Mach numbers as a function of gage exit pressure. As expected, the curves for all the Mach numbers studied are nearly linear. The curves become progressively steeper as  $M_e$  is reduced, indicating that less suction is required to vector the jet to a given angle. This plot resembles Fig. 27 where, for a given level of gage exit pressure, larger values of  $\delta_v$  were achievable for longer collars. As described in Section 5.2.3, the longer collars produced a greater normal collar force,  $F_{cy}$ , on the jet for a given level of suction, thus vectoring it to a greater angle. Reducing  $M_e$  has the same effect on  $\delta_v$ . The primary jet momentum,  $(\dot{m}U)_1$ , can be written as:

$$(\dot{m}U)_1 = \gamma M_e^2 P_e A_e \quad (8)$$

where  $P_e$  is assumed to be atmospheric pressure,  $\gamma$  is the ratio of specific heats in the primary flow, and  $A_e = H*W$ . At a given  $-\Delta P_{exit}$  level, a reduction in  $M_e$  at a fixed  $L/H$  then increases the ratio of collar force to primary momentum,  $F_{cy}/(\dot{m}U)_1$  (as would an increase in  $L/H$  at a fixed  $M_e$ ). Increasing this ratio results in a larger vector angle (from Eq. (6), note that  $\Sigma F_y = F_{cy}$  and  $(\dot{m}U)_x = (\dot{m}U)_1 + (\dot{m}U)_2$ , see Appendix A).

Figure 30 shows the same data with the vector angle plotted as a function of mass flow ratio. The data collapse onto a single curve without any dependence on exit Mach number for the limited range of exit Mach numbers studied. Since the data presented in Fig. 30 is taken at a fixed gap height, the relationship between  $\dot{m}_2/\dot{m}_1$  and  $\delta_v$  is qualitatively in agreement with the data presented earlier in Fig. 24 where the amount of secondary mass flow required to vector the jet to a given angle was roughly proportional to  $G/H$ .

As mentioned before, thrust vectoring with the  $L/H = 1$  collar at  $M_e = 0.5$  ( $M_e^2 = 0.25$ ) was continuously controllable from the centerline to the maximum angle achievable. Continuous control was also possible at  $M_e = 0.447$  ( $M_e^2 = 0.2$ ). However, when the exit Mach number was reduced below 0.4, the vectoring jet began to exhibit bistable behavior. The hysteresis loops become clear when the data for the lowest two Mach numbers studied are plotted alone in Fig. 31. The figure shows the large jump in vector angle and the reduced reverse mass flow typical of the attached behavior seen at the longer collars at  $M_e = 0.5$ . Comparing the attached data points for the  $M_e = 0.316$  ( $M_e^2 = 0.1$ ) and  $0.387$  ( $M_e^2 = 0.15$ ) cases, shown in both Figs. 31 and 30, to the highest vector angles for the larger Mach numbers in Fig. 30, reveals

that the  $\delta_v$  values and mass flow ratios are nearly identical for all cases. This clustering of the data indicates that at high levels of suction, the jets at the larger exit Mach numbers studied here ( $M_e = 0.447$  and  $0.5$ ) have virtually "attached" themselves to the collar and achieved the greatest vector angles allowed by the collar divergence half angle. The data would also confirm the observation made in the previous section that the vectored jet at  $M_e = 0.5$  for the short collar seemed to be hard against the collar surface at maximum suction. Despite this apparent "attached" state, continuous control of the  $M_e = 0.447$  and  $0.5$  jets was possible throughout their entire range of vectoring.

The hysteresis loops in the thrust vector response curves for the lower Mach numbers shown in Fig. 31 resulted from the lower exit momentum of these jets. The entrainment of the jet evidently had more of an effect on these cases so that the jet was more likely to attach to the collar. As a result, the critical vector angles, as defined by the return of the jet from the collar to near the centerline, were considerably less than the " $\delta_{v,cr}$ " values (maximum angles obtainable) for the cases without hysteresis. Figure 31 shows that the  $M_e = 0.387$  case has a critical vector angle of approximately  $11^\circ$ . While this particular case does not display a discernible hysteresis loop, bistable behavior is evident when  $\delta_v$  reaches this point and then becomes attached to the collar. Upon attachment, reduction in suction brings the jet immediately back to the  $11^\circ$  angle. Thus this vector angle was considered to be the critical value. The  $M_e = 0.316$  case shows a typical hysteresis loop with the attached jet demanding that the suction be reduced before it detaches to give a  $\delta_{v,cr}$  value of approximately  $6^\circ$ . The comparison of the bistable behavior of these two

cases reveals an interesting evolution of the hysteresis loop as  $M_e$  is reduced for the  $L/H = 1$  collar. At  $M_e$  above approximately 0.4 there is no bistable behavior in the jet. At  $M_e \approx 0.39$ , the bistable behavior is defined by only two points on the mass flow ratio thrust vector response curve. As  $M_e$  is further reduced, the bistable behavior is defined by four points, giving a hysteresis loop similar to those of the longer collars.

This data shows that as  $M_e$  (and  $U_1$ ) is increased, the jet will be less likely to attach to the collar for a given level of suction. This observation is counter to what Wilson (1970) stated in his thesis on curved wall jets. Wilson suggested that a high speed jet (with a high rate of entrainment) is more likely to become attached to an adjacent surface than a low speed jet. Indeed, the curved jet study of McGlaughlin & Greber (1967) showed that increasing the velocity of an initially laminar jet provided larger regions of attachment to an adjacent curved surface presumably because of the jet's increasing natural entrainment. However, their study also revealed that once the jet Reynolds number exceeded a critical value on the order of 15,000 (the exact number depended on nozzle aspect ratio), further increases in velocity had no effect on jet attachment. Since the jet Reynolds numbers for all of the Mach numbers studied considerably exceed this critical value, Wilson's statement does not likely apply to the jet described in this report.

As an aside, the observation was made that when acquiring data for the  $M_e = 0.387$  and 0.316 cases, the suction could be set to a certain level ( $-\Delta P_{exit} \approx 40$  and 30 torr at  $M_e = 0.387$  and 0.316) so that the jet would oscillate between the near centerline position and the collar surface. This behavior was similar to that described by Viets (1975) in the study of "flip flop" jets.

Since the oscillation behavior was observed in only these two cases, generalizations on its occurrence were difficult. However, the fact that both the jet momentum and normal collar force were relatively low for these cases might suggest that the "boundary" between stable continuous and stable attached operation was not well defined. Structures within the jet shear layer at the above levels of suction may have been able to entrain enough air in order initiate attachment to the collar. However, the ensuing "attachment" to the short collar presumably did not provide a curved flow with the cross stream pressure gradient necessary (and thus a high enough  $F_{cy}$ ) to maintain stability. Hence, the jet detached and the process repeated. In any case, such points were clearly dynamic in nature and would not be considered desirable operating points for any kind of vectoring system, their averaged behavior was not shown in this study.

Critical vector angle is plotted as a function of  $M_e^2$  in Fig. 32 for the  $L/H = 1$  collar at  $G/H = 0.2$ . Along with the  $\delta_{v,cr}$  values determined from the above  $M_e$  cases, the  $\delta_{v,cr}$  value determined from a limited data set at  $M_e = 0.224$  ( $M_e^2 = 0.05$ ) is included for completeness. The critical vector angles for the lower three  $M_e^2$  values display a positive and approximately linear relationship. The  $\delta_{v,cr}$  values for  $M_e^2 = 0.2$  and  $0.25$  break this linear trend, suggesting that the curve departs rapidly from linearity for  $M_e^2 > 0.15$  where the  $\delta_{v,cr}$  values were determined by the maximum  $\delta_v$  achievable for the collar geometry. The critical vector angles for these exit Mach numbers are significantly greater than the  $\delta_{v,cr}$  values for the lower  $M_e$  cases. This behavior is similar to the critical vector angle value trends described in Fig. 28 where  $\delta_{v,cr}$  was plotted as a function of collar length. The data in Fig. 28

suggested that at a fixed  $M_e$  there is a critical length below which continuous counterflow vector control could be attained over the entire vectoring range allowed by the collar geometry. Likewise, the data in Fig. 32 suggest that at a fixed  $L/H$  there is critical value of  $M_e^2$  above which the primary jet momentum is great enough to allow the same continuous control.

#### 5.4 DIMENSIONAL ANALYSIS

Earlier in this report, velocity ratio was proposed as being an important parameter in counterflow vectoring based on data from the gap height studies. This section examines this supposition with further analysis of the data obtained in both the variable gap and exit Mach studies. All the important parameters are then summarized using dimensional reasoning. With the knowledge of what affects the performance of counterflow vectoring, arguments are made about the underlying physical mechanisms.

The data in Fig. 30 showed that for a given collar configuration, the  $\delta_v$  versus mass flow ratio curves were invariant with primary Mach number. Since density and temperature were roughly the same between the primary and reverse flow streams, the curves in Fig. 30 are easily plotted as a function of velocity ratio,  $-U_2/U_1$ . (Here,  $-U_2/U_1$  is defined as the mean velocity ratio at the nozzle exit plane and is determined by dividing the mass flow ratio in Fig. 30 by  $G/H$ .) This plot is shown in Fig. 33. Since  $G/H$  was constant ( $G/H = 0.2$ ), the curves in Fig. 33 look the same as in Fig. 30. However, Fig. 33 provides an indication of the amount of reverse velocity required to vector the jet. The curves show that the vector angle increases significantly at a velocity ratio of approximately 0.33. Additionally, Fig. 33 provides a basis for

the argument that velocity ratio is important in determining the performance of the counterflow vectoring jet.

Recall from Section 5.2.1 that the amount of reverse mass flow required to vector the jet to a given angle seemed to vary proportionally with gap height as shown by Fig. 24. This behavior was consistent with the speculation that vector angle could be dependent on velocity ratio. The data from Fig. 24 is replotted as a function of velocity ratio in Fig. 34 by dividing each of the curves by their respective normalized gap heights in the same way that the data in Fig. 33 were derived. Unlike Fig. 33, Fig. 34 holds primary velocity essentially constant and varies gap area. The data in Fig. 34 reveal that vector angle is much less dependent on gap height when plotted versus velocity ratio than when it was plotted versus mass flow ratio in Fig. 24. Moreover, the curves in Fig. 34 compare well with those in Fig. 33, with vector angle showing significant change at  $-U_2/U_1 \approx 0.33$  in both plots. Thus Fig. 34 would indicate, as Fig. 33 did, that velocity ratio is an important parameter in counterflow vectoring performance.

While the curves of Fig. 34 do not match as well as the data did in Fig. 33, the discrepancies can be explained as follows. Since the reverse flow velocity  $u_2$  is a function of distance along the collar, i.e.  $u_2 = u_2(x)$  and collar geometry (see 4.2.1), the vectoring jet will undoubtedly be influenced by a velocity ratio distribution along the collar. Thus, reverse velocity as measured at the nozzle exit plane,  $U_2$ , for varying gap heights may not be the best parameter for determining vector angle and should not be expected to collapse the curves perfectly. Regardless, the relative collapse of the  $\delta_v$  vs.  $-U_2/U_1$  curves in Figs. 33 and 34 would certainly support the argument that

vector angle was dependent on the general velocity ratio  $-u_2/u_1$  rather than some other parameter such as mass flow ratio. Furthermore, for a given set of flow conditions and collar geometry, the gage exit pressure was shown to be nearly constant for a given vector angle (see Figs. 25 and 27) regardless of gap height. Bernoulli's equation would then suggest that the reverse flow velocities through the gap height would be constant as well. While perhaps a bit suspect in its application to the present flow situation with undoubtedly high pressure losses, the Bernoulli relation would lend further weight to the role of velocity ratio as an important parameter in counterflow vectoring. If the vector angle is dependent on velocity ratio, then the counterflow vectoring process can be assumed to be a shear layer interaction driven process much like the axisymmetric counterflow studies of Niccum (1990), Strykowski & Niccum (1991) and Strykowski & Wilcoxon (1993).

A complete dimensional analysis would then entail all the relevant variables describing the flow within the shear layer. The vector angle  $\delta_v$  must then depend on parameters describing both the primary and reverse (secondary) flows as well as the associated geometry, i.e.

$$\delta_v = f(L, G, \alpha, u_1, \rho_1, T_{01}, M_1, u_2, \rho_2, T_{02}, M_2) \quad (9)$$

where  $M_1 = M_e$  at the nozzle exit. This relation can be written in the non-dimensional form:

$$\delta_v = f(L/H, G/H, R/H, u_2/u_1, \rho_2/\rho_1, T_{02}/T_{01}, M_c) \quad (10)$$

where  $M_c$  (local convective Mach number) =  $(u_1 - u_2)/(a_1 + a_2)$  and  $a$  = speed of sound. Collar non-dimensional radius  $R/H$  includes the effect of  $\alpha$  through Eq. (4). Since the collars used in this study were arcs of constant radius for each configuration, the collar radius and length are sufficient to describe its geometric configuration. However, collars of more complex curvature would doubtless require more involved geometric parameters.

Relation (10) can be examined for the parameters that have affected the performance of counterflow vectoring in this study. The density and total temperature ratios were nearly unity and invariant throughout this study, so these effects could not be isolated. Strykowski, Krothapalli, & Wishart (1992) showed that total temperature ratio can influence the entrainment characteristics of counterflowing jets. Density ratio has also been shown to be a significant factor in shear layer mixing in the axisymmetric counterflowing studies of Strykowski & Niccum (1992). Therefore, either of these parameters could affect the counterflow jet thrust vector angles. However, the overall effects of both  $T_{02}/T_{01}$  and  $\rho_2/\rho_1$  are still unclear and are considered constant in this analysis. Convective Mach number was approximately 0.3 or less throughout the entire flow field for all of the flow conditions tested. The findings of Papamoschou & Roshko (1988) indicated that for convective Mach numbers of this order, compressibility will not significantly affect the shear layer mixing dynamics. Therefore,  $M_c$  can be eliminated as an important parameter for this study. Over the range of gap heights studied,  $G/H$  was shown not to influence continuous vector angle to any measurable extent, so  $G/H$  can be dropped as well. (Note, however, that  $\dot{m}_2/\dot{m}_1$  would be dependant on  $G/H$ .) The relevant parameters affecting counterflow vectoring

in the studied subsonic jet are therefore a function of collar length, collar radius, and velocity ratio. Inclusion of the collar radius expression, which would include the effect of divergence half angle, must be considered conditional at this time, however, pending further studies of collars of various  $\alpha$  (various radii at fixed length). This relation is expressed by:

$$\delta_v = f(L/H, R/H, u_2/u_1) \quad (11)$$

which is consistent with the findings of this study.

These parameters give an indication of the physical mechanisms are responsible for counterflow thrust vectoring in the present problem. The Coanda effect does provide for the movement of the jet towards the collar. As discussed in Chapter 2 and shown in Figs. 2b - 3b, the jet entrains fluid from the surroundings and will attempt to entrain, in this case, air between the collar and the jet. However, the presence of the collar requires that the entrained air be replaced by air which flows along the collar from downstream. In order for flow to enter this constricted region, the pressure there must be less than the pressure of the surroundings. Adopting the cylindrical coordinates shown in Fig. 3b, a cross stream pressure gradient,  $\partial P/\partial r$ , is therefore established along the jet over the length of the collar ( $\partial P/\partial r = \partial P/\partial r(\theta)$ ) causing it to deflect towards the collar and in some cases to attach to it. However, the described Coanda effect is strictly passive, only a fixed distribution of  $\partial P/\partial r$  will be developed for a fixed geometry and flow condition. The behavior of the continuous vectoring jet suggests that the responsible mechanism could be controlled by active means.

Since velocity ratio was determined to be an important parameter in this study, the countercurrent mixing layer is most likely responsible for active control of the vectoring jet. Counterflow, in conjunction with collars, has been shown to be an effective means of enhancing the mixing of free jets with turbulent shear layers in both the incompressible (Strykowski & Wilcoxon, 1993) and compressible (Strykowski, Krothapalli, & Wishart, 1992) flow regimes. These studies showed that a countercurrent mixing layer allowed the formation of large three-dimensional structures within the layer. These structures enhanced the entrainment of the shear layer which led to elevated growth rates as velocity ratio  $-U_2/U_1$  was increased. When counterflow is applied to one shear layer of the rectangular jet in this study, the resulting structures will augment the entrainment of mass. This process will be inhibited by the presence of the collar, thereby increasing the average  $\partial P/\partial r$  along the length of the collar and drawing the jet off-axis. Unlike the passive Coanda effect described above, however, the amount of entrainment and thus the average  $\partial P/\partial r$  can be controlled by adjusting the velocity ratio and thus controlling vector angle.

Evidence of enhanced mixing with the application of counterflow to the jet is seen in Fig. 35. The figure plots cross stream Mach profiles taken at a fixed distance downstream of the collar ( $L/H = 1$ ,  $G/H = 0.2$ ) for different levels of counterflow. For each level of suction (level of  $-\Delta P_{exit}$ ) the probe was carefully aligned with the vector angle of the flow. As the suction level is increased from zero, the jet profile spreads out indicating increasing entrainment and mixing with the greater levels of counterflow. The spreading reaches a maximum at a gage exit pressure of approximately -76

torr. The spreading then decreases as suction is further increased. This reversal in suction to spreading rate trend occurs as the jet nears the collar wall. Because of the proximity of the jet to the collar wall, the size of the shear layer structures is restricted and thus the spreading rate of the jet reduced. By this point, the jet is nearly attached to the collar (although for the  $L/H = 1$  collar, continuous control of the jet remains), so it is conceivable that the mixing layer between the primary and reverse flows has made the transition between a free shear counterflowing layer to a wall bounded counterflowing layer. The dynamics of the mixing layer would then undoubtedly change. This change in mixing dynamics is examined in more detail later in this section. Regardless, Fig. 35 provides evidence that, for the majority of the vectoring range, jet mixing is dependent on counterflow providing an active means of controlling entrainment and thereby the vector angle.

Continuous control of the jet can be maintained without jet attachment for the reason expressed by Strykowski & Krothapalli (1993) in their initial research into counterflow vectoring. They reasoned that the vectoring of the jet will reduce the cross-sectional area of the counterflowing channel (the area between the vectoring jet and the collar wall), thus increasing the pressure drop in the secondary (reverse) stream. Consequently, the amount of counterflow will be reduced and with it the generation of the mixing structures. An equilibrium position will be achieved where sufficient suction is present to excite the layer and cause vectoring, but not too large a vector angle such that counterflow vectoring is cut off. Sometimes, as shown by the attached condition of the jet in this study, there was enough vacuum

pressure to hold the jet against the collar in the absence of counterflow. When these conditions were present, control of  $\partial P/\partial r$  was lost, allowing the jet to suddenly attach itself to the collar in a bistable configuration. However, as described earlier, given a short enough collar or a large enough primary jet momentum, continuous control of the vectoring jet could be maintained to angles over  $20^\circ$ .

Before continuing, a note is made on how counterflow enhances mixing in the counterflow vectoring jet. Strykowski & Wilcoxon (1993) in their axisymmetric counterflow studies, determined that once a critical level of counterflow was reached,  $(-U_2/U_1)_{cr} \approx 0.2$ , the development of global oscillations led to significant increases in jet mixing (see Chapter 2). Indeed, Strykowski & Krothapalli (1993) suggested that self-excitement of the shear layer may have been the responsible mechanism for their counterflow vectoring studies. However, such self-excited instabilities were not readily apparent in the counterflow vectoring jet of this study. The counterflow may have simply reduced the convective velocity of the shear layer, allowing time for structures to grow within the layer and thus enhance mixing. More recent measurements by Strykowski, Krothapalli, & Jendoubi (1995) in compressible shear layers support this later view. However, a more complete study including non-intrusive velocity measurements and spectral analysis of the turbulence fields will be needed in order to determine the complete role, if any, that global instabilities play in counterflow vectoring.

As mentioned above, Fig. 35 revealed that the jet spreading reduced as the jet neared the collar. This effect was attributed to the transition of the free shear layer to a wall bounded mixing layer preventing the development of

large scale structures and thus reducing mixing. This observation begs the question of how continuous vectoring can be maintained (pertaining to the  $L/H = 1$  collar) without the continuous production of mixing. The answer lies in the change in mixing dynamics during the transition of the mixing layer.

Figure 36 shows the countercurrent mixing layer transitioning from a free to a wall bounded shear flow. As the mixing layer moves close to the curved surface of the collar, the layer itself becomes curved. At this point the effect of the centrifugal force field on the turbulence in the layer becomes important. Rayleigh's criterion predicts that for a laminar and inviscid curved flow, the radial equilibrium of a fluid element is stable if the radial gradient of angular momentum is positive (proportional to  $\partial(ru_\theta)^2/\partial r > 0$ ) and unstable if the radial gradient of the angular momentum is negative (proportional to  $\partial(ru_\theta)^2/\partial r < 0$ ). Eskinazi & Yeh (1956) first showed that Rayleigh's criterion applied to curved turbulent flows. In regions where the gradient of the angular momentum distribution was positive, turbulence was suppressed, and where the gradient of the angular momentum was negative, turbulence was promoted. Referring to Fig. 36, the curved countercurrent mixing layer is seen to have a band of unstable flow where  $\partial(ru_\theta)^2/\partial r < 0$  sandwiched between two regions of stable flow where  $\partial(ru_\theta)^2/\partial r > 0$ . Considering the findings of Eskinazi & Yeh, this unstable region would produce higher levels of turbulence than would normally be found in a plane mixing layer. Furthermore, Margolis & Lumley (1965) demonstrated that turbulent energy transport by the turbulent velocities is highly promoted in unstable curved mixing layers. According to Margolis & Lumley, this

promotion of transport in the unstable layer causes the turbulence intensities to persist at a high level through the development of the curved flow. Such high levels of turbulence and turbulent energy transport in the curved countercurrent mixing layer would produce high levels of entrainment along the collar thus providing a mechanism for vectoring in the absence of large structures. Once downstream of the collar, the mixing layer would transition back to a plane free shear layer with turbulence no longer being generated due to curvature. Hence, the mean cross stream Mach profiles taken 16H downstream of the collar in Fig. 35 show decreased spreading at high levels of suction even though large amounts of mixing occurred at the collar surface resulting in the continuous vectoring of the jet.

Now that the significant parameters and mechanisms responsible for continuous vectoring have been examined in detail, the parameters affecting the level of critical vector angle are discussed. As mentioned in Section 5.1, critical vector angle seemed to depend on the attached jet condition since  $\delta_{v,cr}$  was the angle the jet settled at once it became detached from the collar with minimal disturbance. When the jet is attached to the collar, there is no significant counterflow past the jet. Therefore, unlike general vectoring, the critical vector angle value does not depend on shear layer interaction but rather on the passive Coanda effect keeping the jet attached. The jet detaches as the point of jet impingement moves past the end of the collar when suction is reduced. Thus, the jet is more easily held by a longer collar or for a lower primary jet momentum which describes the behavior of the jet in this study.

This study also showed that the attached condition is dependent on gap height and divergence half angle. Figures 25 and 26 illustrate that higher levels of suction ( $-\Delta P_{exit}$ ) are required to attach the jet to the collar for larger gaps and larger  $\alpha$ . In summary, the attached condition of the jet depends on the entire collar geometry as well as the primary jet momentum. Because of its relationship to the attached jet condition, critical vector angle might then be a function of:

$$\delta_{v,cr} = f(L/H, G/H, \alpha, (\rho U^2)_1) \quad (12)$$

These parameters agree with the ones used by Olson (1962) in predicting the reattachment of a two-dimensional jet to an adjacent plate. Olson derives several expressions for numerically predicting the point of jet attachment and the bubble pressure of the attached jet. These expressions are important in determining the attached behavior, however, they give no indication as to the condition of the jet after it detaches from the adjacent surface. Therefore, while  $G/H$  plays an important role in the attached jet, the dependence of the critical vector angle on gap for the cases examined in this study was shown to be weak and inconsistent (see Figs. 24 and 25). Similarly, divergence half angle fixes the vector angle achieved on attachment (Fig. 26) but its effect on critical vector angle is less pronounced (Fig. 28).

Collar length and primary jet momentum play the largest role in determining  $\delta_{v,cr}$  as can be seen in Figs. 28 and 32. Unfortunately, the precise relation between these parameters and the value of critical vector angle could not be determined. The difficulty arises because the relation between the state

of the jet just prior to detachment and the state of the jet after it detaches remains unknown. Further testing of different collar geometries and flow conditions will doubtless shed more light on this question. Regardless, decreasing collar length or increasing the jet momentum will increase the value of critical vector angle. Furthermore, the data collected for this study would indicate that there exists critical values for these parameters that once reached, allow the jet to vector continuously over a wide range of angles.

## 5.5 COLLAPSE OF DATA

The primary goal of this research was to examine how collar geometry and flow conditions affected the performance of a counterflow vectoring subsonic jet. These topics have been covered in some detail in the preceding sections of this chapter. Insights into the possible vectoring mechanisms have also been discussed. The next step is to develop a way to predict vectoring performance for a given collar design and set of flow conditions.

Section 5.4 revealed that velocity ratio was the primary flow parameter for determining the vector angle. Predicting vector angle from velocity ratio  $-u_2/u_1$  would then be a physically sound approach. However, the driving reverse flow velocity is a function of position along the collar ( $u_2 = u_2(x)$ ) and collar geometry and very difficult to measure accurately. Therefore, using it to predict vectoring performance would be difficult especially under realistic thrust vectoring applications. Vector angle might also be determined as a function of velocity ratio  $-U_2/U_1$  at the nozzle exit plane since this could be reasonably measured. However, as seen in Fig. 33, velocity ratio defined in this manner does not always give a unique vector angle nor is it very robust

over variable gap heights. Gage exit pressure is then the remaining variable for predicting vector angle.

While not linked to the counterflow vectoring mechanism, gage exit pressure  $-\Delta P_{exit}$  does provide an easily determined, robust and direct parameter for predicting vector angle as shown by the  $-\Delta P_{exit}$  thrust vector response curves of Fig. 27 and Fig. 29. By normalizing  $-\Delta P_{exit}$  by the primary jet momentum flux,  $(\rho U^2)_1$  or  $(\gamma P M^2)_e$ , the data from Figs. 27 and 29, which showed the effect of length and exit Mach number on vectoring performance, are now plotted together on Fig. 37. Figure 37 plots all data for every gap height and exit Mach number studied for the  $\alpha = 30^\circ$  collars. Since the gage exit pressure was normalized by the primary momentum flux, vector angle is now seen to be independent of exit Mach number. The linear thrust vector curves are determined by collar length, but all the data for each  $M_e$  plotted in the curves in Fig. 29 has now collapsed for the  $L/H = 1$  collar in Fig. 37.

The curves in Fig. 37 were dependent on collar length as was expected since vector angle was shown to be a function of  $L/H$ . In order to make these curves collapse regardless of collar length, the normalized gage exit pressures were multiplied by  $L/H$ . The result is shown in Fig. 38. This figure shows a complete collapse of the vector angle data for all of the  $\alpha = 30^\circ$  collars independent of flow conditions or collar length. This curve provides a very powerful design tool. The effects of collar length and primary flow velocity on vector angle can easily be determined for a given gage exit pressure from this nearly linear curve by using the empirical relation:

$$\delta_v = C * \frac{-\Delta P_{exit}}{(\rho U^2)_1} * \frac{L}{H} \quad (13a)$$

or by using Eq. (8):

$$\delta_v = C * \frac{-\Delta P_{exit}}{(\gamma M^2 P)_e} * \frac{L}{H} \quad (13b)$$

where  $C$  is the constant value of the slope determined from a linear regression of the experimental data. The approximate value for the slope of the line given by the data in Fig. 38 is:

$$C \approx 51^\circ \quad (14)$$

Since this study examined only one collar of a differing divergence half angle (differing radius with length held constant), the effect of  $\alpha$  on continuous counterflow vectoring is unclear. Therefore inclusion of a divergence half angle term in Eq. (13) was considered inappropriate at this time.

The thrust vector response curves in Fig. 38 collapse well using Eq. (13) for the following reasons. Equation (6) (Section 4.2.3) shows that vector angle is determined from the ratio of normal collar forces,  $\Sigma F_y$  over the net momentum of the counterflowing stream,  $\Sigma(\dot{m}U)_x$ , plus the axial pressure forces,  $\Sigma F_x$ . These terms require extensive instrumentation and data processing for evaluation. Equation (13) essentially condenses the relation given by Eq. (6) into the known or easily determined components: gage exit

pressure, collar length, and primary jet exit momentum. Given that the vector angles were calculated using (6), the fact that all the data collapse with (13) may not be surprising. However, Eq. (6) was independently verified as an accurate means of determining vector angle by downstream pitot surveys as shown in Fig. 21. As a result, Eq. (13) provides an extremely simplified means of determining vector angle and required suction for a given collar design and flow condition. Additionally, since the resultant normal suction force,  $\Sigma F_y$  in (6), of each collar can be represented by  $-\Delta P_{exit}$  multiplied by its length, the collapse of the data with (13) reveals that every collar pressure distribution can be uniquely specified by  $-\Delta P_{exit}$  regardless of collar geometry. For example, the collar pressure distributions of Fig. 20 would essentially collapse onto a single curve if normalized by  $-\Delta P_{exit}$ .

Equation (13) reveals that there is a maximum angle achievable for a given collar length and primary jet momentum. Providing that a perfect vacuum can be developed by a suction system (maximum  $-\Delta P_{exit} = P_{atm}$ ) and that the flow of the primary jet is perfectly expanded ( $P_e = P_{atm}$ ), then the maximum vector angle,  $\delta_{v, max}$ , is then:

$$\delta_{v, max} = \frac{C}{(\gamma M^2)_e} * \frac{L}{H} \quad (15)$$

Using Eq. (15) and its assumptions, the minimum collar length,  $(L/H)_{min}$ , required to vector to a given angle  $\delta_v$  can then be determined from:

$$\left(\frac{L}{H}\right)_{min} = \frac{\delta_v * (\gamma M^2)_e}{C} \quad (16)$$

Equations (15) and (16) provide limits to the designer of counterflow vectoring systems. The collar length is determined by the suction force necessary to vector the jet to the required angle. This consideration would be especially important for aircraft applications because of the high exhaust momentum generated by aircraft engines. However, the value of  $C$  might be increased by reshaping the collar so that it became more efficient in vectoring and thus allow shorter collar lengths to achieve a given vector angle.

While Eqs. (13 - 16) do provide a powerful design tool for predicting counterflow vectoring performance, they must be applied with caution. The vector angle would be limited by the value of the divergence half angle of the collar. For example, with an  $\alpha = 30^\circ$  collar,  $\delta_v$  could not exceed an approximate value of  $30^\circ$ . Additionally, the collapsed curve in Fig. 38 represents smooth and continuous vectoring data, however, much of the data represent regions of bistable jet operation. Thus, any vector angle calculated from these equations that was greater than the  $\delta_{v,cr}$  given for that collar geometry and primary flow conditions would represent an undesirable point of operation. Because of the somewhat limited data base given by this study, critical vector angle can not yet be predicted accurately for a given collar geometry and flow condition. However, Figs. 28 and 32 provide guidance to these limitations imposed by the critical vector angle.

As mentioned in earlier sections, there seems to be critical values for collar length and primary jet momentum that once reached, the jet is capable of continuous vectoring over a wide range of angles. Figures 28 and 32 show that once collar length is decreased to  $L/H = 1$  at  $M_e = 0.5$  or once  $M_e^2$  exceeds

0.2 ( $M_e$  exceeds 0.447) at  $L/H = 1$ ,  $\delta_{v,cr}$  jumps considerably. This behavior suggests that below a critical ratio of collar length over  $M_e^2$ , continuous vectoring is only limited by the divergence half angle of the collar. From the limited data given above, wide ranges of continuous vectoring would be possible for:

$$[L/(H*{M_e}^2)] \lesssim 5 \quad (17)$$

Equation (17) should be used with caution since it was derived from a limited data base (e.g. only for subsonic jets). Additionally, the limits on this continuous vectoring region may break down as  $G/H$  approaches zero. However, the results of this study do indicate that such a critical ratio of length to primary jet momentum exists and that it plays an important role in counterflow vectoring.

In summary, Eqs. (16) and (17) along with the data presented in Figs. 28 and 32 provide guidance on minimum and maximum values to both collar length and primary jet momentum for the designer of counterflow vectoring systems. Within these realistic limitations, the results of this study (for the  $L/H = 1$  collar) have shown that counterflow can be used successfully to vector a jet without bistability over a wide range of angles. Counterflow therefore provides a viable alternative to thrust vectoring by mechanical means.

## 6. CONCLUSIONS

A fluidic thrust vectoring scheme utilizing countercurrent mixing and suction collars has been shown to effectively vector a rectangular subsonic jet over  $20^\circ$  within a laboratory setting at Mach numbers up to 0.5. The effect of suction, nozzle-collar geometry, and primary flow conditions on the behavior of the vectoring jet have been documented. The main conclusions which can be drawn from this study are the following:

- Under some conditions, the vectoring jet can demonstrate bistable behavior where the jet is either controlled continuously or is attached to the suction collar at high vector angles. When attached, the jet remains so over a wide range of vacuum conditions forming a hysteresis loop when vector angle is plotted as a function of mass flow ratio. Critical vector angle is defined to be the maximum angle achievable outside of the bistable operating conditions. Most importantly, with certain combinations of collar geometry and flow conditions, the counterflowing vectoring jet does *not* demonstrate bistable behavior, providing continuous vectoring over a wide range of angles.
- Thrust vector angle  $\delta_v$  is dependent on collar length  $L/H$  and primary jet momentum flux  $(\rho U^2)_1$ . Performance based on secondary (reverse) to primary mass flow ratio  $\dot{m}_2/\dot{m}_1$  varies proportionally to the counterflow gap height  $G/H$  indicating that velocity ratio  $-u_2/u_1$  is an important fundamental parameter in determining vectoring performance.

- Continuous control of the thrust vector is dependent on two mechanisms: 1) When the jet is still relatively near the nozzle axis, the counterflow allows increased shear layer turbulence and therefore enhanced entrainment rates supporting moderate cross stream pressure gradients; and 2) as the jet moves close to the collar surface, centrifugal instabilities generate intense small scale turbulence which maintains strong cross stream pressure gradients very near the collar.

- Critical vector angle  $\delta_{v,cr}$  increases as collar length is decreased and as primary flow momentum is increased but the precise relation is still undetermined. Furthermore,  $\delta_{v,cr}$  appears to be insensitive to  $G/H$  over the range of gap heights studied. However, as mentioned above, mass flow ratio,  $\dot{m}_2/\dot{m}_1$ , does depend on the gap height parameter  $G/H$ .

- All data taken in the study for the  $\alpha = 30^\circ$  collars collapse onto a single nearly linear curve when vector angle is plotted as a function of gage exit pressure over primary momentum flux multiplied by  $L/H$ . This curve gives the empirical relation:

$$\delta_v = C * \frac{-\Delta P_{exit}}{(\rho U^2)_1} * \frac{L}{H} \quad (13a)$$

where  $C \approx 51^\circ$ . This relation provides a powerful tool for designing counterflow collars.

- Counterflow vectoring presents a potentially viable alternative to mechanically actuated thrust vectoring. Due to the absence of moving surfaces and the inherent cooling effects of the counterflowing stream, savings in weight and complexity might be realized for aircraft propulsion systems employing counterflow vectoring.

## FUTURE WORK

The behavior of the counterflow vectoring jet is highly sensitive to the suction collar geometry and depends highly on the shear layer interactions. Their effects should be quantified more thoroughly in order to attain a complete understanding of the phenomenon. The present study suggests the following actions:

- Non-intrusive measurements utilizing LDV or PIV of the mean and turbulent flow field within the collar should be made. This will determine the relevant counterflow velocity ratio as well as provide further insights into the vectoring mechanism. Downstream turbulence measurements would also be helpful in this regard. Such measurements would provide the needed basis for CFD modeling of this flow.

- Still more suction collar geometries of different lengths and divergence half angles should be examined at exit Mach numbers ranging from 0.5 and 2.0. The results of these studies could be compared against Eq. (13) (shown above) to determine its usefulness over a wide range of conditions. The effect of divergence half angle could then also be included in

Eq. (13). Ways of increasing the constant C could be explored by utilizing collars with complex curvature. Additionally, such studies would shed more light on ways to predict critical vector angle.

- If possible, future studies should employ a strain gage balance to determine normal and axial forces on the nozzle-collar assembly. This would make vector angle measurements more accurate by removing some of the assumptions made by the control volume method.
- Transient measurements of the rate of change of vector angle should be made for comparison with mechanical vectoring systems. Also, transient "oscillatory" behavior observed in a limited portion of the operating domain (see Section 5.3) must be examined.
- The effect of free stream turbulence on vector performance should be studied in order to determine the robustness of counterflow vectoring over a range of initial flow conditions.

This study has shown that counterflow vectoring is a very interesting and applicable problem. Indeed, the potential for counterflow to provide an innovative means of aircraft thrust vectoring exists. Counterflow vectoring is therefore both a rewarding and fertile ground for future study.

## APPENDIX

### A. DERIVATION OF CONTROL VOLUME EQUATIONS

Section 4.2.3 discussed the use of a control volume analysis to determine thrust vector angle  $\delta_v$ . Equation (6) gave a representation of  $\delta_v$  based on a momentum and force balance. Equation (7) provided a means of determining thrust vector efficiency (as given by the thrust coefficient,  $C_T$ ) based on information from the analysis. This appendix describes how Eqs. (6) and (7) were derived.

The control volume, shown in Fig. 19, is bounded by the collars and extends from the nozzle exit plane to past the collar ends. Various forces and momentum fluxes act on and pass through the surfaces of the control volume. For steady flow, the momentum equation in vector notation is:

$$\Sigma F = \int_S \rho u(u \cdot n) dA \quad (18)$$

where  $\Sigma F$  is the vector sum of all forces acting on the control volume surface  $S$ ,  $u$  is the local velocity vector, and  $n$  is the outward directed unit vector normal to a control surface element  $dA$ . Primary velocity  $U_1$ , reverse mass flow rate  $\dot{m}_2$ , and collar pressure distribution,  $P_c(x,y)$  are directly measured. However, before the above expression can be evaluated, some assumptions must be made on the pressure distributions along the other regions of the control volume surface.

Referring to Fig. 19, the suction gap height  $G$  is estimated to be at the constant pressure  $P_{exit}$ . Since the jet is subsonic, the pressure along the nozzle exit  $H$  is assumed to be atmospheric as is the pressure distribution

along the inactive gap. Sample measurements of the pressure distribution along the inactive collar showed that the gage pressures there were on the order of 0.5% that of the active (suction) collar. Hence, the pressure distribution there is considered to be atmospheric as well. Additionally, the downstream boundary of the control volume was located far enough such that the conditions there were atmospheric. In absence of a direct force balance, viscous drag on the nozzle collar assembly is neglected.

Since forces on the control volume surface are developed in relation to atmospheric pressure, the forces are zero on surface regions where the pressure is considered atmospheric. The summation of the forces acting on the control volume surface is then:

$$\Sigma \mathbf{F} = \mathbf{F}_c + \mathbf{F}_G \quad (19)$$

where  $\mathbf{F}_c$  is the resultant force vector acting on the suction collar and  $\mathbf{F}_G$  is the force acting on the suction gap.  $\mathbf{F}_c$  is defined as:

$$\mathbf{F}_c = \int_{A_c} (P_{atm} - P_c) \mathbf{n} \, dA \quad (20)$$

where  $A_c$  is the collar area and  $P_c = P_c(x, y)$ . The components of  $\mathbf{F}_c$  are then:

$$F_{cx} = \int -\Delta P_c \, dA_{cx} \quad \text{and} \quad F_{cy} = \int -\Delta P_c \, dA_{cy}$$

where  $-\Delta P_c = P_{atm} - P_c$  and  $dA_{cx}$  and  $dA_{cy}$  are the components normal to the x and y-axis of an incremental area on the collar surface.

The above integrations are evaluated numerically by assuming the pressure measured at each tap acts uniformly over an incremental area normal to  $\phi$  measured at the tap location. Where  $\phi$  is the angle between  $\mathbf{n}$  and the y-direction (i.e.  $\phi = 0^\circ$  at the nozzle exit plane). Thus:

$$F_{Cx} = \sum_{i=1}^m -\Delta P_{C,i} * \sin\phi_i \Delta A_c + \sum_{j=1}^n \left( -\Delta P_{C,m} - j * \frac{-\Delta P_{C,m}}{n} \right) \sin\phi_j \Delta A_c \quad (21)$$

and

$$F_{Cy} = -\Delta P_{C,0} * \left( \frac{\Delta A_c}{2} \right) + \sum_{i=1}^m -\Delta P_{C,i} * \cos\phi_i \Delta A_c + \sum_{j=1}^n \left( -\Delta P_{C,m} - j * \frac{-\Delta P_{C,m}}{n} \right) \cos\phi_j \Delta A_c \quad (22)$$

Here,  $i$  is the station or tap number and  $m$  is the station number for the tap farthest downstream on a given collar.  $-\Delta P_{C,i}$  is the locally measured collar static gage pressure and  $\Delta A_c$  is the incremental area on which  $-\Delta P_c$  acts.  $\Delta A_c$  is defined as:  $\Delta A_c = R * W * \Delta\phi$  where  $R$  is the collar radius,  $W$ , the collar width, and  $\Delta\phi$ , the fixed angular difference (in radians) between the evenly distributed collar taps. The boundaries of  $\Delta A_c$  are then located midway between each tap position. The first term of the  $F_{Cy}$  equation represents the gage exit pressure ( $-\Delta P_{C,0} = -\Delta P_{exit}$ ) acting on  $\Delta A_c/2$  since this pressure is a boundary condition (the term is not necessary in the  $F_{Cx}$  equation since the incremental area normal to the x-axis is zero at  $i = 0$ ).

The last summation term in each of the above equations represent an estimated collar pressure distribution from the last tap to the end of the collar. Because the last tap was not located precisely at the end of the collar due to the highly curved collar lip, the pressure measured there was not typically

atmospheric. Therefore, the pressure distribution was estimated to decrease linearly from the last measured pressure,  $-\Delta P_{c,m}$ , to zero at the end of the collar. The variable  $n$  in this expression represents the number of additional incremental areas ( $\Delta A_c$  as defined above) required to cover the area from the last tap to the collar end. The collar end is defined such that  $\phi_n$  had a value of  $\alpha + 90^\circ$ . Typically,  $n$  has values of 3 or 4 depending on the collar geometry. While this estimated pressure distribution seems somewhat arbitrary, it was consistent with the above assumption that the pressure at the collar end boundary should be atmospheric. Furthermore, since the angles of force application on the collar lip ( $\phi_j$ ) were on the order of  $90^\circ$ , the forces near the collar lip had little impact on  $F_{cy}$  and so affected the thrust vector angle calculation little (see below).

Returning to Eq. (19), the components of  $F_G$  are easily calculated since  $A_G$  ( $A_G = G*W$ , the gap area) is aligned with the y-axis:

$$F_{Gx} = -\Delta P_{exit} * A_G \quad \text{and} \quad F_{Gy} = 0$$

Therefore:

$$\Sigma F_x = F_{cx} + F_{Gx} \quad \text{and} \quad \Sigma F_y = F_{cy}$$

Note that for this analysis that the positive x-component pressure forces act in the negative x-direction.

Turning to the momentum balance, the momentum leaving the control volume through the downstream boundary is assumed to be the

momentum entering the control volume through the nozzle exit multiplied by a thrust coefficient  $C_T$ . Momentum entering the control volume as a result of the reverse flow is considered negligible because much of the reverse flow originates from the primary jet and the remaining flow enters the control volume over the large surface area between where the primary jet leaves the control volume and the collar. Thus the resulting momentum entering this region would be small due its low mass flow and velocity (e.g. estimates suggest that  $(\dot{m}u)_2/(\dot{m}u)_1$  here is on the order of  $10^{-3}$ ). Thus, the total momentum flux through the control volume due to these factors can be written:

$$\int_S \rho u(u \cdot n) dA = C_T \int_{A_e} \rho u(u \cdot n) dA + \int_{A_e} \rho u(u \cdot n) dA + \int_{A_G} \rho u(u \cdot n) dA$$

The momentum flux at the downstream boundary exits the control volume at the thrust vector angle,  $\delta_v$ . The other fluxes enter and exit the control volume parallel to the x-axis. The sign of the momentum fluxes depend on whether the associated mass flow is leaving (positive) or entering (negative) the control volume and on the direction of the associated velocity. The x-y components of the total momentum flux are then:

$$\int_S \rho u_x(u \cdot n) dA = C_T \cos \delta_v \int_{A_e} \rho_1 U_1^2 dA - \int_{A_e} \rho_1 U_1^2 dA - \int_{A_G} \rho_{atm} U_2^2 dA$$

and

$$\int_S \rho u_y(u \cdot n) dA = C_T \sin \delta_v \int_{A_e} \rho_1 U_1^2 dA$$

Since  $U_1$  was shown to be essentially constant over the nozzle exit (see Figs. 13 and 14) and  $U_2$  is defined as being the average velocity over the gap height (see the end of Section 4.2.2), the x-y components of the total momentum flux can then be written simply as:

$$\int_S \rho u_x (\mathbf{u} \cdot \mathbf{n}) dA = C_T \cos \delta_v (\dot{m}U)_1 - (\dot{m}U)_1 - (\dot{m}U)_2 \quad (23)$$

and

$$\int_S \rho u_y (\mathbf{u} \cdot \mathbf{n}) dA = C_T \sin \delta_v (\dot{m}U)_1 \quad (24)$$

From the momentum equation (Eq. (18)), the x and y component forces are then equal to the component momentum fluxes:

$$\Sigma F_x = C_T \cos \delta_v (\dot{m}U)_1 - (\dot{m}U)_1 - (\dot{m}U)_2 \quad \text{and} \quad \Sigma F_y = C_T \sin \delta_v (\dot{m}U)_1$$

rearranging:

$$C_T \cos \delta_v (\dot{m}U)_1 = \Sigma (\dot{m}U)_x + \Sigma F_x \quad \text{and} \quad C_T \sin \delta_v = \Sigma F_y \quad (25a \text{ and } b)$$

where  $\Sigma (\dot{m}U)_x = (\dot{m}U)_1 + (\dot{m}U)_2$ . Dividing Eq. (25b) by Eq. (25a), the expression for thrust vector angle  $\delta_v$  is then:

$$\delta_v = \tan^{-1} \left[ \frac{\Sigma F_y}{\Sigma (\dot{m}U)_x + \Sigma F_x} \right] \quad (6)$$

which is the expression given previously in Section 4.2.3. By squaring and adding Eqs. (25a and 25b) and then dividing by the primary momentum through the nozzle exit, the following expression is attained:

$$C_T^2(\cos^2\delta_v + \sin^2\delta_v) = \frac{[\Sigma(\dot{m}U)_x + \Sigma F_x]^2 + (\Sigma F_y)^2}{(\dot{m}U)_1^2}$$

Taking the square root of this expression, the equation for  $C_T$  (also given in Section 4.2.3) is then:

$$C_T = \frac{\sqrt{[\Sigma(\dot{m}U)_x + \Sigma F_x]^2 + (\Sigma F_y)^2}}{(\dot{m}U)_1} \quad (7)$$

$C_T$  represents the magnitude of the pressure and momentum losses associated with turning the primary jet using counterflow.

## REFERENCES

Boggs, R. N., "Nozzle Combines Vectored and Reverse Thrust," *Design News*, Vol. 49, No. 8, 1993, pp. 99-100.

Bourque, C., and Newman, B.G., "Reattachment of a Two-Dimensional Incompressible jet to an Adjacent Flat Plate," *Aeronautical Quarterly*, Vol. XI, 1960, pp. 201-232.

Bursey, R. N., Berger, C. W., and DeFreese, C. G., "Pratt & Whitney Vectoring Team Turns Imagineering into Reality," Pratt & Whitney Government Engines & Space Propulsion Paper, West Palm Beach, FL, 3 November 1993.

Capone, F., Smereczniak, P., Spetnagel, D., and Thayer, E., "Comparative Investigation of Multiplane Thrust Vectoring Nozzles," AIAA/SAE/ASME/ASEE 28th Joint Propulsion Conference and Exhibit, AIAA Paper 92-3264, July 1992.

Carrol, G. R., and Cox, H., "A Missile Flight Control System using Boundary Layer Thrust Vector Control," AIAA/SAE/ASME/ASEE 19th Joint Propulsion Conference, AIAA Paper 83-1149, June 1983.

Comparin, R. A., Mitchell, A. E., Mueller, H. R., and Glaettli, H. M., "On the Limitations and Special Effects in Fluid Jet Amplifiers," ASME Symposium on Fluid Jet Control Devices, New York, NY, 28 November 1962.

Cornelius, K. C., and Lucius, G. A., "Thrust Vectoring Control from Underexpanded Asymmetric Nozzles," AIAA 3rd Shear Flow Conference, AIAA Paper 93-3261, July 1993.

Doonan, J.G., and Kuchar, A.P., "Scale Model Test Results of a Multi-Slotted 2DCD Ejector Nozzle," AIAA/SAE/ASME/ASEE 28th Joint Propulsion Conference and Exhibit, AIAA Paper 92-3264, July 1992.

Eskinazi, S., and Yeh, H., "An Investigation on Fully Developed Turbulent Flows in a Curved Channel," *Journal of Aerospace Science*, Vol. 23, 1956, p. 23.

Fitzgerald, R.E., and Kampe, R.F., "Boundary Layer TVC for Missile Applications," AIAA/SAE/ASME/ASEE 19th Joint Propulsion Conference, AIAA Paper 83-1153, June 1983.

Franke, M.E., "Supersonic Confined Jet Devices," *FLUCOME '91*, ASME 3rd Triennial International Symposium on Fluid Control, Measurement, and Visualization, August 1991.

Friddell, J.H., and Franke, M.E., "Confined Jet Thrust Vector Control Nozzle Studies," *AIAA Journal of Propulsion and Power*, Vol. 8, No. 6, 1992, pp. 1239-1244.

Gilbert, B., "Directional Control of Large Mass Flows by Fluidics," *FLUCOME '91*, ASME 3rd Triennial International Symposium on Fluid Control, Measurement, and Visualization, August 1991.

Grandmaison, E. W., Pollard, A., and Ng, S., "Scalar Mixing in a Free, Turbulent Rectangular Jet," *International Journal of Heat and Mass Transfer*, Vol. 34, No. 10, 1991, pp. 2653-2662.

Green, S.M., and Glezer, A., "The Manipulation of Turbulent Jets using Surface-Mounted Actuators," AFOSR Contractor Meeting Report, Grant 89-0465 Flagstaff, AZ, August 1993.

Henderson, W. P., "Propulsion Systems Integration in High Performance Aircraft," *Aerospace Engineering*, Vol. 10, No. 2, 1990, pp. 21-25.

Kibens, V., Parekh, D.E., Joshi, M.C., and Glezer, A., "Active-Control-Enhanced Mixing Mechanisms in Rectangular Jets," *Bulletin of the American Physical Society*, Vol. 39, No. 9, 1994, p. 1893.

Lepicovsky, J., Ahuja, K.K., Brown, W.H., Salakuddin, M., and Morris, P.J., "Acoustically Excited Heated Jets," NASA CR-4129, part I - III, 1988.

Loehrke, R. I., and Nagib, H. M., "Control of Free-Stream Turbulence by Means of Honeycombs: A Balance Between Suppression and Generation," *Journal of Fluids Engineering*, Vol. 98, 1976, pp. 483-491.

Margolis, D.P., and Lumley, J.L., "Curved Turbulent Mixing Layer," *Physics of Fluids*, Vol. 8, No. 10, 1965, pp. 1775-1784.

McGlaughlin, D.W., and Greber, I., "Experiments on the Separation of a Fluid Jet From a Curved Surface," *Advances in Fluidics*, ASME, New York, NY, 1967, pp. 14-30.

McRee, D.I., and Moses, H.L., "The Effect of Aspect Ratio and Offset on Nozzle Flow and Jet Reattachment," *Advances in Fluidics*, ASME, New York, NY, 1967, pp. 142-161.

Mishler, R., and Wilkinson, T., "Emerging Airframe/Propulsion Integration Technologies at General Electric," AIAA/SAE/ASME/ASEE 28th Joint Propulsion Conference and Exhibit, AIAA Paper 92-3335, July 1992.

Niccum, D.L., "The Influence of Velocity Ratio on a Counterflowing Circular Jet," M.S. Thesis, University of Minnesota, Minneapolis, MN, December 1990.

Olson, R.E., "Reattachment of a Two-dimensional Compressible Jet to an Adjacent Plate," ASME Symposium on Fluid Jet Control Devices, New York, NY, 28 November 1962.

Papamoschou, D., and Roshko, A., "The Compressible Turbulent Shear Layer," *Journal of Fluid Mechanics*, Vol. 197, 1988, pp. 453-477.

Porzio, A.J., and Franke, M.E., "Experimental Study of a Confined Jet Thrust Vector Control Nozzle," *AIAA Journal of Propulsion and Power*, Vol. 5, No. 5, 1989, pp. 596-601.

Raman, G., Zaman, K.B.M.Q., and Rice, E.J., "Initial Turbulence Effect on Jet Evolution With and Without Tonal Excitation," *Physics of Fluids A*, Vol. 1, 1989, pp. 1240-1248.

Rayleigh, J.W.S., "On the Dynamics of Revolving Fluids," *Proceedings of the Royal Society, A*, Vol. XCIII, 1916, pp. 148-154. Also, *Scientific Papers by Lord Rayleigh*, Dover, New York, NY, Vol. 6, 1964, pp. 447-453.

Reisenthal, P., "Hybrid Instability in an Axisymmetric Jet with Enhanced Feedback," Ph.D. Thesis, Illinois Institute of Technology, Chicago, IL, May 1988.

Shih, C., Krothapalli, A., and Gogineni, S., "Experimental Observations of Instability Modes in a Rectangular Jet," *AIAA Journal*, Vol. 30, No. 10, 1992, pp. 2388-2394.

Snow, B.H., "Thrust Vectoring Control Concepts and Issues," SAE Technical Paper Series, Aerospace Technology Conference and Exposition, paper 901848, Long Beach, CA, October 1990.

Squire, H.B., "Jet Flow and Its Effects on Aircraft," *Aircraft Engineering*, Vol. 22, 1950, pp. 62-67.

Strykowski, P.J., and Krothapalli, A., "The Countercurrent Mixing Layer: Strategies for Shear-Layer Control," AIAA 3rd Shear Flow Control Conference, AIAA Paper 93-3260, July 1993.

Strykowski, P.J., Krothapalli, A., and Jendoubi, S., "The Effect of Counterflow on the Development of Compressible Shear Layers," submitted to *Journal of Fluid Mechanics*, January 1995.

Strykowski, P.J., Krothapalli, A., and Wishart, D., "The Enhancement of Mixing in High-Speed Heated Jets Using a Counterflowing Nozzle," AIAA/SAE/ASME/ASEE 28th Joint Propulsion Conference and Exhibit, AIAA Paper 92-3262, July 1992.

Strykowski, P.J., and Niccum, D.L., "The Stability of Countercurrent Mixing Layers in Circular Jets," *Journal of Fluid Mechanics*, Vol. 227, 1991, pp. 309-343.

Strykowski, P.J., and Niccum, D.L., "The Influence of Velocity and Density Ratio on the Dynamics of Spatially Developing Mixing Layers," *Physics of Fluids A*, Vol. 4, No. 4, 1992, pp. 770-781.

Strykowski, P.J., and Wilcoxon, R.K., "Mixing Enhancement due to Global Oscillations in Jets with Annular Counterflow," *AIAA Journal*, Vol. 31, No. 3, 1993, pp. 564-570.

Viets, H., "Flip-Flop Jet Nozzle," *AIAA Journal*, Vol. 13, No. 10, 1975, pp. 1375-1379.

Warren, R.W., "Some Parameters Affecting the Design of Bistable Fluid Amplifiers," ASME Symposium on Fluid Jet Control Devices, New York, NY, 28 November 1962.

Wilson, D.J., "An Experimental Investigation of the Mean Velocity, Temperature and Turbulence Fields in Plane and Curved Two-Dimensional Wall Jets: Coanda Effect," Ph.D. Thesis, University of Minnesota, Minneapolis, MN, December 1970.

Young, T., "Outlines of Experiments and Inquiries Respecting Sound and Light," Lecture to the Royal Society, 16 January 1800. (See *Journal of the Royal Aeronautical Society*, Vol. 61, 1957, p. 157.)

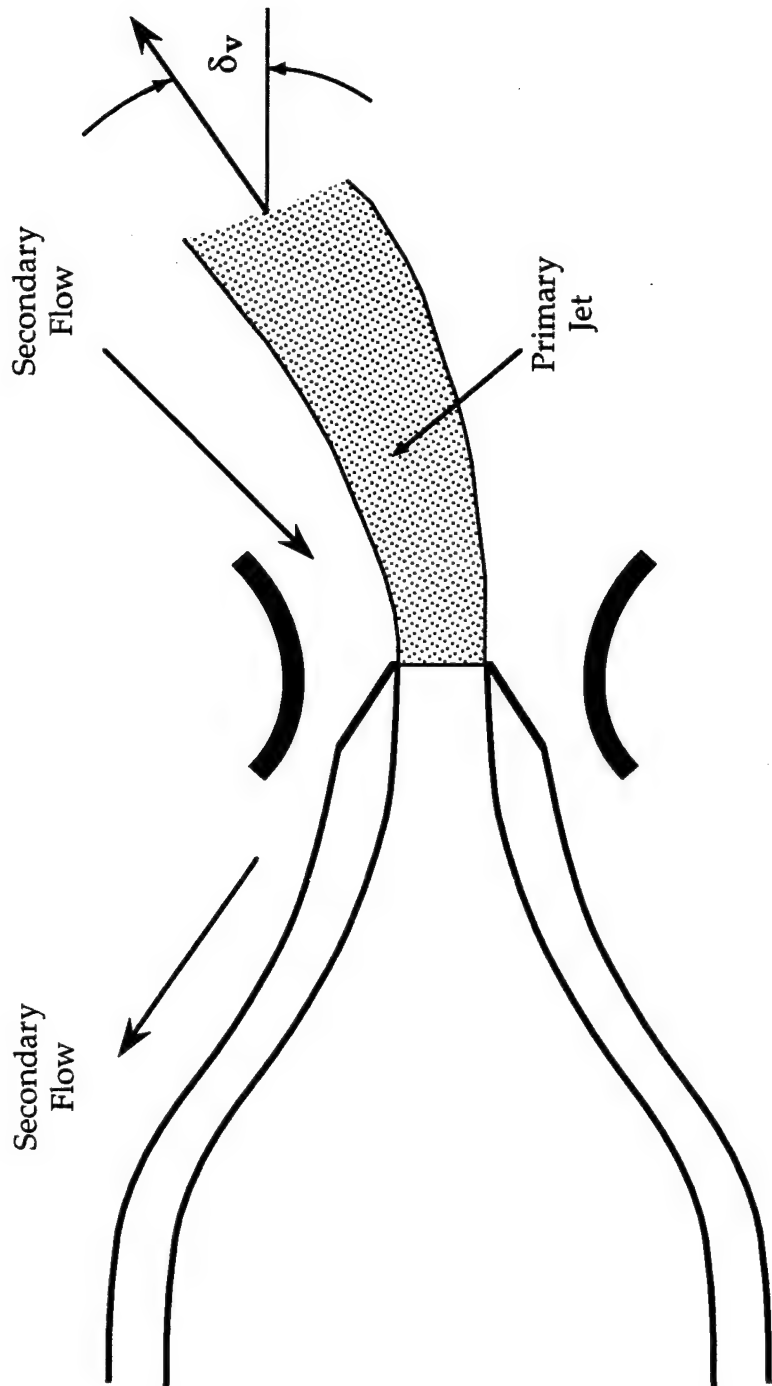


Figure 1. Schematic of the fluidic thrust vector nozzle showing vectoring when counterflow is activated in the upper shear layer of the jet.

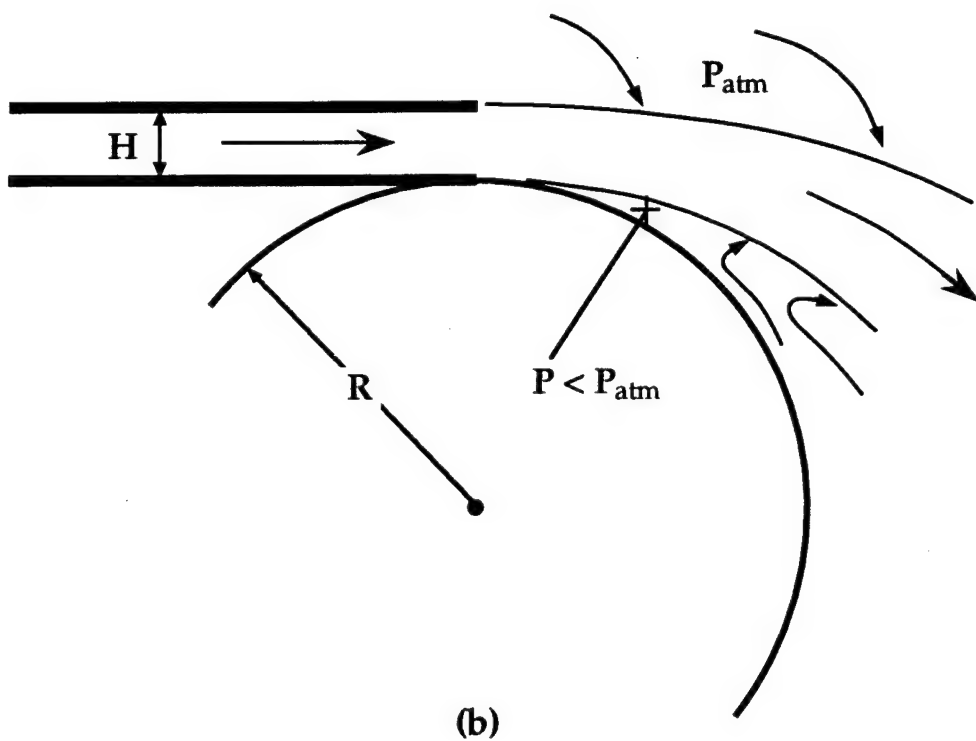
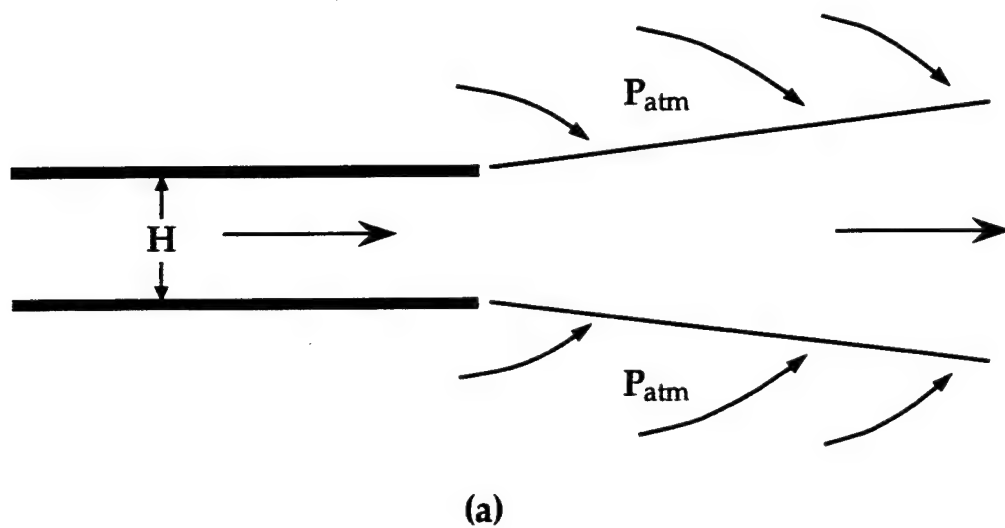
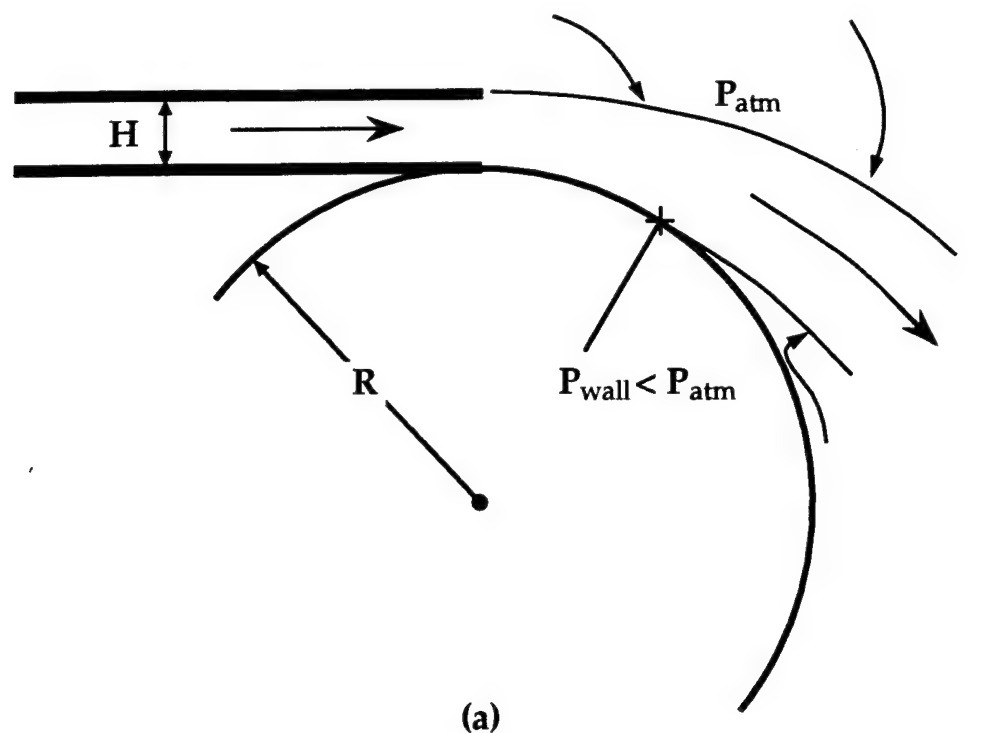
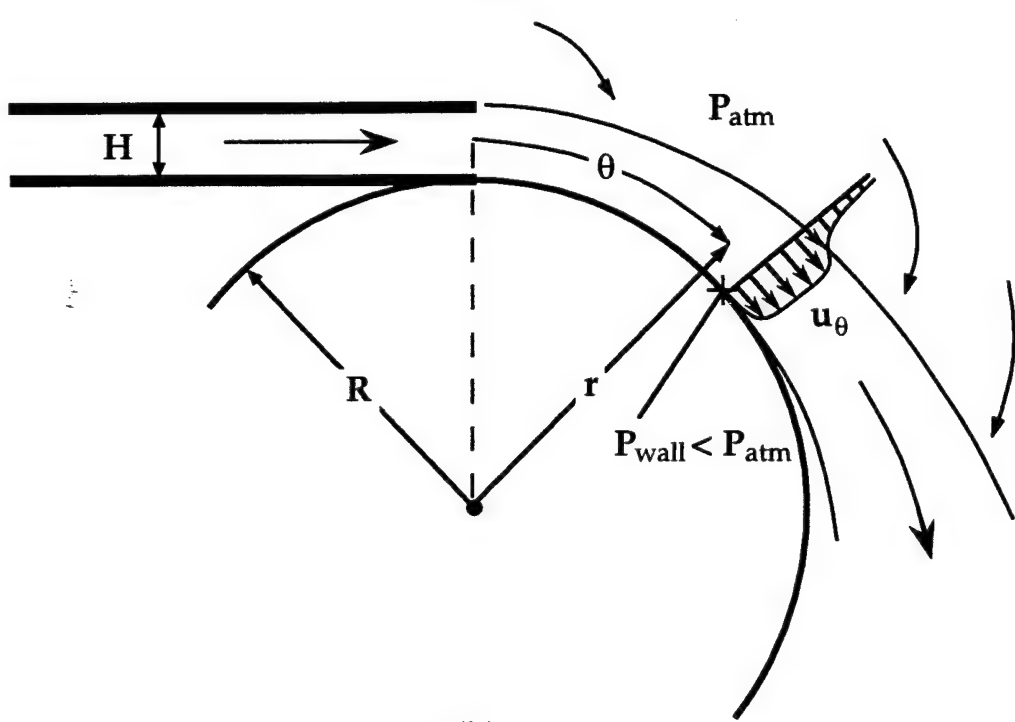


Figure 2. Two-dimensional jet of height  $H$ . (a) As a free jet entraining the surrounding fluid. (b) As a jet in the presence of a curved surface of radius  $R$  illustrating the Coanda effect. Pressure near the surface is low causing jet deflection.



(a)



(b)

Figure 3. Jet attaches to the curved surface in (a). In (b), the jet continues attachment until it can no longer entrain enough fluid to maintain a low enough pressure to prevent separation. The curved wall jet along the  $\theta$  axis is stable due to the positive pressure gradient in the positive  $r$  direction.

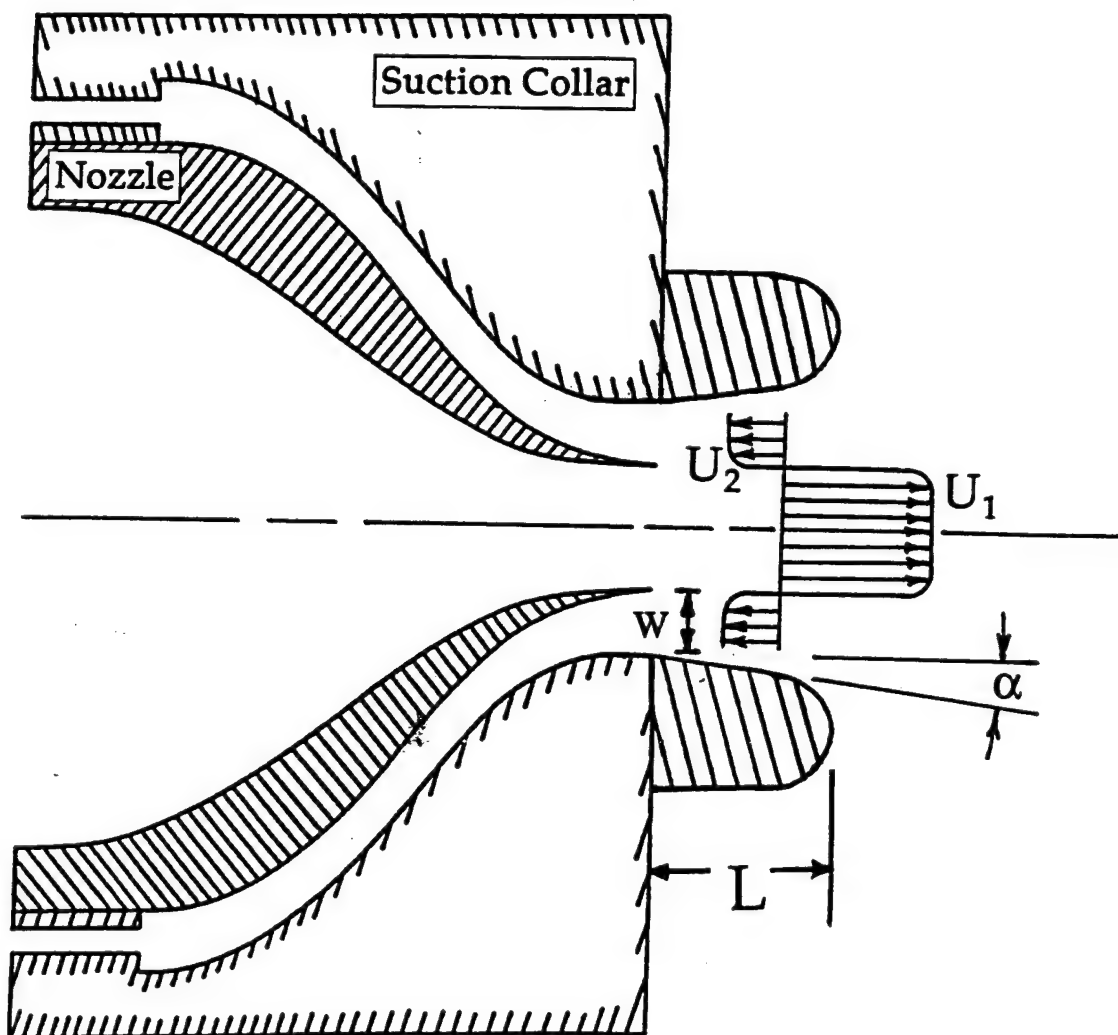
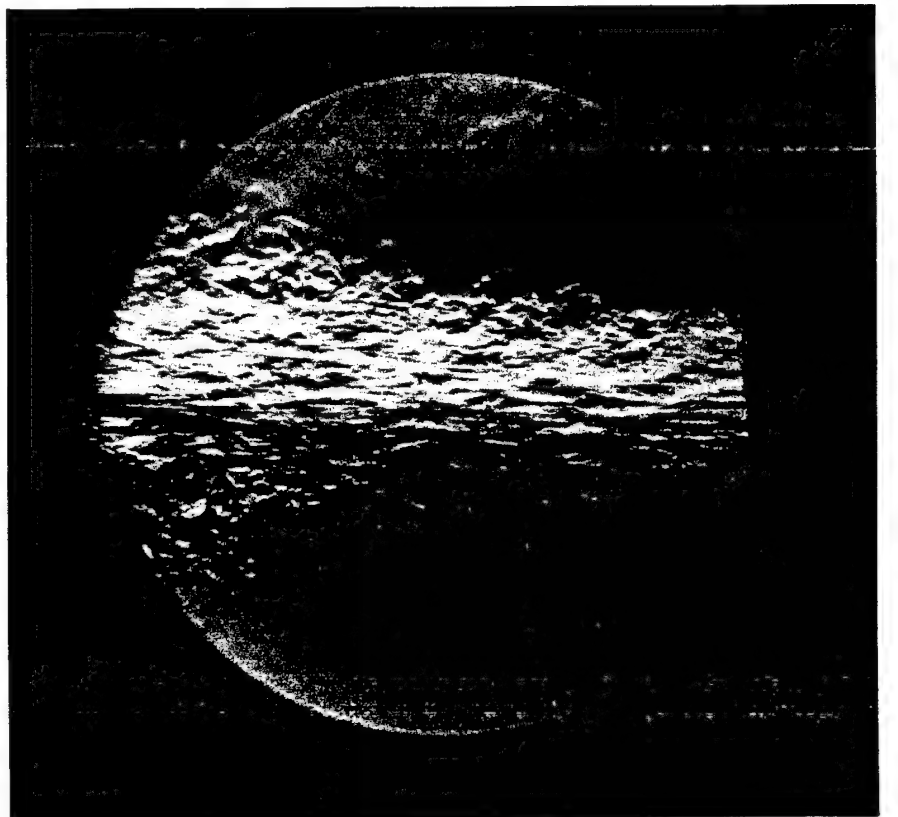
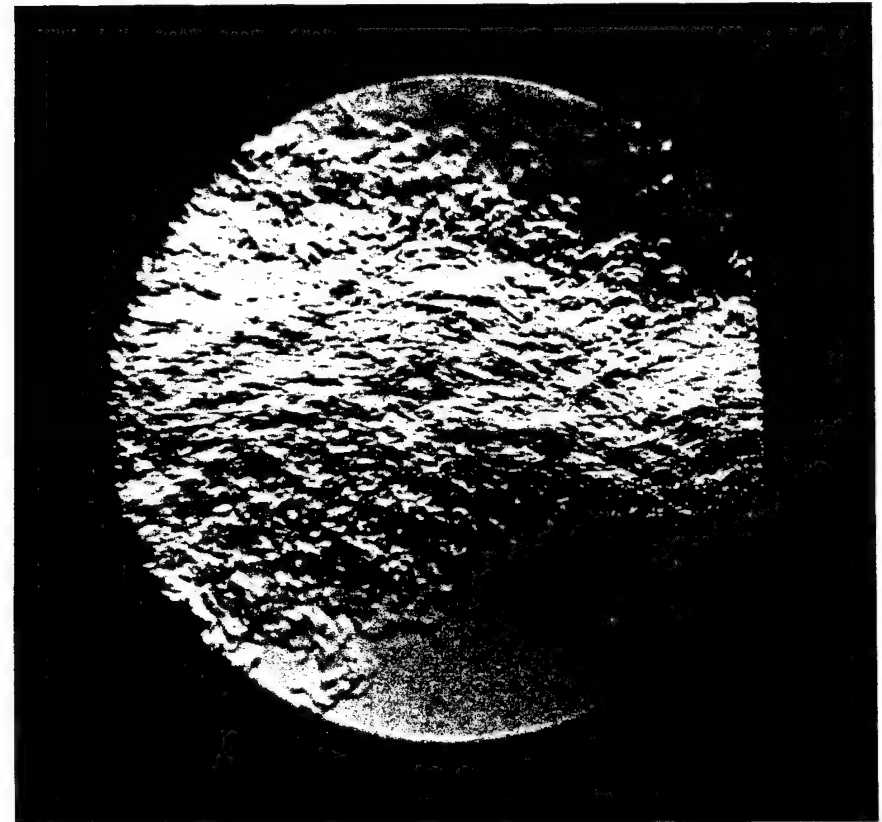


Figure 4. Nozzle-collar configuration used to generate an axisymmetric countercurrent mixing layer (from Strykowski and Wilcoxon 1993; with permission).



(a)



(b)

Figure 5. Schlieren photographs of an axisymmetric jet at  $ReD = 7.8 \times 10^4$  using the facility from Fig. 4. The photograph in (a) was taken without suction and (b) was obtained at a velocity ratio of  $-U_2/U_1 \approx 0.35$  (from Strykowski and Wilcoxon 1993; with permission).

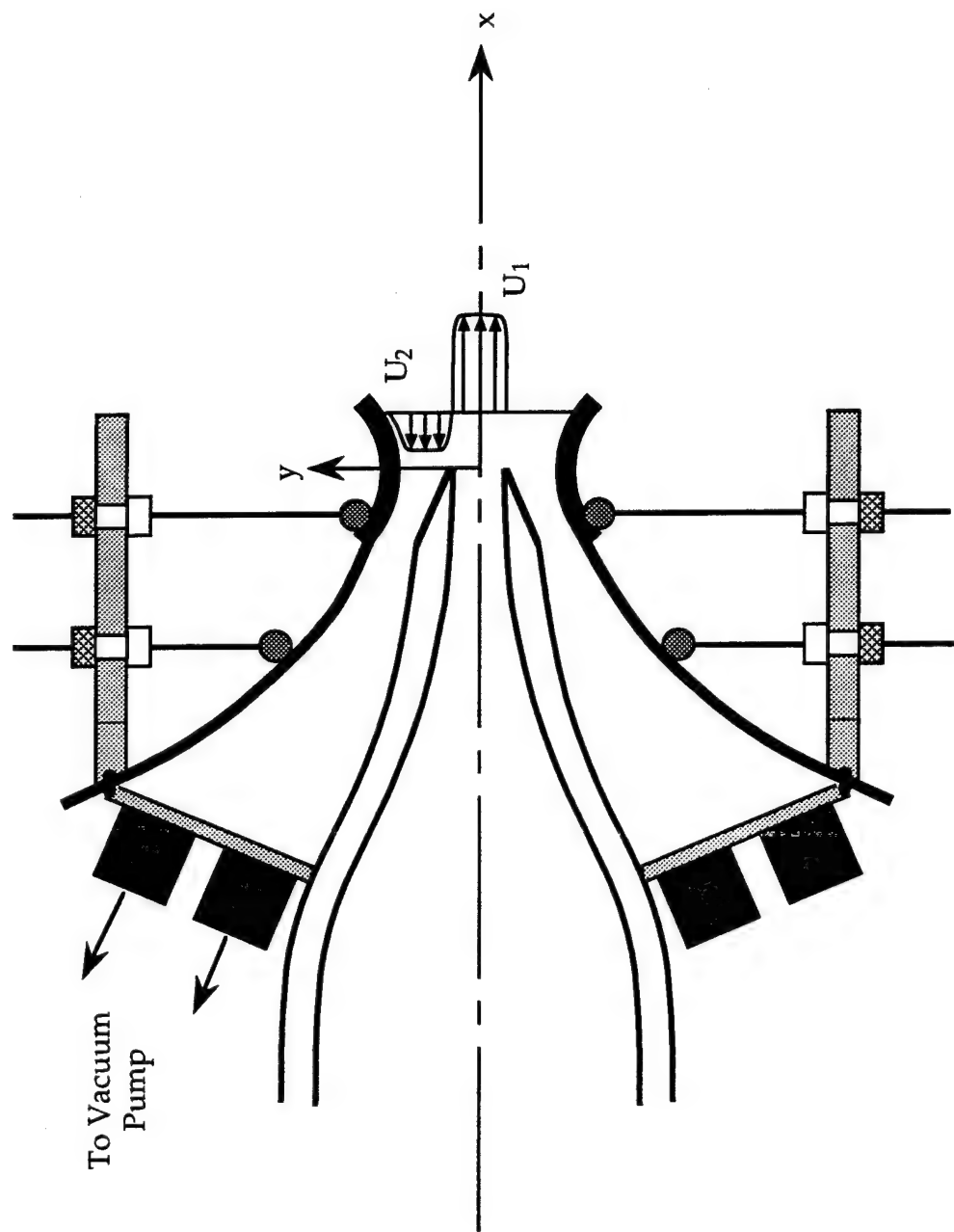


Figure 6.  
Scaled drawing of the nozzle-collar assembly used for counterflow vectoring.  
The forward stream  $U_1$  and secondary stream  $U_2$  are defined in a coordinate system  
having an origin in the nozzle exit plane

Figure 6.

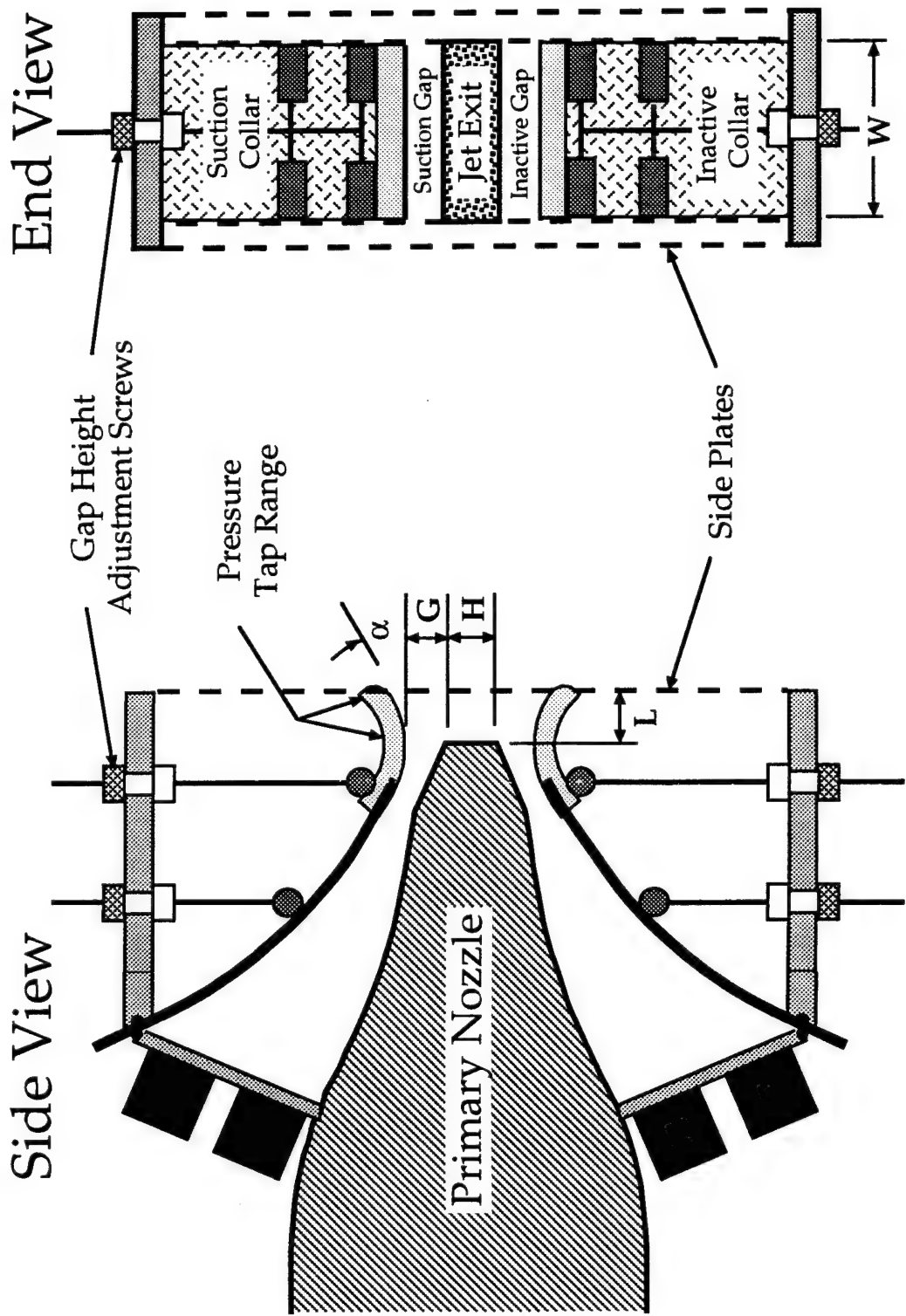


Figure 7. Scaled drawing of the internal dimensions of the side and end views of the nozzle-collar configuration. The  $L = 1$  cm,  $\alpha = 30^\circ$  collar is shown.

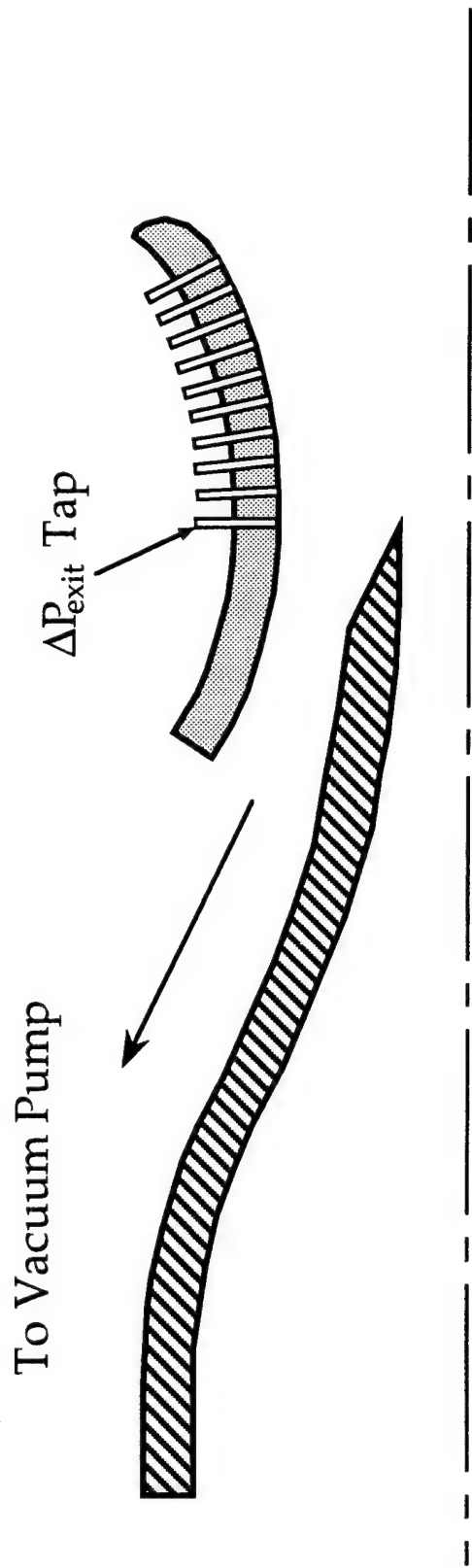


Figure 8. Schematic showing the approximate distribution of one row of the static pressure collar wall taps. The location of tap used to measure gage exit pressure,  $\Delta P_{exit}$ , is also indicated. The collar having  $L/H = 3.5$  is shown.

### Side View

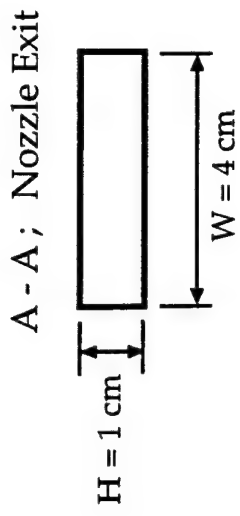
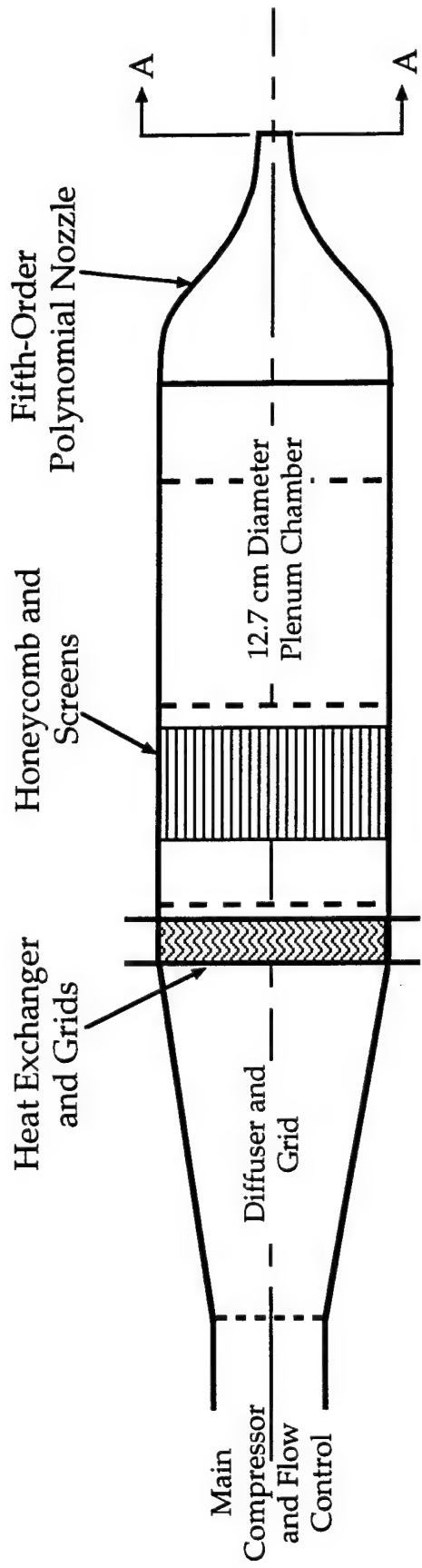


Figure 9. Schematic of the test facility used to generate the forward velocity stream. The air exhausts into the laboratory from a rectangular nozzle shown in cross section A-A. The main drawing is not to scale.

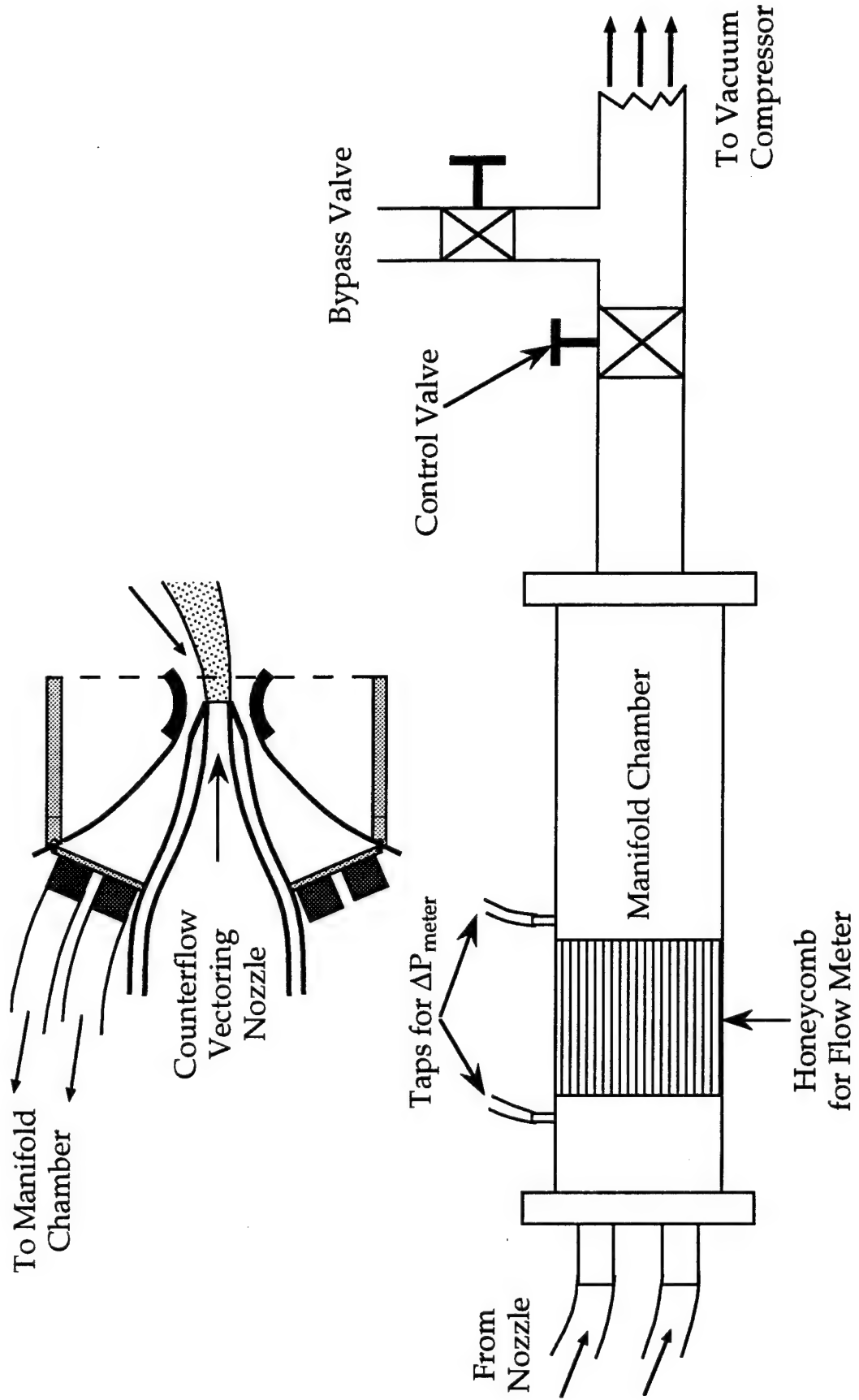


Figure 10. Schematic of the reverse flow assembly. The drawing is not to scale.

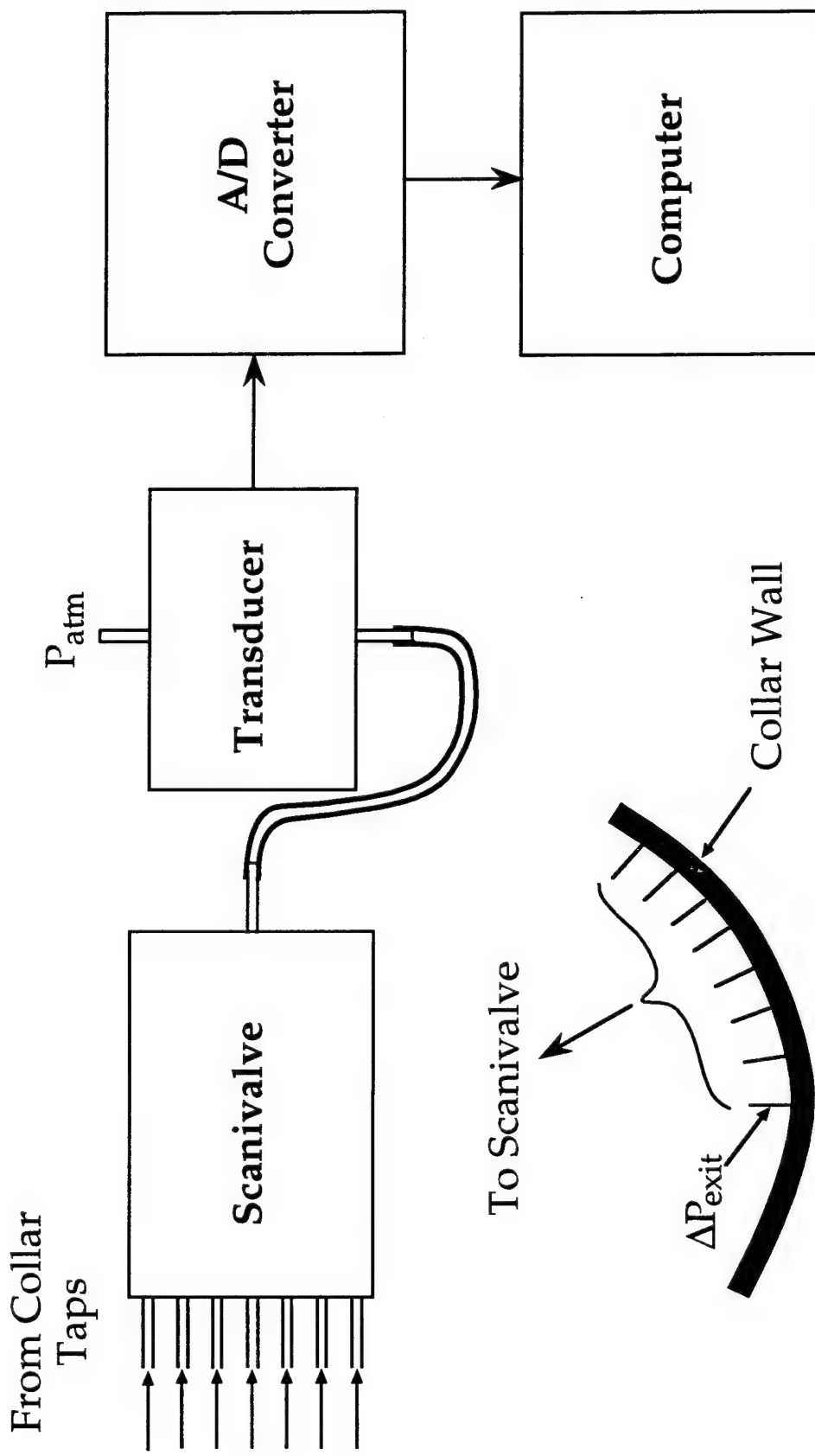


Diagram illustrating the integration of the Scaniivalve with the static pressure taps placed along the collar wall. Static collar wall pressure distributions were sampled by the voltmeter and then passed to the computer for processing.

Figure 11.

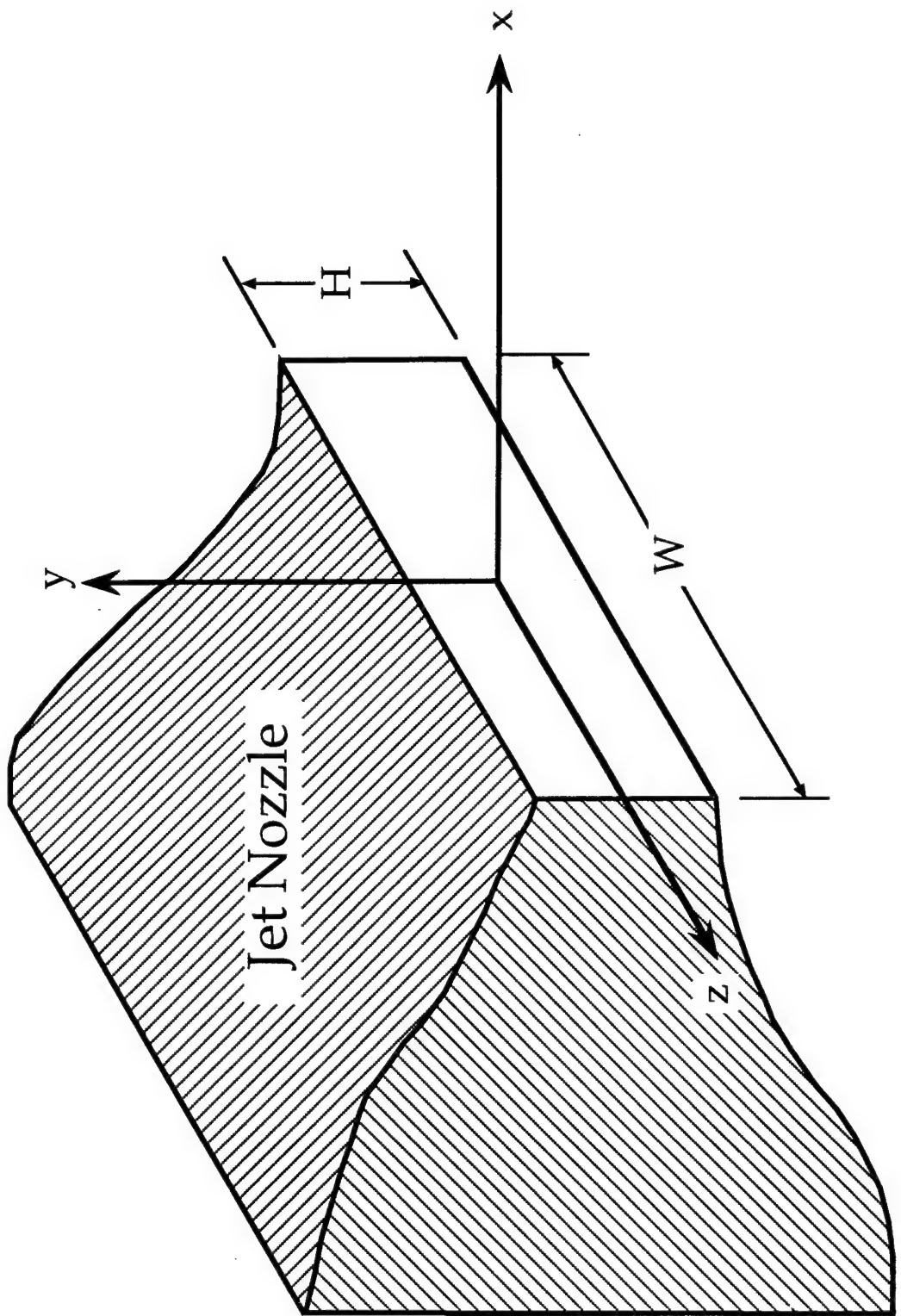


Figure 12. Coordinate system for standard jet measurements.

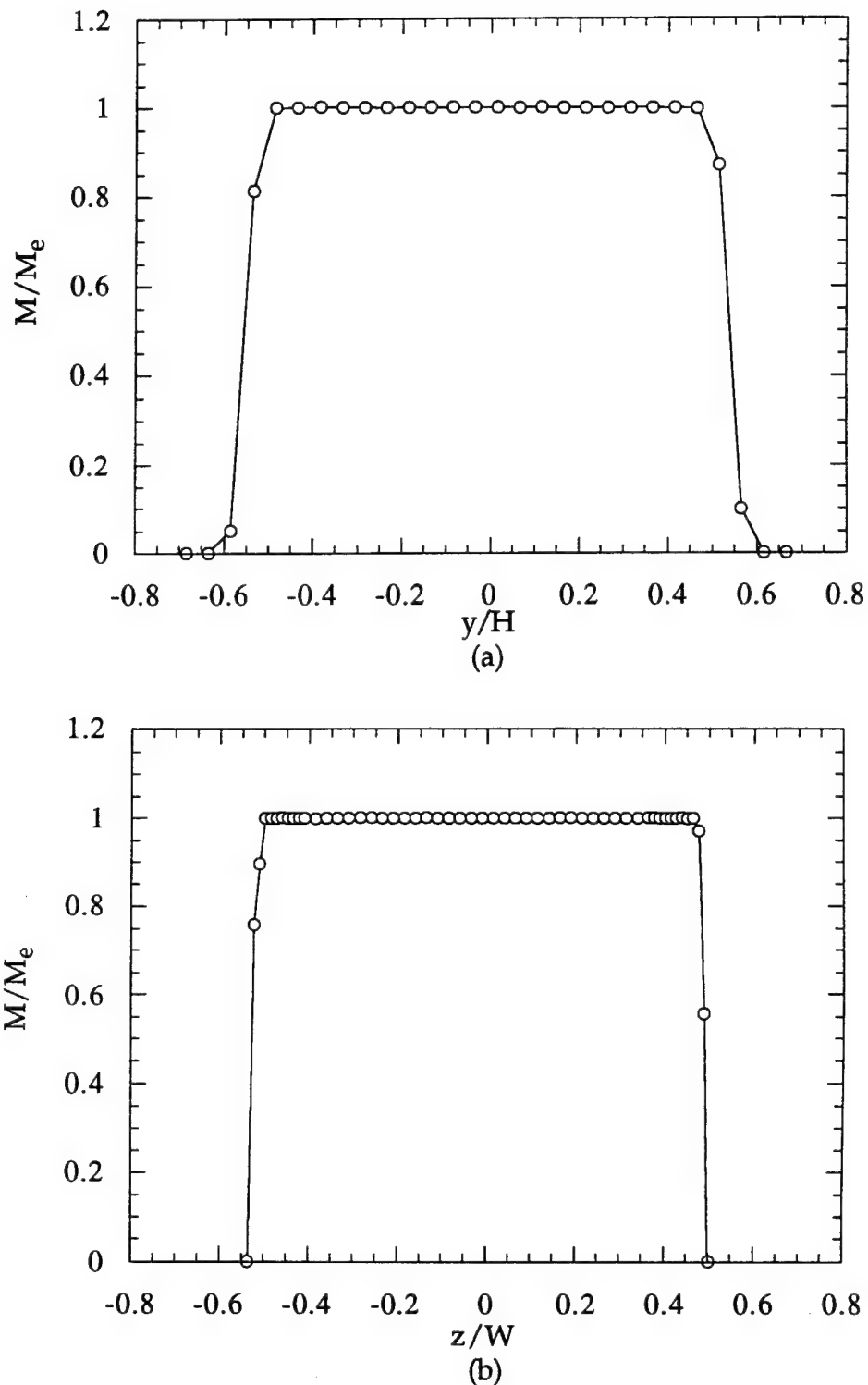


Figure 13. Mean Mach profiles along the (a)  $y$ -axis and (b)  $z$ -axis of the standard jet without any collar attached. Profiles were obtained at  $Re_H = 1.16 \times 10^5$  ( $M_e = 0.5$ ) and  $x/H = 0.05$ .

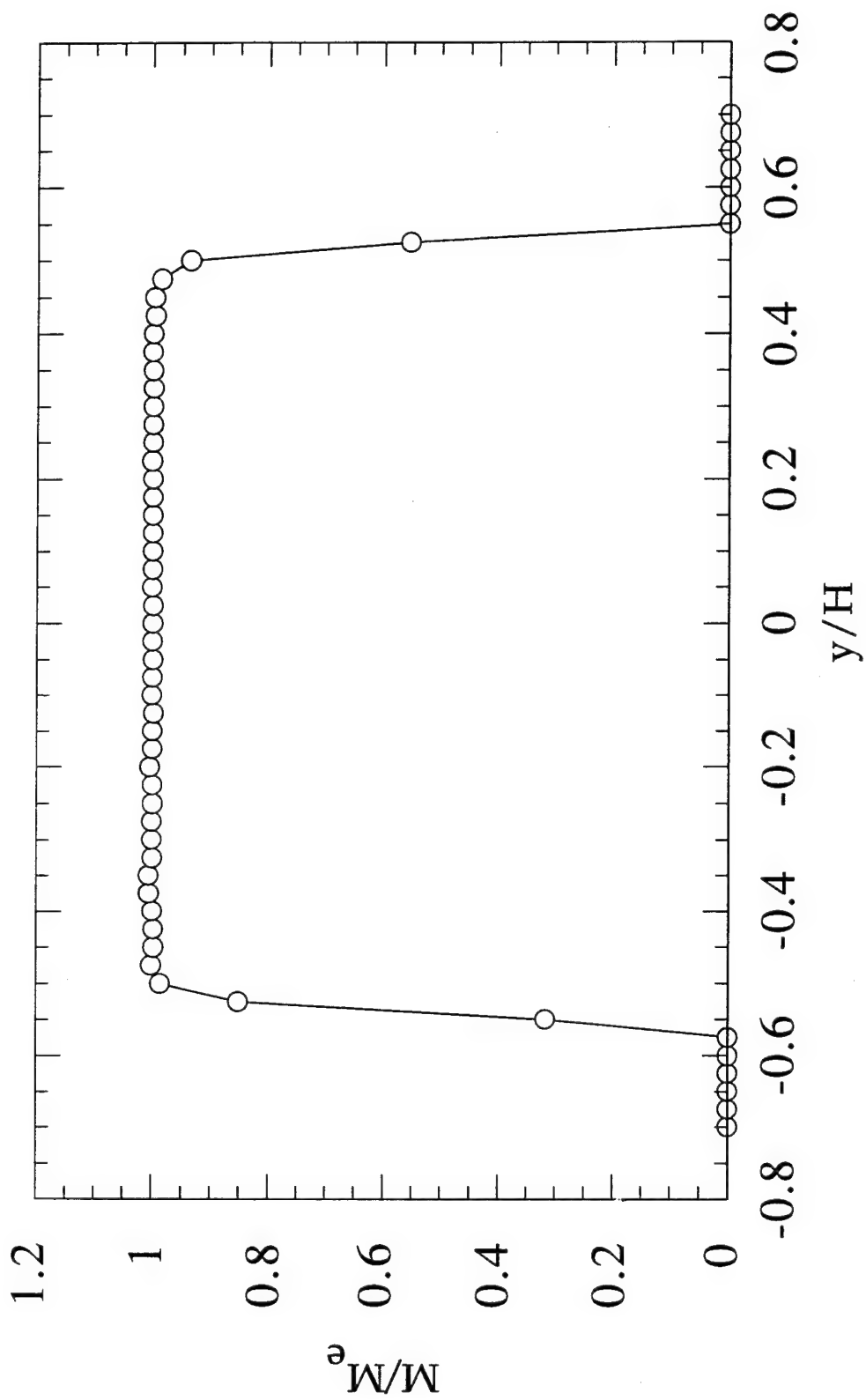


Figure 14. Mean Mach profile along  $y$ -axis for the standard jet with representative collar attached. The profile was obtained at  $ReH = 1.16 \times 10^5$  ( $M_e = 0.5$ ) and  $x/H = 0.05$ .

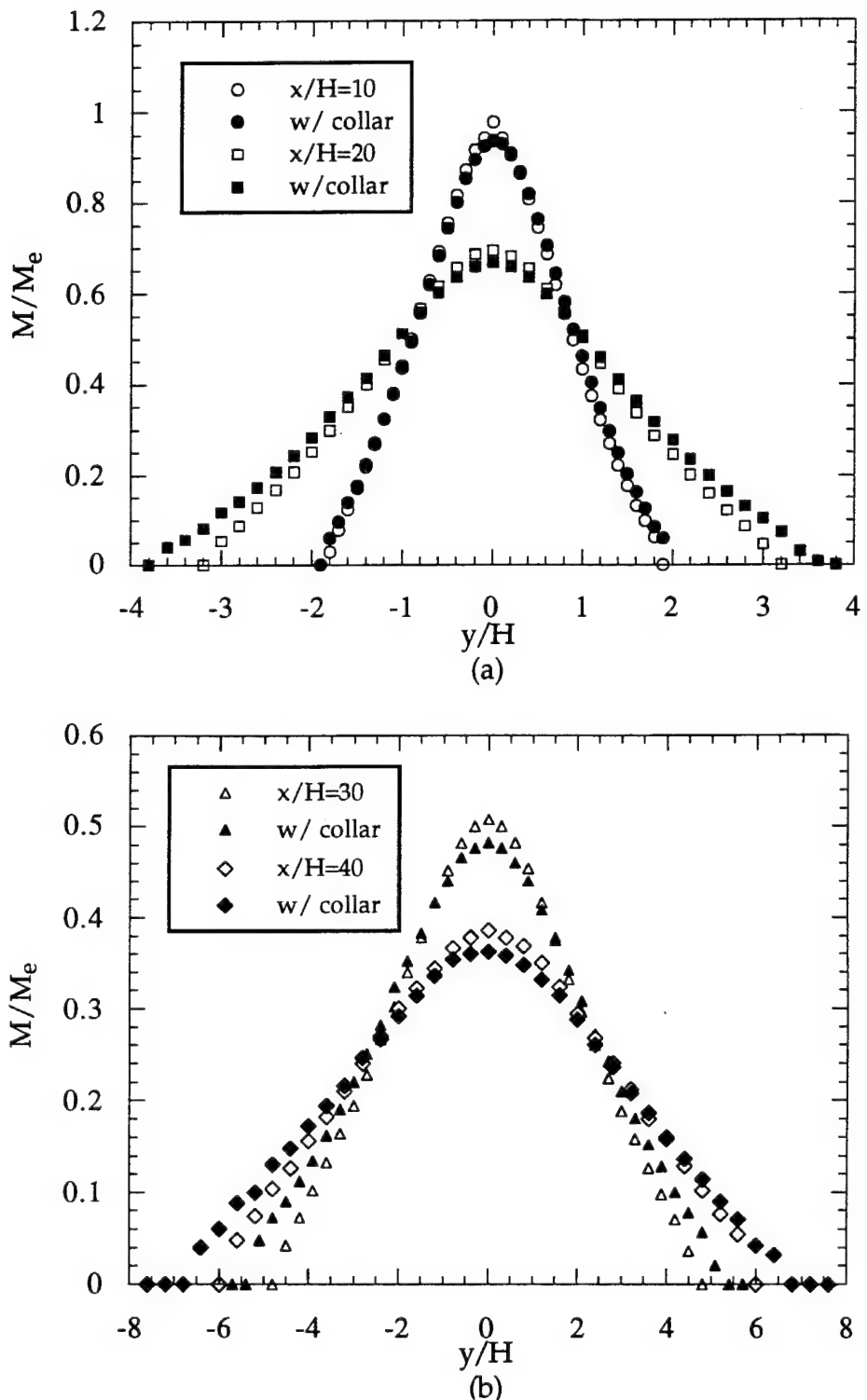


Figure 15. Mean downstream Mach profiles comparing standard jet with and without a collar. Profiles are at (a)  $x/H = 10$  and  $20$ , and (b)  $x/H = 30$  and  $40$ . Exit flow conditions were  $Re_H = 1.16 \times 10^5$ .

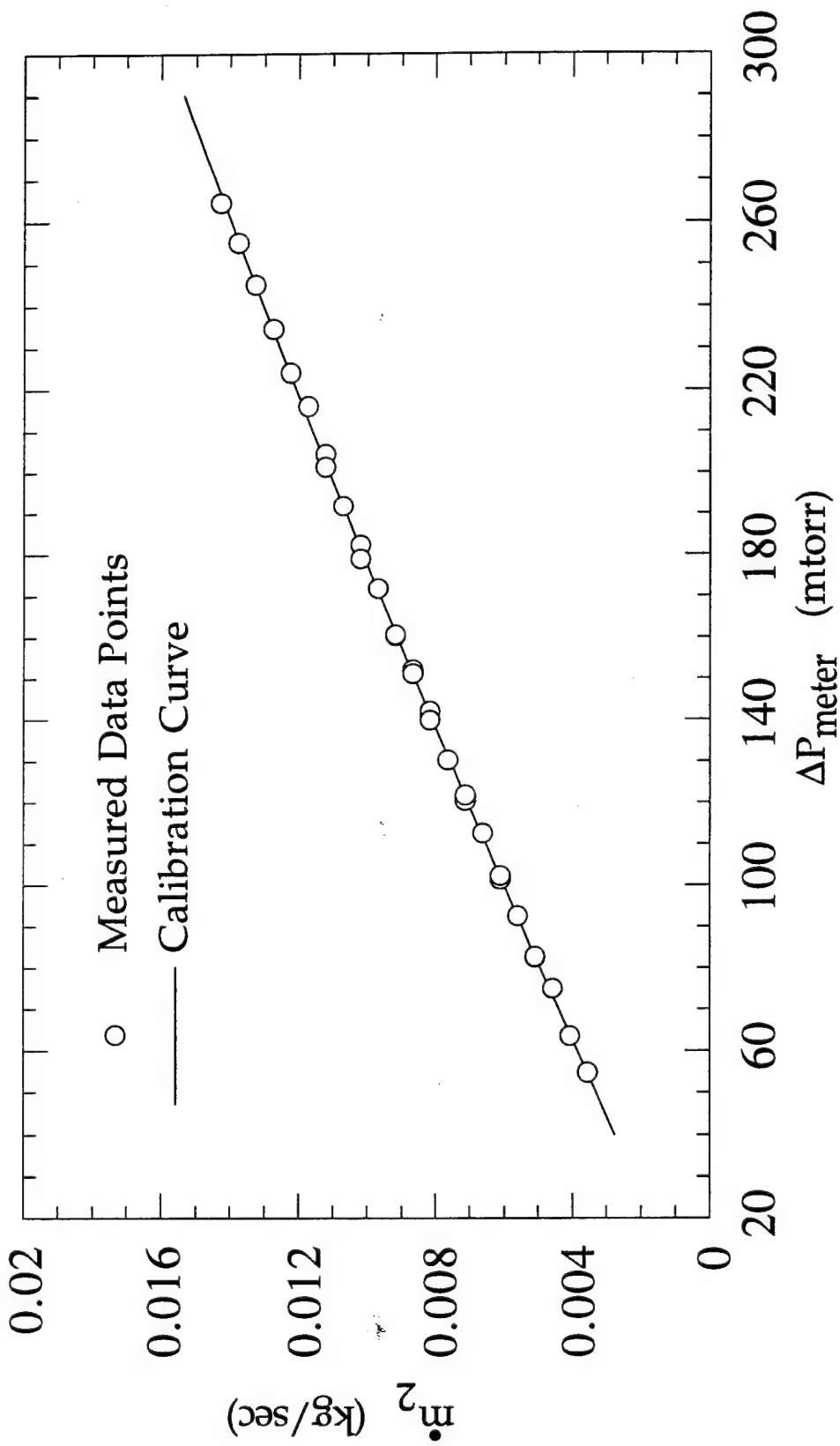


Figure 16. Calibration curve of the pressure drop across the reverse flow meter versus the rotameter reading. Best fit is plotted as solid line.

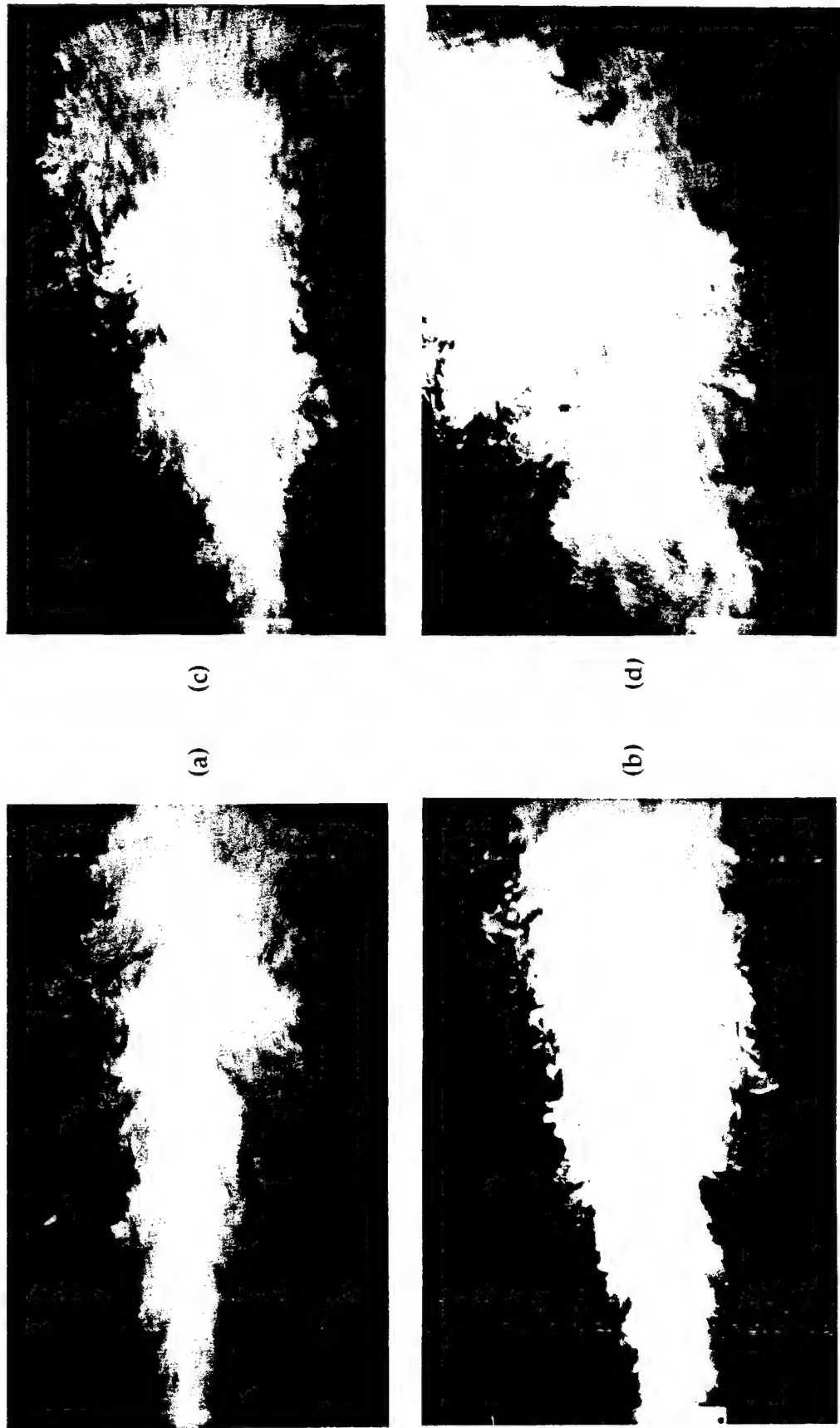


Figure 17. Thrust vector angle determined by flow visualization. The jet is illuminated by using injected smoke particles to scatter a laser sheet. Angles of (a)  $0^\circ$ , (b)  $6^\circ$ , (c)  $13^\circ$  and (d)  $27^\circ$  are shown. This  $L/H=0$  collar was used for flow visualization only.

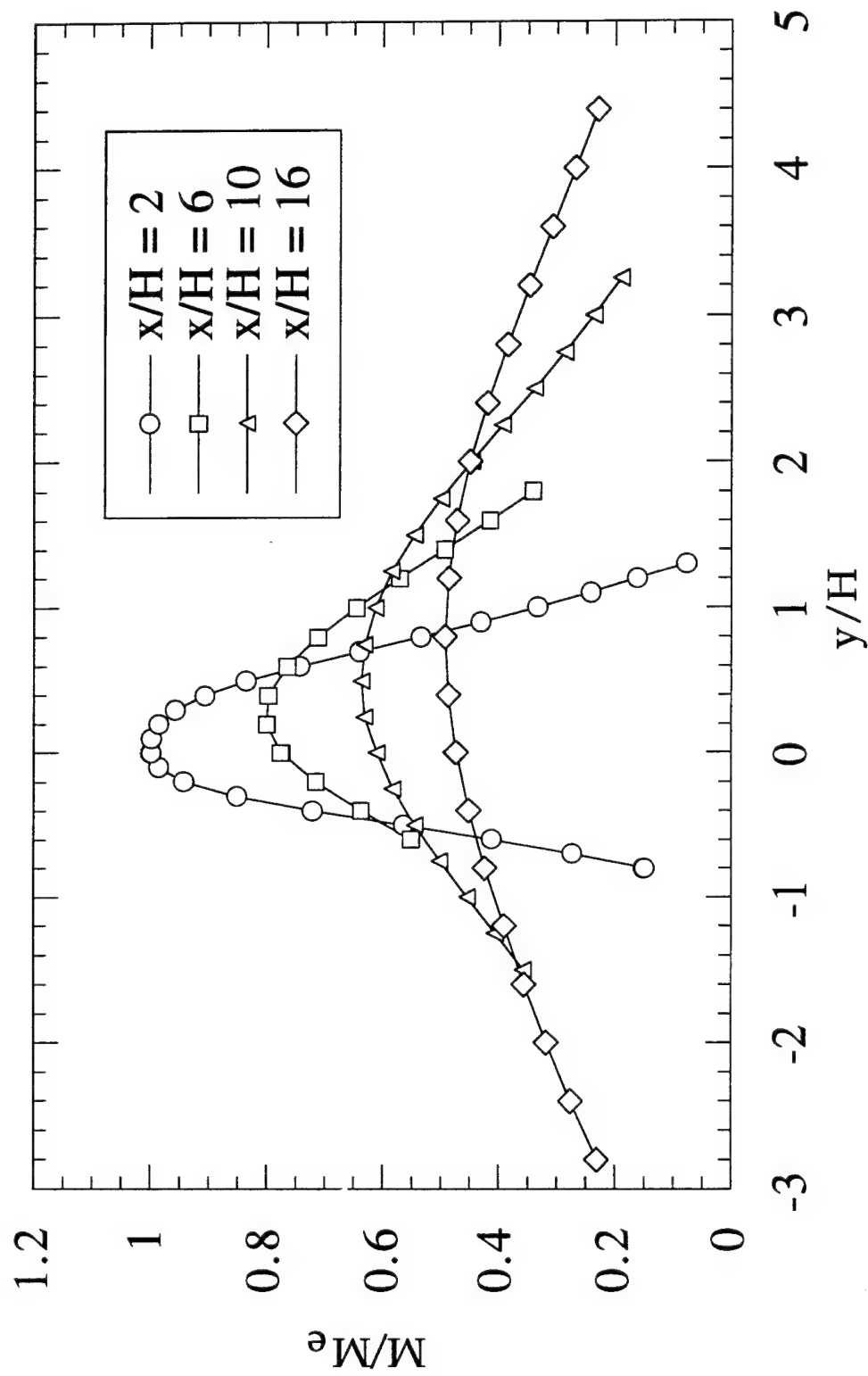


Figure 18. Downstream pitot surveys showing increasing offset in Mach profile as measurements are made at increasing  $x/H$  positions as measured from the collar exit. The amount of offset can be used to determine the thrust vector angle,  $\delta_v$ .  $M_e = 0.5$ .

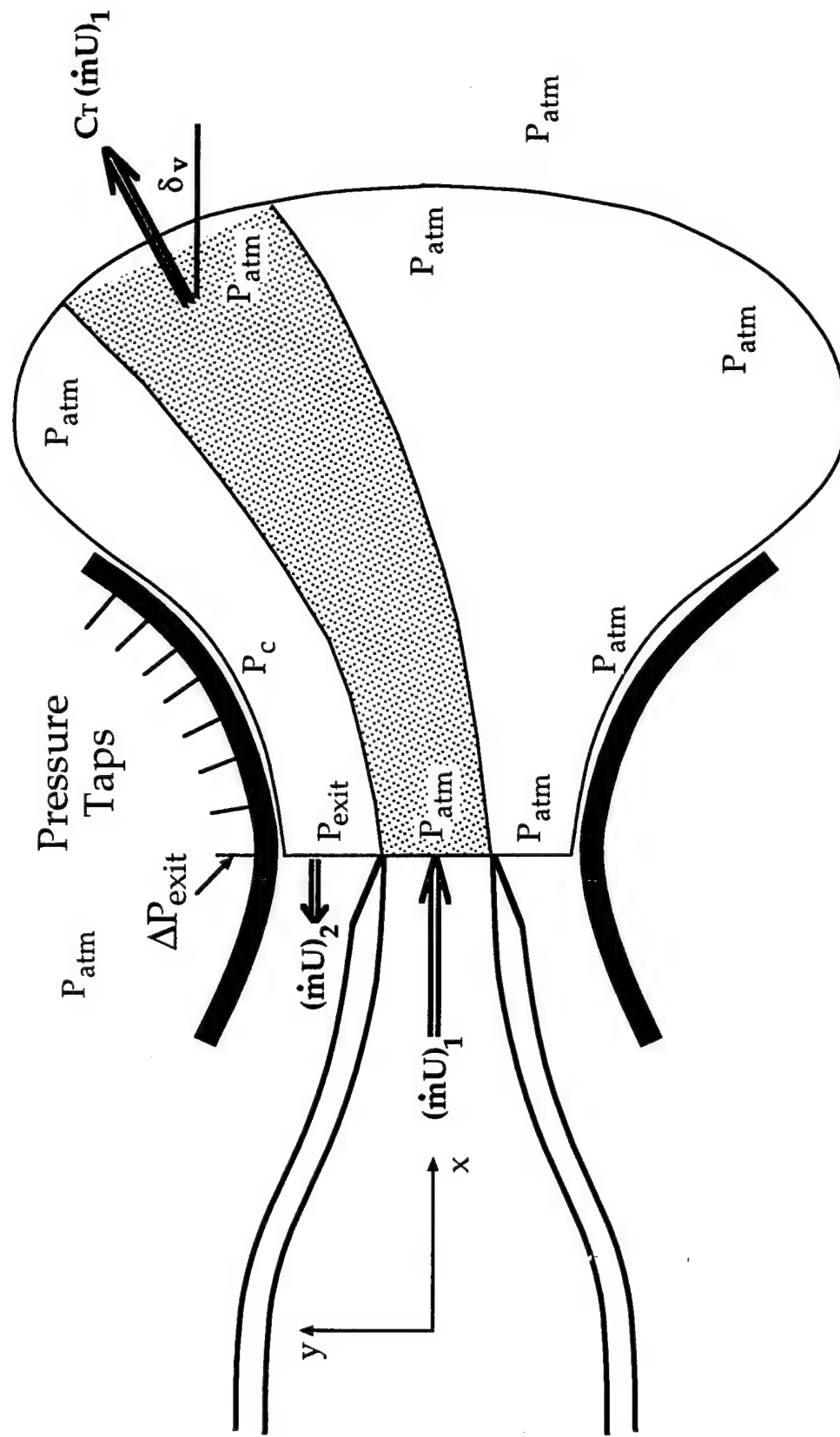


Figure 19. Schematic showing the boundaries of the control volume used to calculate vector angle. Forces are resolved from static pressure measurements along collar walls and estimated pressure profiles across exit plane. The outside boundary of the control volume is assumed to be at ambient pressure.

Figure 19.

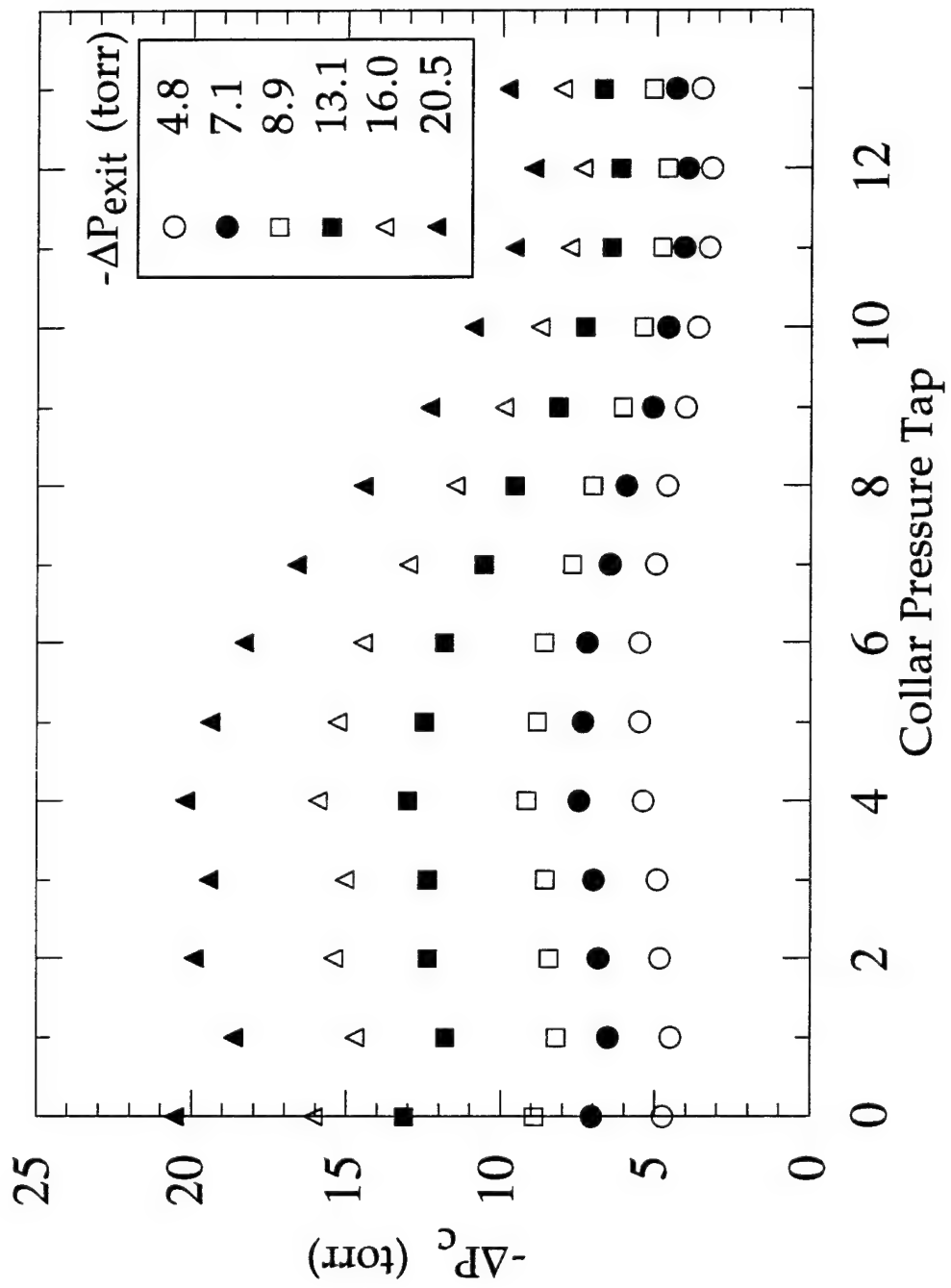


Figure 20. Collar static pressure profiles taken on the  $L/H = 2$ ,  $\alpha = 60^\circ$  collar for a gap height of  $G/H = 0.40$  at  $M_e = 0.5$ .

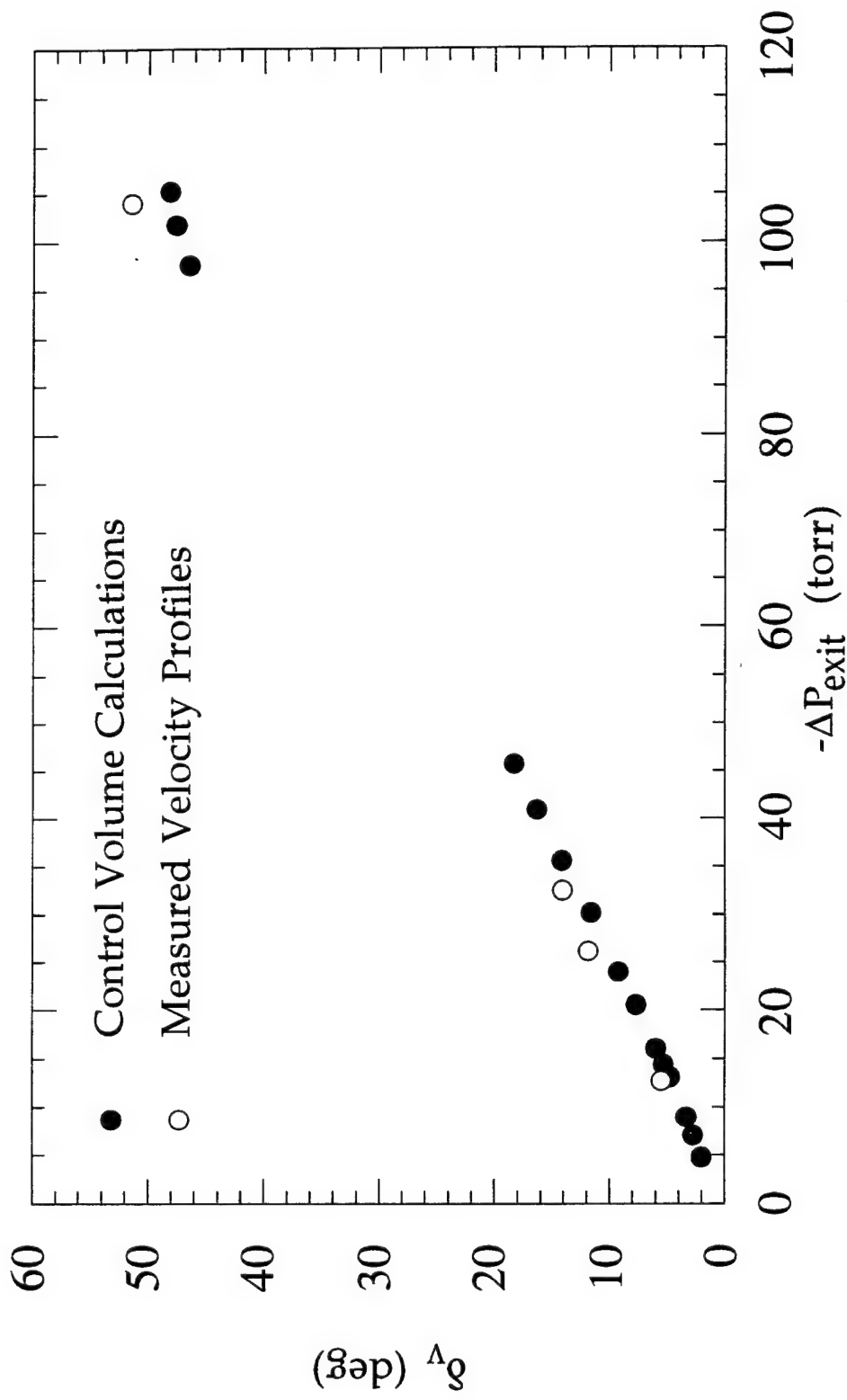


Figure 21. Thrust vector response curve as a function of gage exit pressure,  $-\Delta P_{\text{exit}}$ . Data are for the  $L/H = 2$ ,  $\alpha = 60^\circ$  collar at  $G/H = 0.4$  and  $M_e = 0.5$ . Open symbols compare vector angle determined by downstream Mach profiles to control volume calculations represented by the solid symbols.

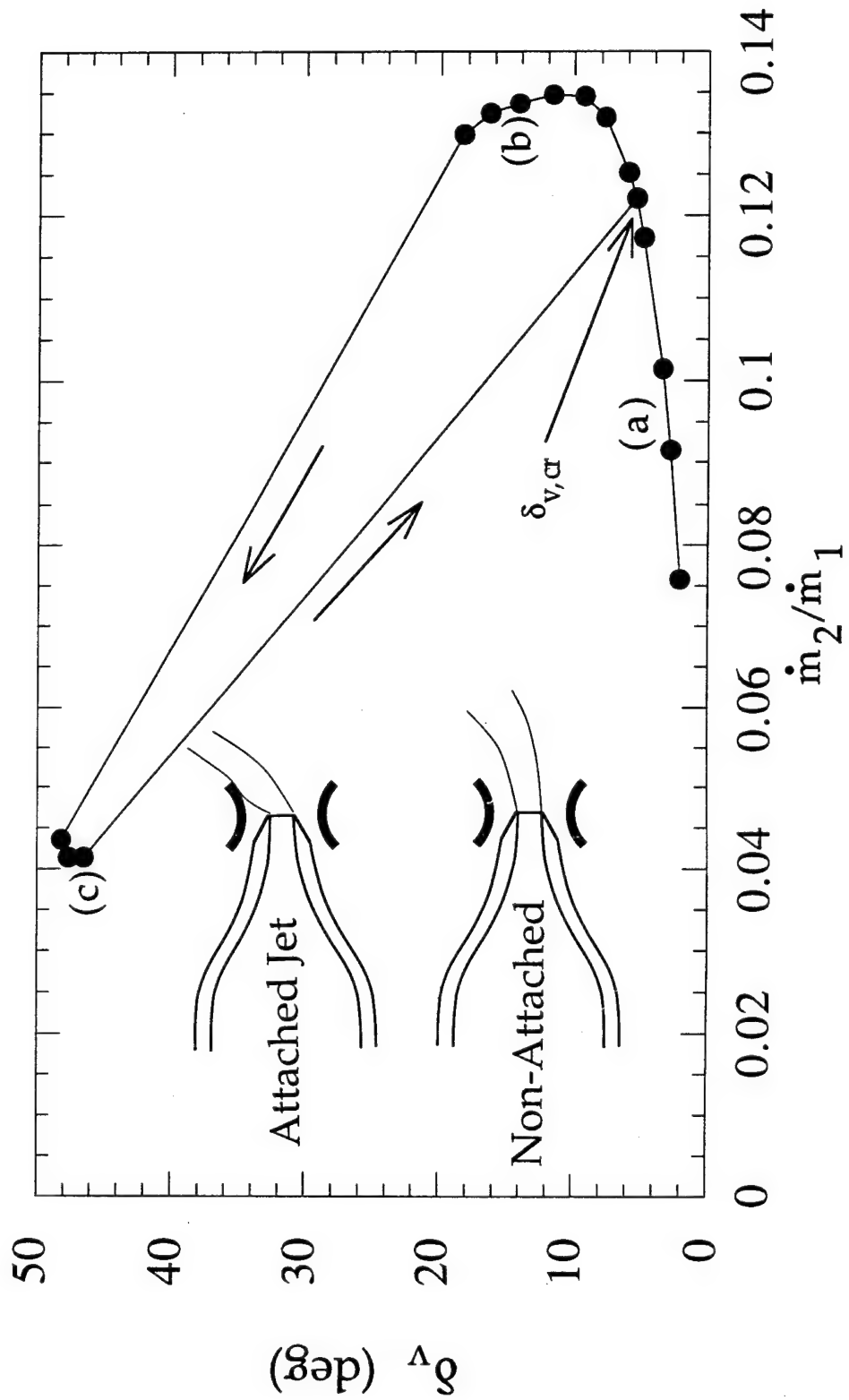
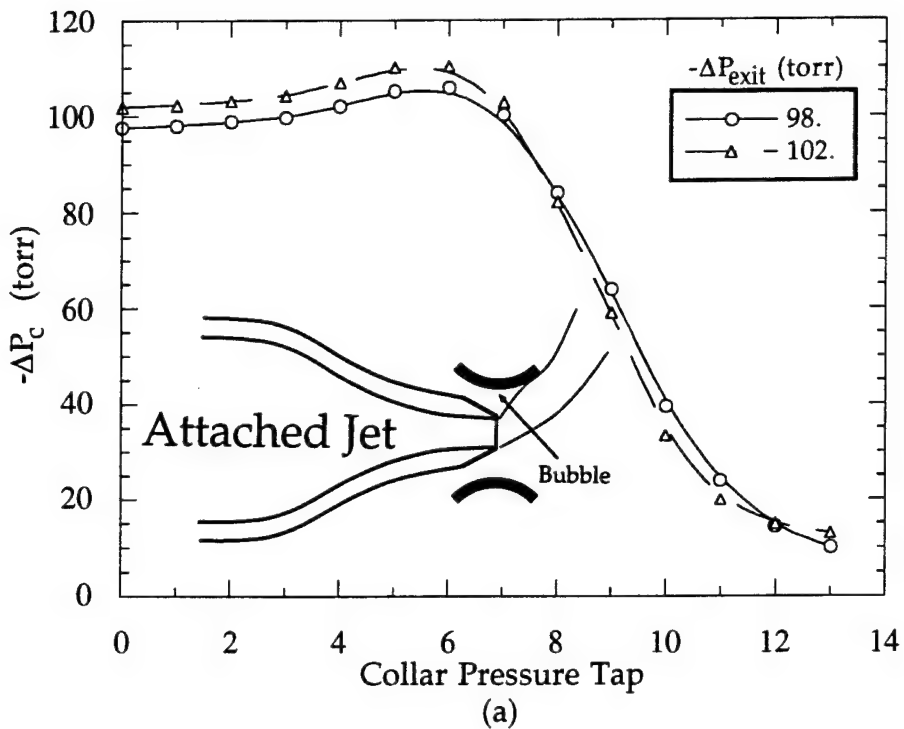
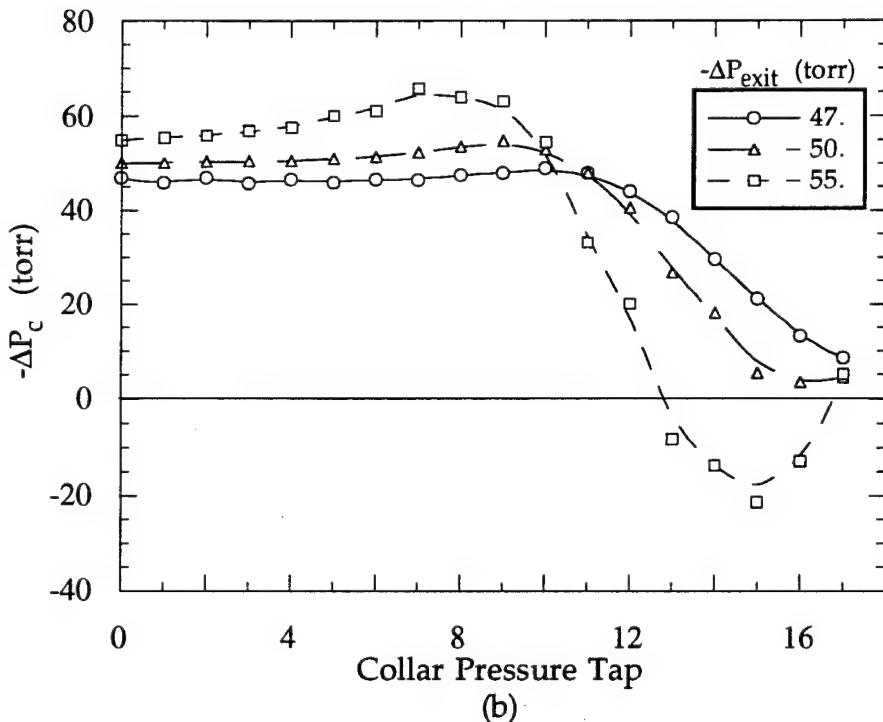


Figure 22. Thrust vector response curve as a function of reverse flow to primary mass flow ratio. Data are for the  $L/H = 2$ ,  $\alpha = 60^\circ$  collar at  $G/H = 0.4$  and  $M_e = 0.5$ . The hysteretic effect of collar attachment on vector angle is shown. The critical vector angle,  $\delta_{\text{v},\text{cr}}$ , marked by the arrow, is defined as the maximum angle achieved before the jet becomes bistable.



(a)



(b)

Figure 23. Collar static pressure distributions with attached jet for: (a) the  $L/H = 2, \alpha = 60^\circ$  collar at  $G/H = 0.4$ , and (b) the  $L/H = 3.5, \alpha = 30^\circ$  collar at  $G/H = 0.75$ .  $M_e = 0.5$  for both cases.

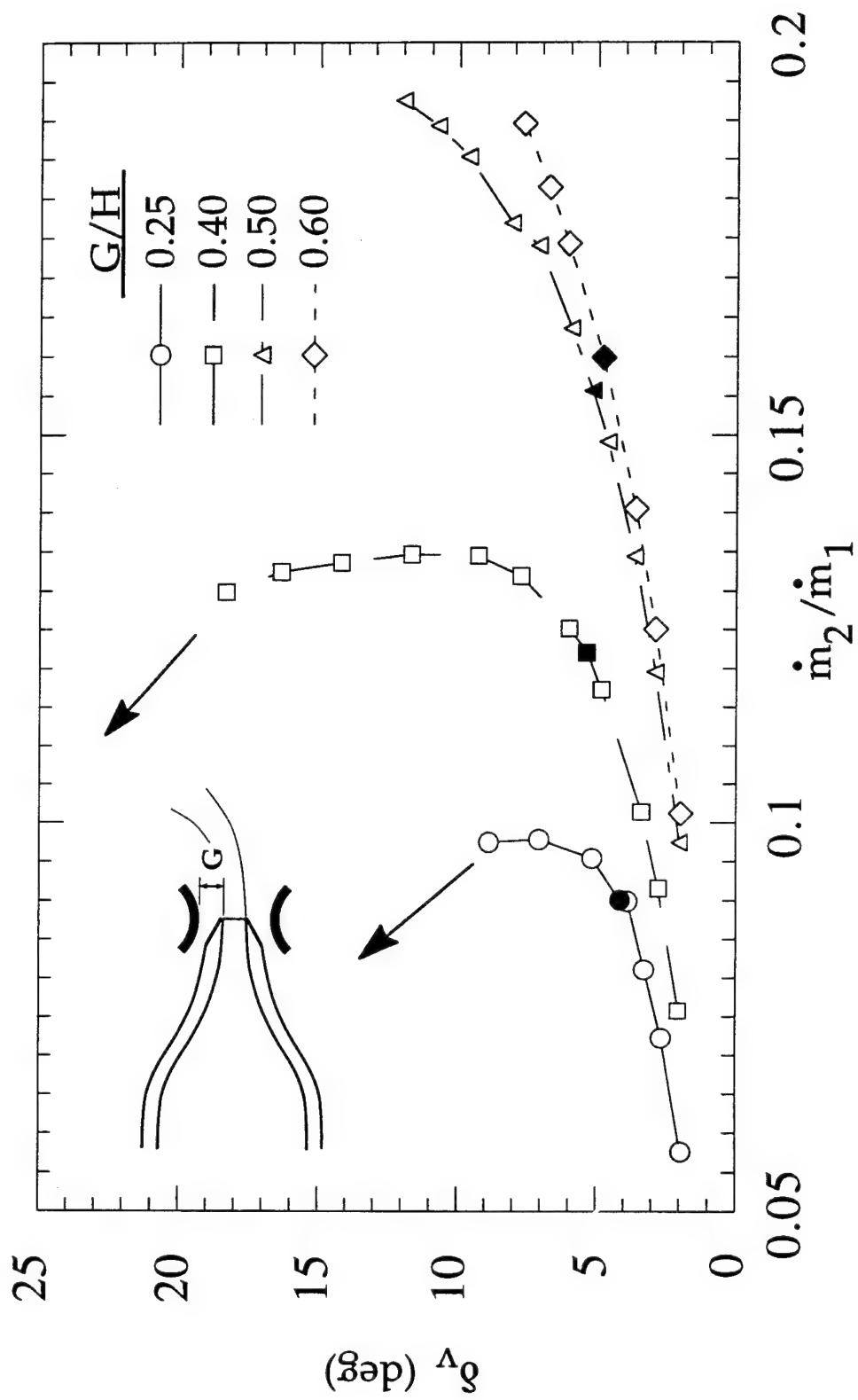


Figure 24. Thrust vector response curve as a function of mass flow ratio for the  $L/H = 2$ ,  $\alpha = 60^\circ$  collar at  $M_e = 0.5$ . Effect of varying gap height is illustrated. Continuous data shown. Solid symbols represent critical vector angle values where jet returns from attachment to collar.

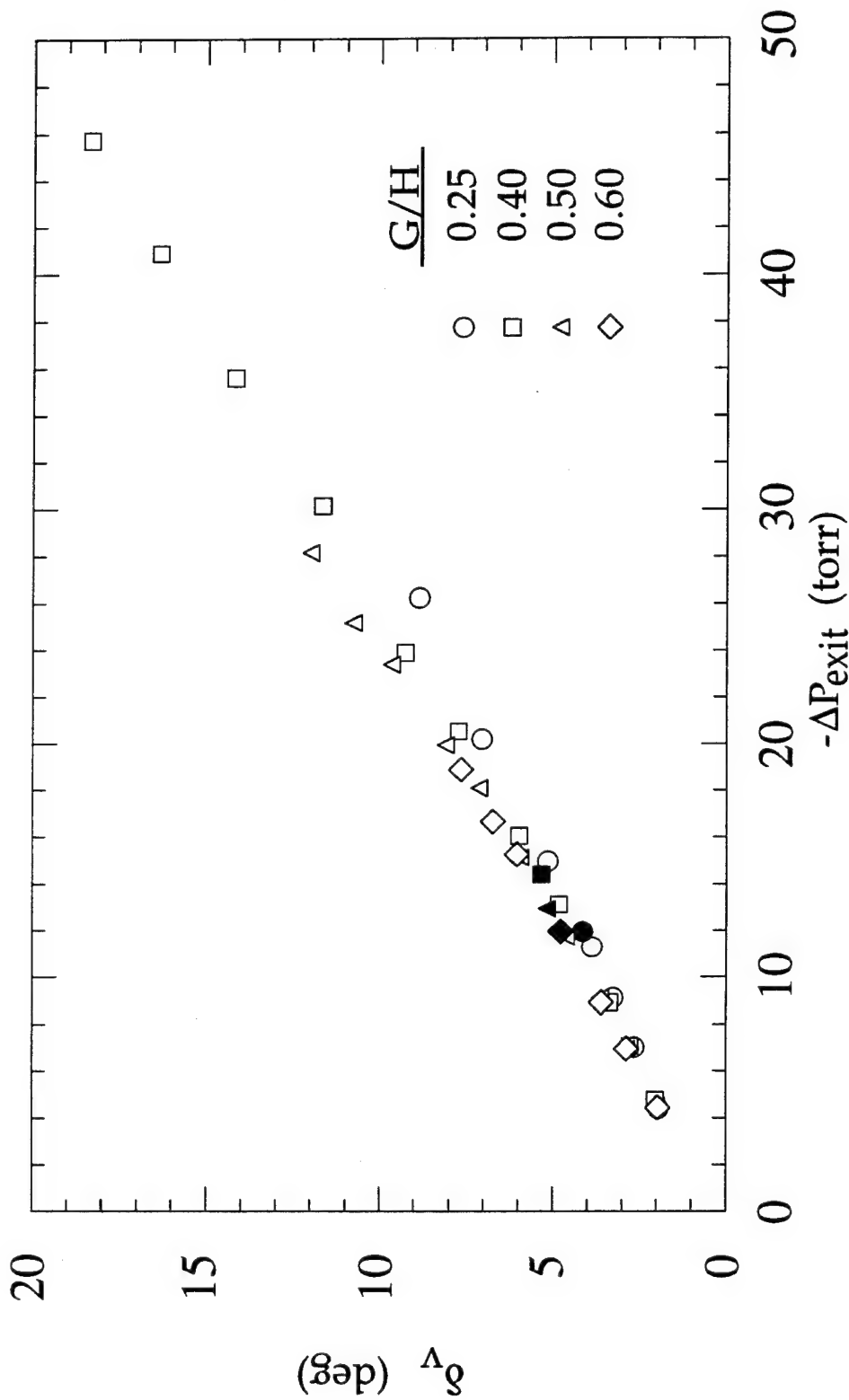


Figure 25.  $-\Delta P_{\text{exit}}$  thrust vector response curve for the  $L/H = 2$ ,  $\alpha = 60^\circ$  collar at  $M_e = 0.5$  comparing operation for variable gap heights. Continuous data shown. Solid symbols represent critical vector angle values.

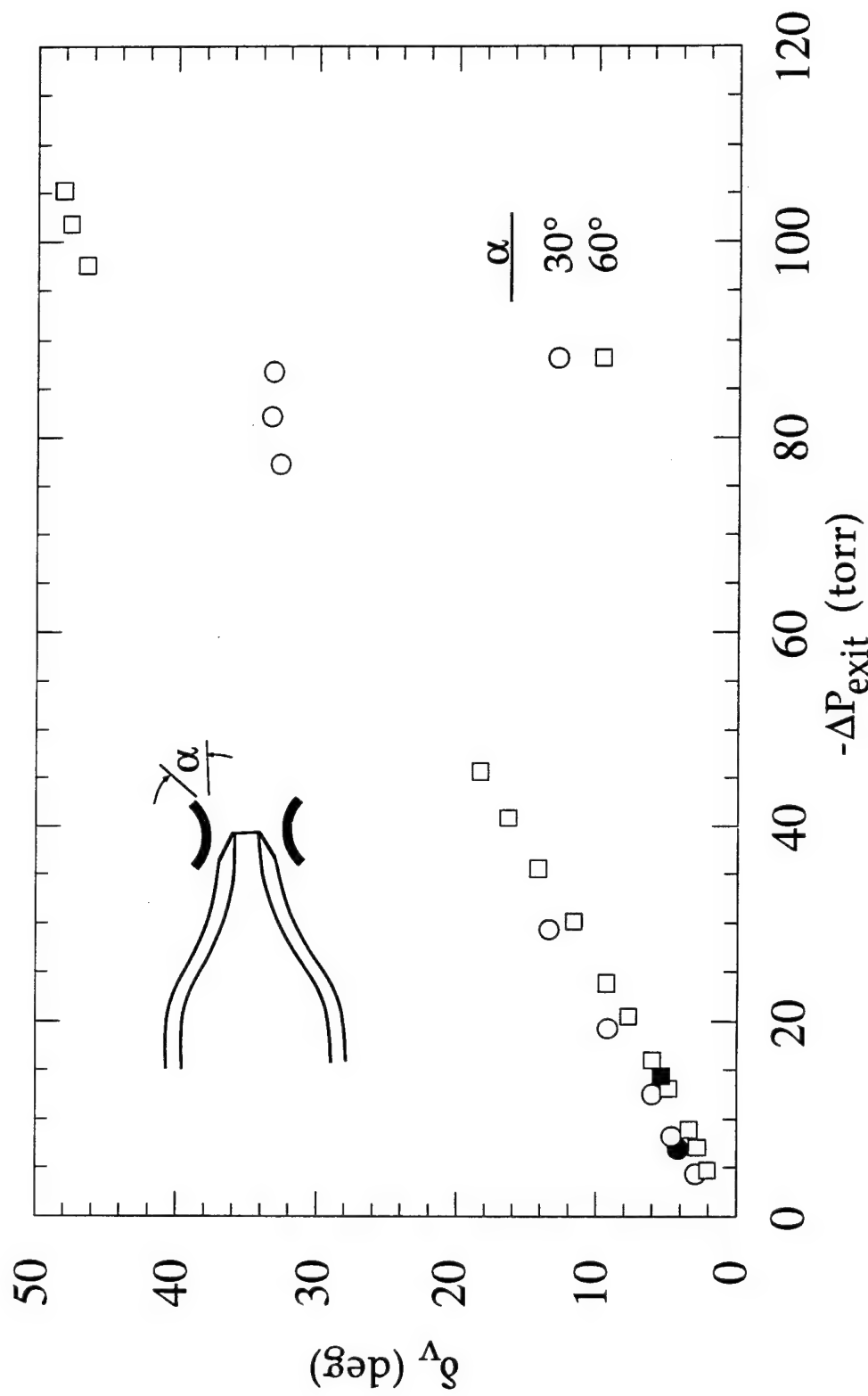


Figure 26.  $-\Delta P_{\text{exit}}$  thrust vector response curve for the  $\alpha = 30^\circ$  and  $60^\circ$  collars. Both collars are 2.0H in length and have gap heights of  $G/H = 0.4$ . Continuous and attached data shown. Solid symbols represent critical vector angle values.  $M_e = 0.5$ .

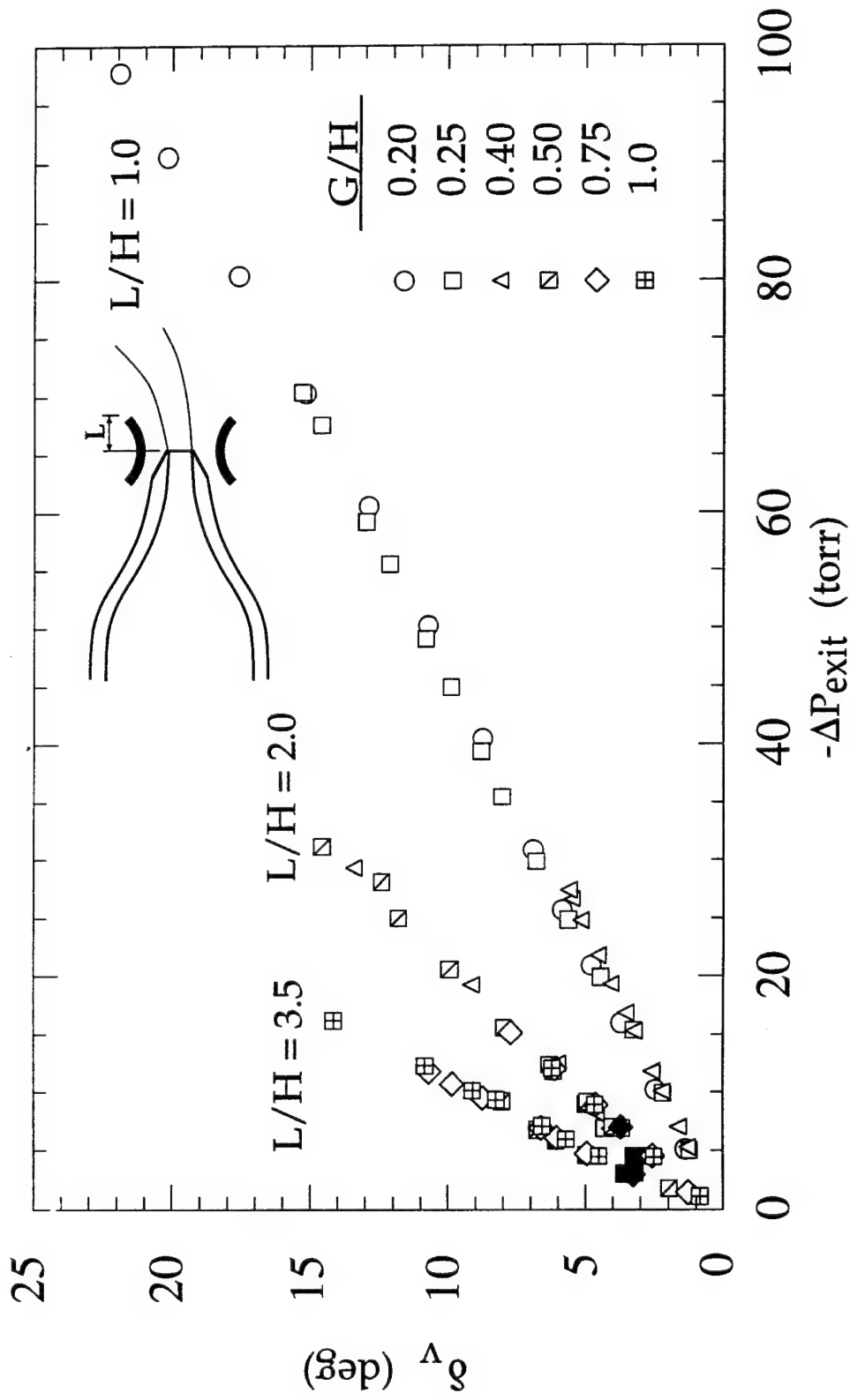


Figure 27.  $-\Delta P_{\text{exit}}$  thrust vector response curve for all  $\alpha = 30^\circ$  collars comparing operation for differing collar lengths. Each symbol represents a separate gap height. Solid symbols represent critical vector angle values for each length.  $M_e = 0.5$ .

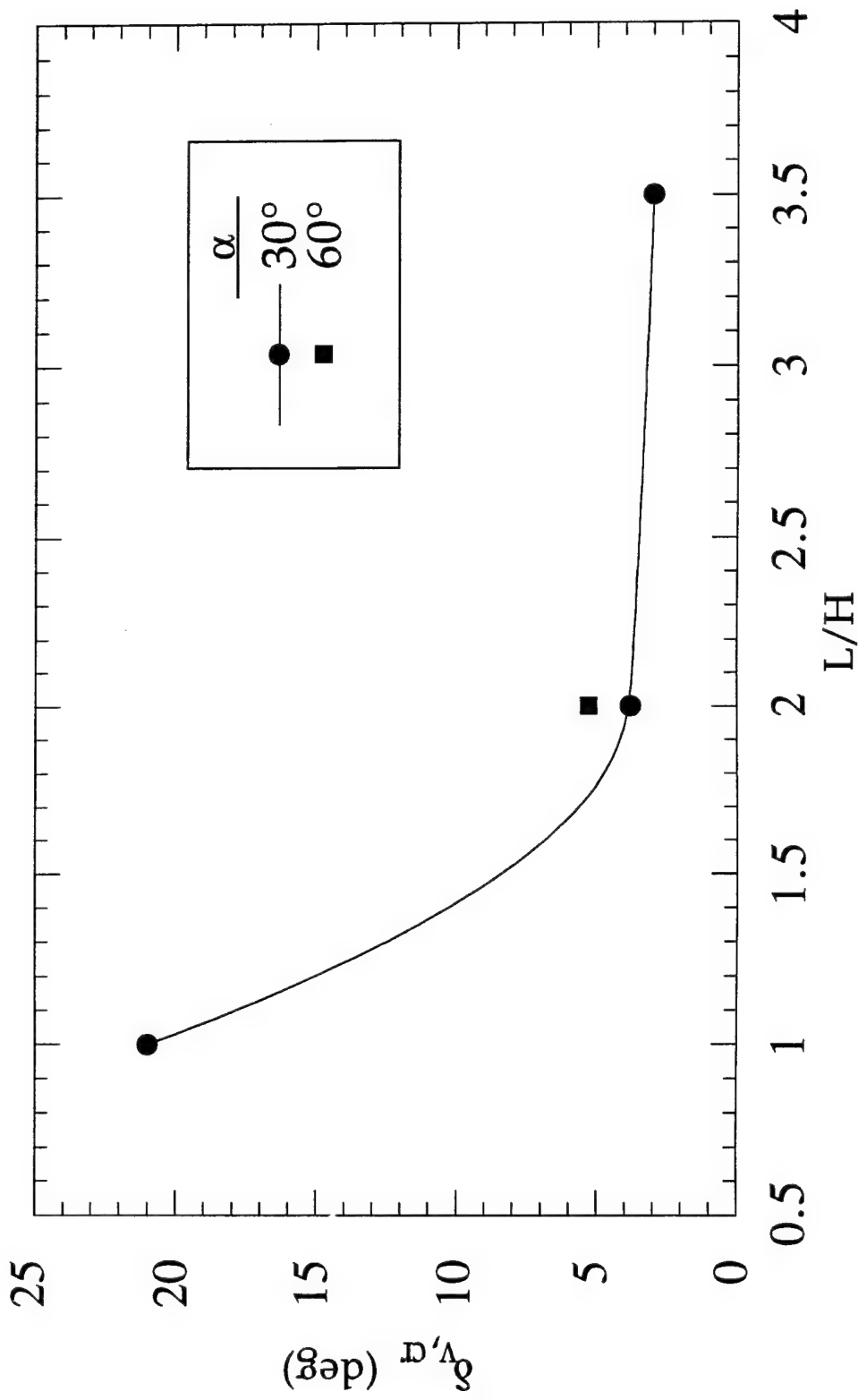


Figure 28. Maximum critical vector angle obtainable for each collar length as a function of collar length and divergence angle.  $G/H = 0.2, 0.4$ , and  $0.5$  for  $L/H = 1.0, 2.0$ , and  $3.5$  at  $\alpha = 30^\circ$ .  $G/H = 0.4$  for  $L/H = 2.0$  at  $\alpha = 60^\circ$ .  $M_e = 0.5$  for all cases.

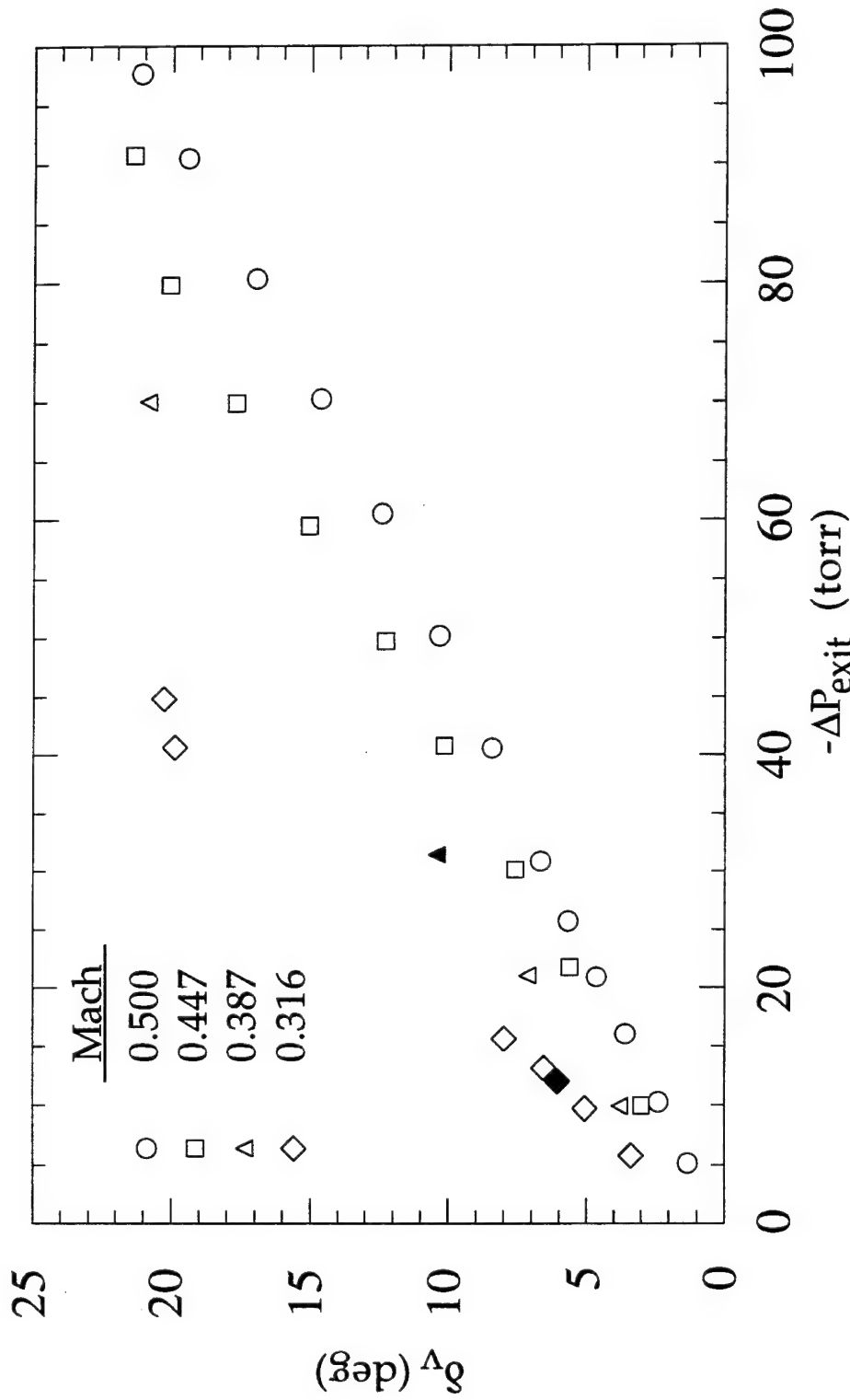


Figure 29.  $-\Delta P_{\text{exit}}$  vector response curve for  $L/H = 1$ ,  $\alpha = 30^\circ$  collar comparing operation for variable jet exit Mach numbers. Gap height was fixed at  $G/H = 0.2$ . Both continuous and attached data are included for the  $M_e = 0.387$  and  $0.316$  cases (the  $M_e = 0.5$  and  $0.447$  cases were non-hysteretic). Solid symbols represent critical vector angle.

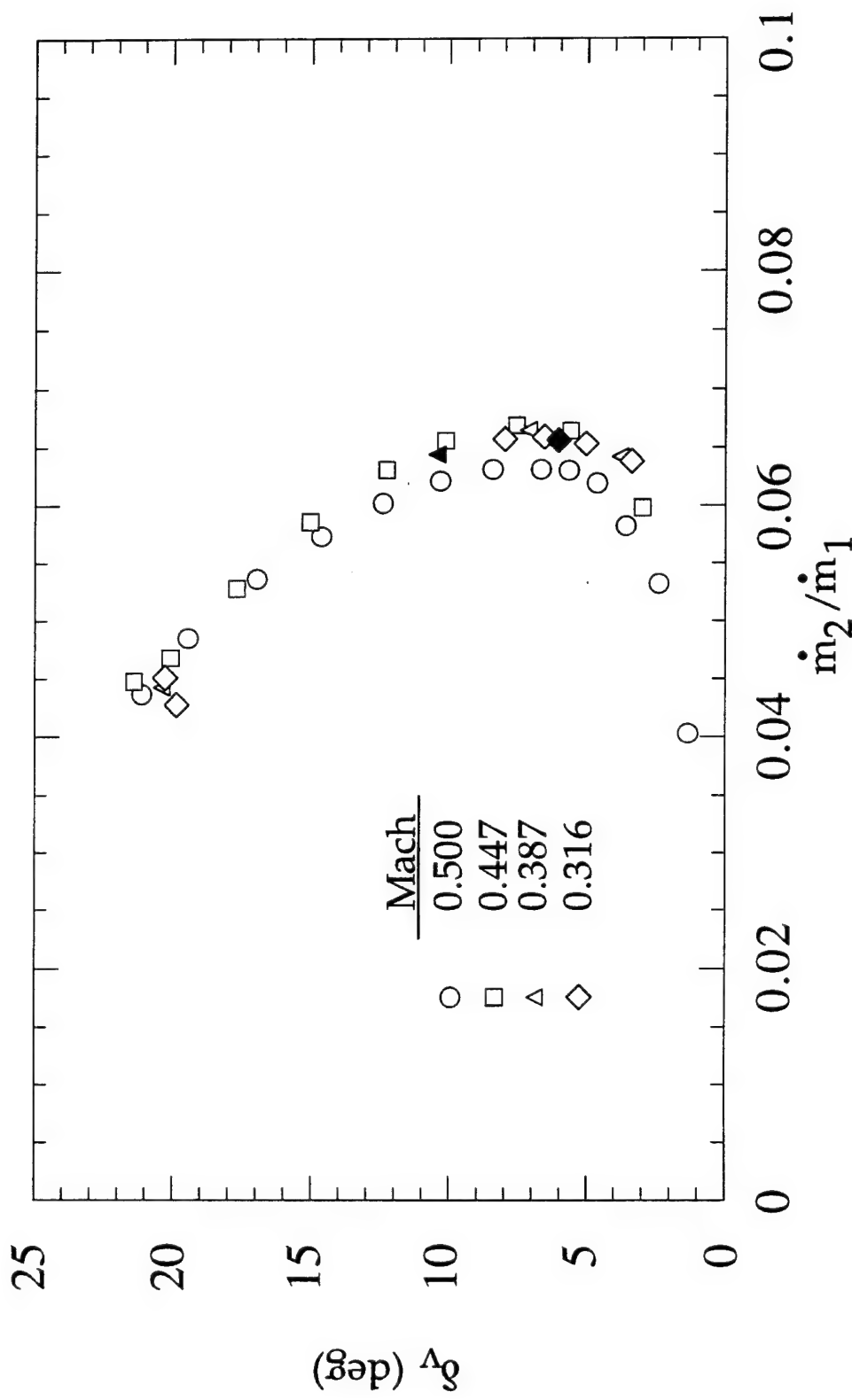


Figure 30. Mass flow ratio vector response curve for the same data plotted in the previous figure.  
 $L/H = 1.0, \alpha = 30^\circ$  collar at  $G/H = 0.2$ .

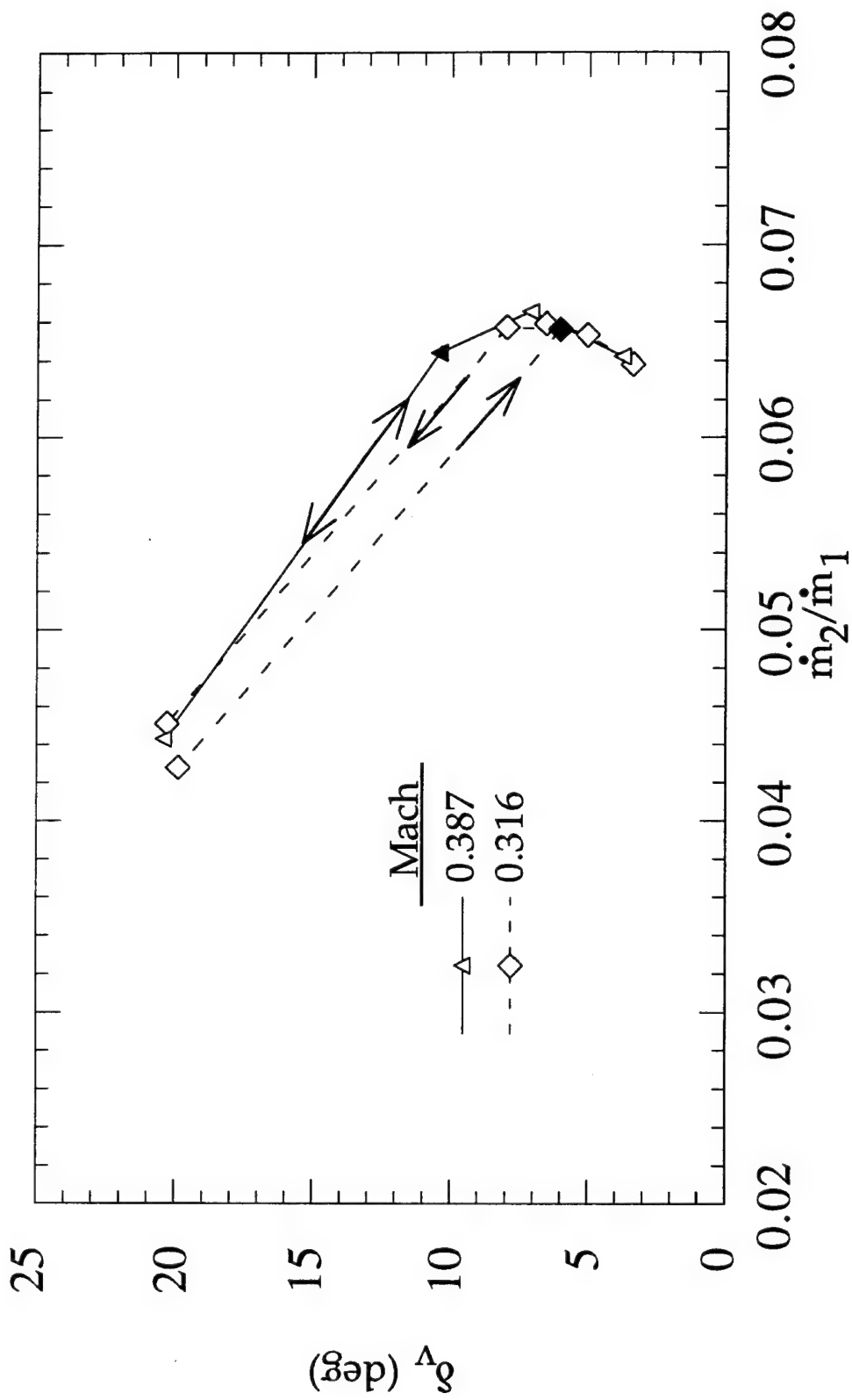


Figure 31. Detail showing the hysteresis curves in the mass flow ratio vector response curves for the  $M_e = 0.316$  and  $0.387$  cases.  $L/H = 1.0$ ,  $\alpha = 30^\circ$  collar at  $G/H = 0.2$ .

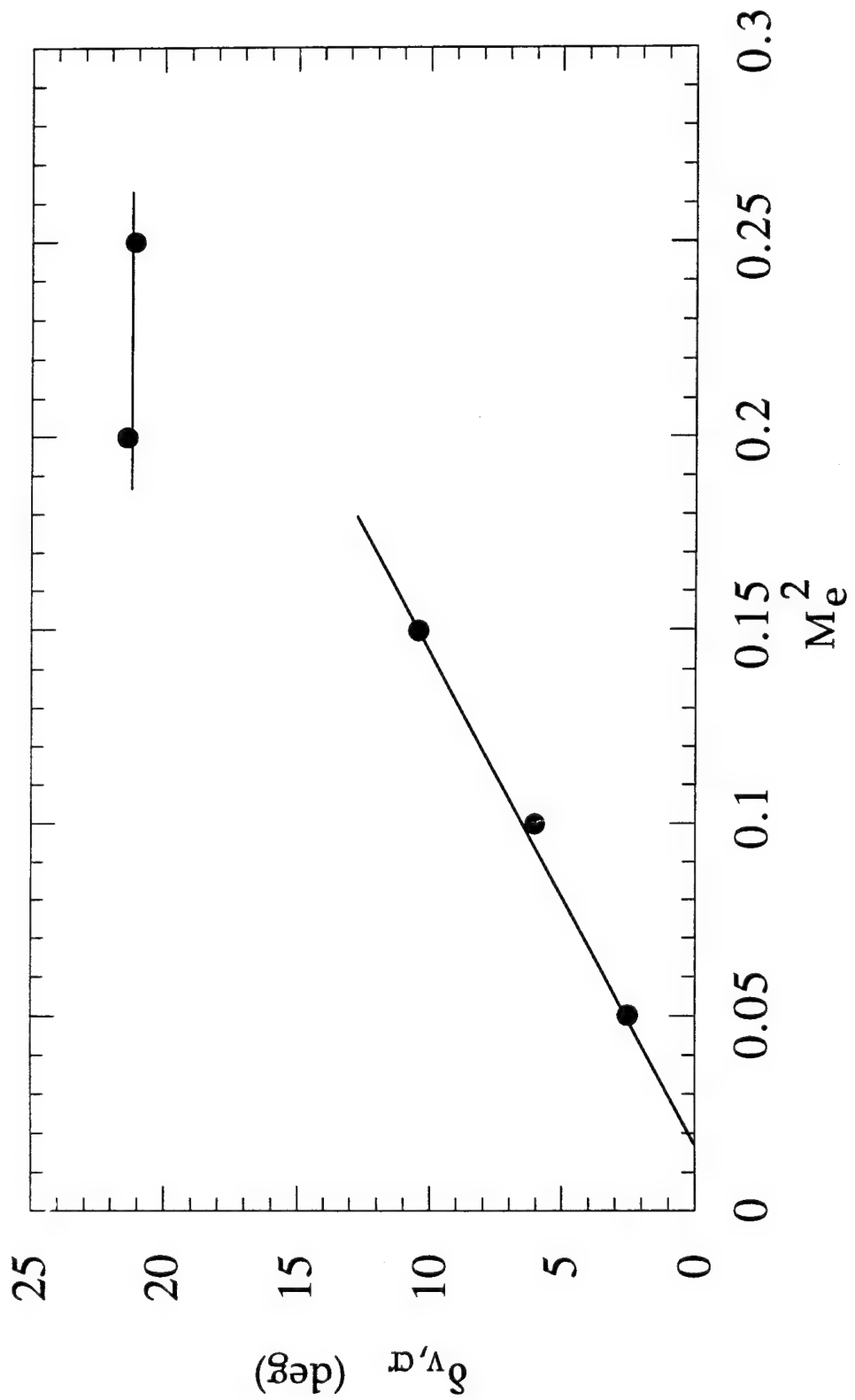


Figure 32. Critical vector angle as a function of  $M_e^2$  for the  $L/H = 1$ ,  $\alpha = 30^\circ$  collar at  $G/H = 0.2$ .

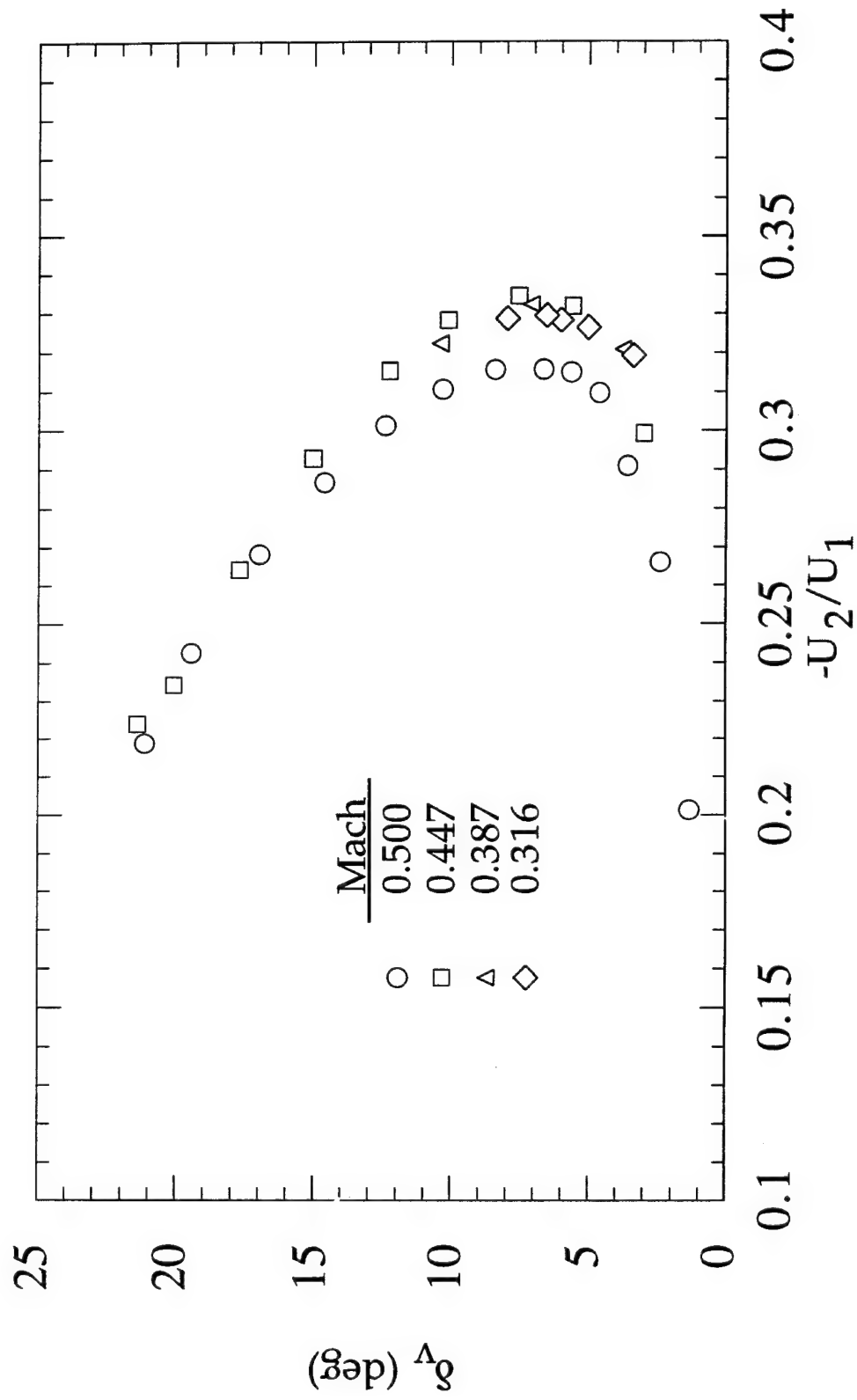


Figure 33. Velocity ratio thrust vector response curve for the  $L/H = 1$ ,  $\alpha = 30^\circ$  collar at  $G/H = 0.2$  for variable exit Mach numbers.

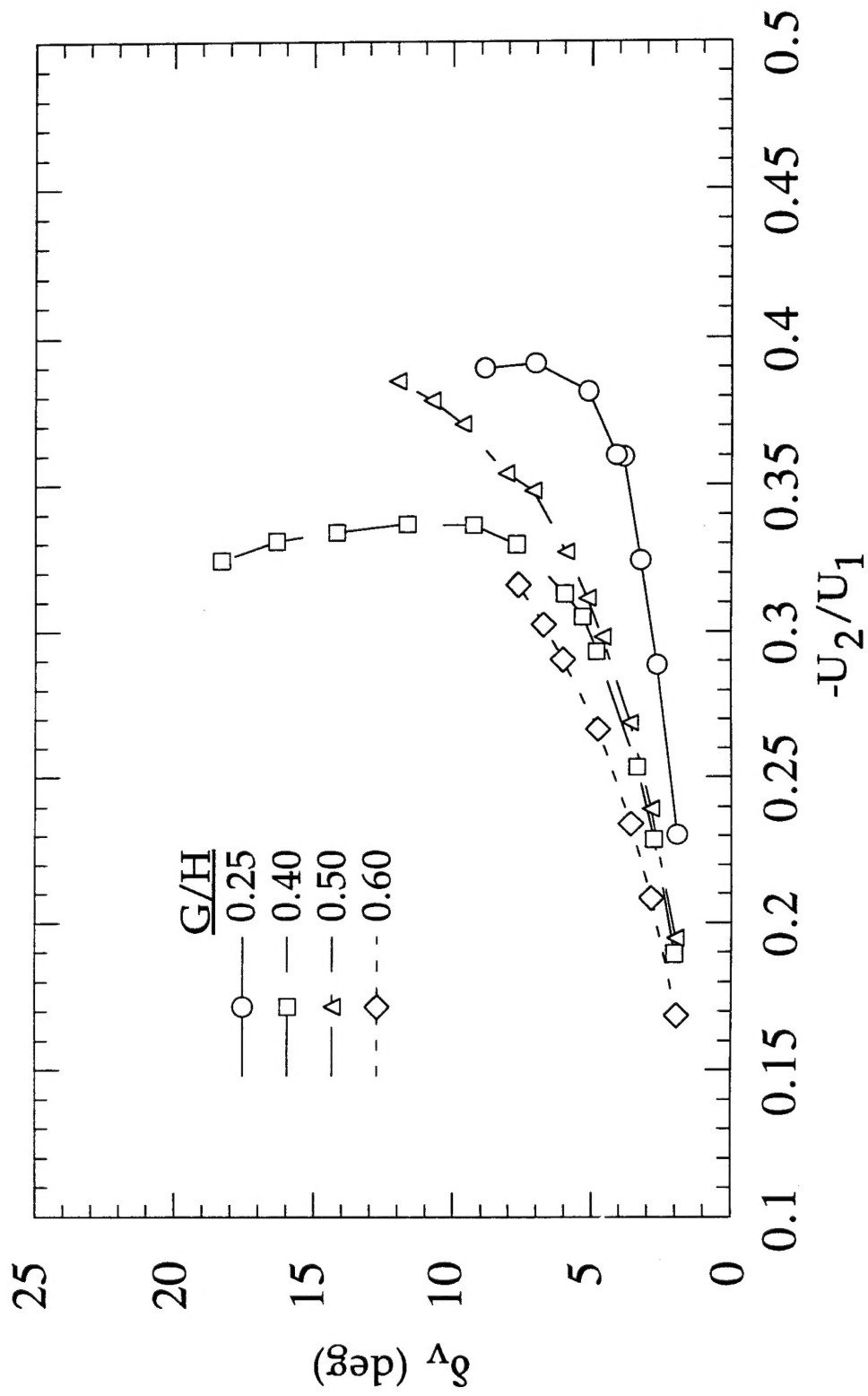


Figure 34. Thrust vector response curve as a function of reverse over primary velocity ratio for the  $L/H = 2$ ,  $\alpha = 60^\circ$  collar for variable gap heights.

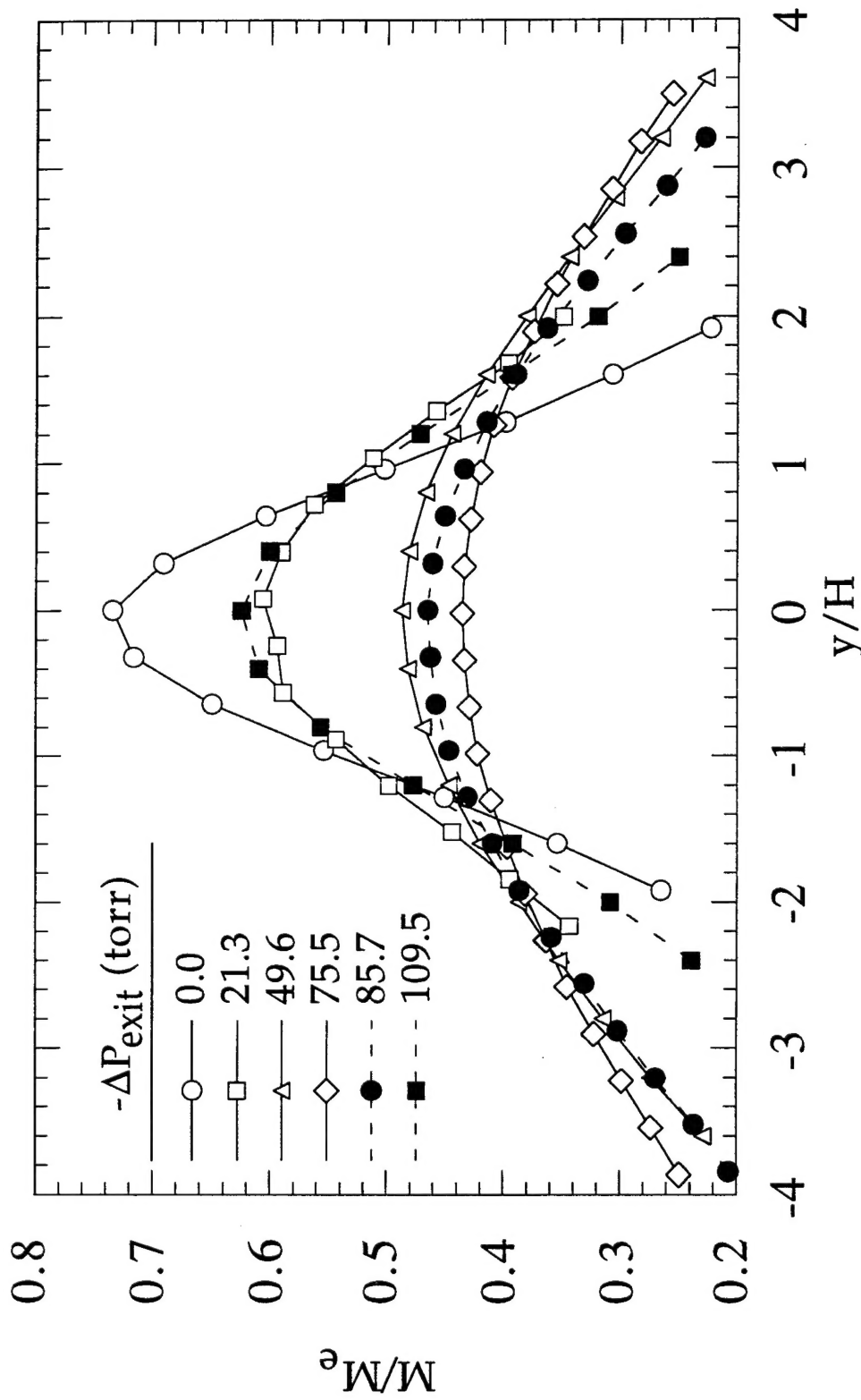
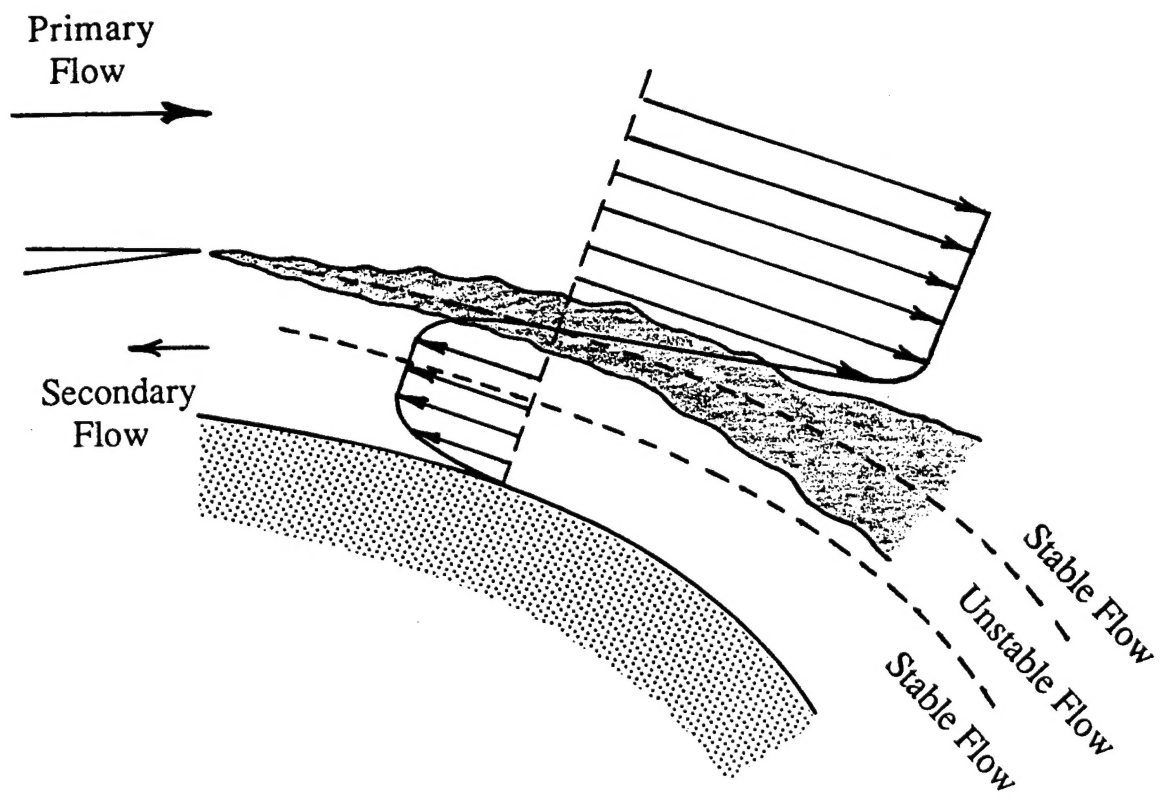


Figure 35. Mean Mach profiles showing the effect of suction on jet spreading for the  $L/H = 1$ ,  $\alpha = 30^\circ$  collar at  $G/H = 0.2$ . Data was taken at  $16H$  downstream of the collar exit with the  $y$ -axis aligned normal to the vector angle for each level of suction.  $M_e = 0.5$ .



$$\text{Stable: } \frac{\partial(rU)^2}{\partial r} > 0$$

$$\text{Unstable: } \frac{\partial(rU)^2}{\partial r} < 0$$

Figure 36. Diagram showing the centrifugal instability of the countercurrent mixing layer when the jet is vectored close to the collar surface.

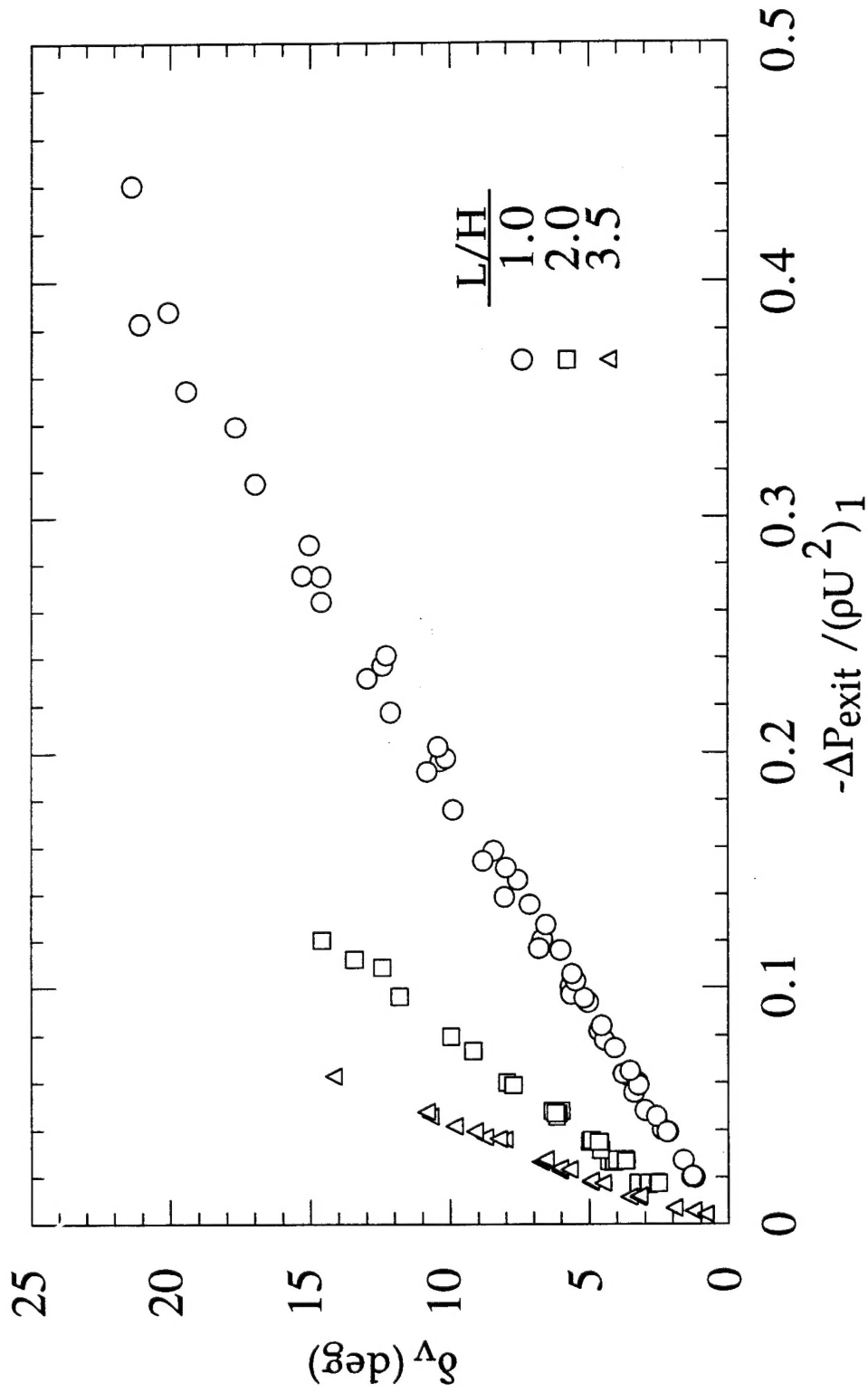


Figure 37. Thrust vector response curves as a function of gage exit pressure normalized by primary momentum flux. Data are shown for all gap heights,  $0.2 < G/H < 1.0$ , and exit Mach numbers,  $0.316 < M_e < 0.500$ , for the  $\alpha = 30^\circ$  collars. The effect of collar length is shown.